



Edwin Alexander Delgado Insuasty

**Sensitivity of next-generation neutrino
detectors to the observation of Earth matter
effects on supernova neutrinos in the
framework of invisible neutrino decay**

Tese de Doutorado

Thesis presented to the Programa de Pós-graduação em Física of PUC-Rio in partial fulfillment of the requirements for the degree of Doutor em Ciências – Física.

Advisor : Prof. Hiroshi Nunokawa
Co-advisor: Dr. Alexander Argüello Quiroga

Rio de Janeiro
December 2021



Edwin Alexander Delgado Insuasty

**Sensitivity of next-generation neutrino
detectors to the observation of Earth matter
effects on supernova neutrinos in the
framework of invisible neutrino decay**

Thesis presented to the Programa de Pós-graduação em Física of PUC-Rio in partial fulfillment of the requirements for the degree of Doutor em Ciências – Física. Approved by the Examination Committee:

Prof. Hiroshi Nunokawa

Advisor

Departamento de Física – PUC-Rio

Dr. Alexander Argüello Quiroga

Co-advisor

Departamento de Física – PUC-Rio

Prof. Arman Esmaili Taklimi

Departamento de Física – PUC-Rio

Prof. David Vanegas Forero

UDEM

Prof. Orlando Luis Goulart Peres

UNICAMP

Prof. Pietro Chimenti

UEL

Rio de Janeiro, December 1st, 2021

All rights reserved.

Edwin Alexander Delgado Insuasty

Graduated in Physics at the Nariño University (UDENAR) in 2008 and obtained his M.Sc. Degree in Physics from Pontifical Catholic University of Rio de Janeiro (PUC-RIO) in 2014.

Bibliographic data

Delgado Insuasty, Edwin Alexander

Sensitivity of next-generation neutrino detectors to the observation of Earth matter effects on supernova neutrinos in the framework of invisible neutrino decay / Edwin Alexander Delgado Insuasty; advisor: Hiroshi Nunokawa; co-advisor: Alexander Argüello Quiroga. – 2021.

126 f. : il. color. ; 30 cm

Tese (doutorado) - Pontifícia Universidade Católica do Rio de Janeiro, Departamento de Física, 2021.

Inclui bibliografia

1. Física – Teses. 2. Neutrinos de supernova. 3. Efeitos da matéria da Terra. 4. Decaimiento invisível de neutrinos. 5. Próxima geração de detectores de neutrino. 6. Ordenamento de massas de neutrinos. 7. Análise de Fourier. 8. Teoria de detecção de sinal. I. Nunokawa, Hiroshi. II. Argüello Quiroga, Alexander. III. Pontifícia Universidade Católica do Rio de Janeiro. Departamento de Física. IV. Título.

CDD: 530

To my mother, for her support
and encouragement.

Acknowledgments

I dedicate this space to those people who directly or indirectly contributed to the completion of this research and its conclusion in this text. I would like to first thank God for granting me the strength, perseverance and wisdom without which the accomplishment of this work would not have been possible. Then I wish to thank my mother, her advice made me an integral person, able to overcome all the obstacles that arose throughout these years of study. I would like to express my genuine appreciation to professor Hiroshi Nunokawa for his patience and willingness to assist me and guide me through all difficulties. I also want to thank Alexander Quiroga and Leydi Silva for your friendship and unconditional support during all these years, my deepest thanks.

This study was financed in part by the Coordenação de Aperfeiçoamento de Pessoal de Nível Superior - Brasil (CAPES) - Finance Code 001 and CNPq agency, thank you very much.

Abstract

Delgado Insuasty, Edwin Alexander; Nunokawa, Hiroshi (Advisor); Argüello Quiroga, Alexander (Co-Advisor). **Sensitivity of next-generation neutrino detectors to the observation of Earth matter effects on supernova neutrinos in the framework of invisible neutrino decay.** Rio de Janeiro, 2021. 126p. Ph.D. Thesis – Departamento de Física, Pontifícia Universidade Católica do Rio de Janeiro.

In this thesis we studied the potential that the next-generation neutrino detectors (JUNO, Hyper-Kamiokande and DUNE) will have to the detection of the Earth matter effects through the identification of the modulations in the energy spectrum of neutrinos from core-collapse supernovae in our galaxy, assuming the possibility of the invisible decay of ν_2 after the neutrinos have left the star, on their way to Earth. Recent simulations of gravitational collapse (and subsequent explosion) of stars more massive than $\sim 8M_\odot$ show that during the cooling phase the average energies $\langle E_{\bar{\nu}_e} \rangle$ and $\langle E_{\nu_x} \rangle$ become very similar and the fluxes tend to equalize, making it difficult to observe the Earth matter effects using a single detector. In this work we show that the inclusion of neutrino decay creates also the possibility of observing the effects under consideration in the neutrino detection channel if the mass ordering is normal and in the anti-neutrino channel if the ordering is inverted, which is not expected in the absence of neutrino decay. In particular, if the decay rate is more than $\sim 70\%$, we find that the invisible neutrino decay of ν_2 can enhance the observation possibilities of Earth matter effects even for supernovae at a distance of 10 kpc from us.

Keywords

Supernova neutrinos; Earth matter effects; Invisible neutrino decay; Next-generation neutrino detectors; Neutrino mass ordering; Fourier analysis; Signal detection theory.

Resumo

Delgado Insuasty, Edwin Alexander; Nunokawa, Hiroshi (Orientador); Argüello Quiroga, Alexander (Coorientador). **Sensibilidade da próxima geração de detectores de neutrino à observação dos efeitos da matéria da Terra em neutrinos que vem de supernovas no contexto do decaimento invisível de neutrinos.** Rio de Janeiro, 2021. 126p. Tese de Doutorado – Departamento de Física, Pontifícia Universidade Católica do Rio de Janeiro.

Nesta tese estudamos o potencial que terão a próxima geração de detectores de neutrinos (JUNO, Hyper-Kamiokande e DUNE) para a detecção dos efeitos da matéria da Terra através da identificação das modulações no espectro de energia dos neutrinos de supernovas de colapso de núcleo em nossa galáxia, assumindo a possibilidade do decaimento invisível de ν_2 após os neutrinos terem deixado a estrela, caminho da Terra. Simulações recentes do colapso gravitacional (e subsequente explosão) de estrelas com massa maior do que $\sim 8M_\odot$ mostram que durante a fase de esfriamento as energias médias $\langle E_{\bar{\nu}_e} \rangle$ e $\langle E_{\nu_x} \rangle$ tornam-se muito semelhantes e os fluxos tendem a se igualar, tornando difícil observar os efeitos da matéria da Terra usando um único detector. Neste trabalho mostramos que a inclusão do decaimento dos neutrinos também cria a possibilidade de observar os efeitos em consideração no canal de detecção de neutrinos se o ordenamento de massa for normal e no canal anti-neutrino se o ordenamento for invertido, o que não é esperado na ausência de decaimento. Em particular, se a taxa de decaimento for maior do que $\sim 70\%$, descobrimos que o decaimento invisível de ν_2 pode aumentar as possibilidades de observação dos efeitos da matéria da Terra, mesmo para supernovas a uma distância de 10 kpc de nós.

Palavras-chave

Neutrinos de supernova; Efeitos da matéria da Terra; Decaimento invisível de neutrinos; Próxima geração de detectores de neutrino; Ordenamento de massas de neutrinos; Análise de Fourier; Teoria de detecção de sinal.

Table of contents

1	Introduction	15
2	Supernova Neutrinos and Elements of Neutrino Physics	17
2.1	Neutrinos	17
2.1.1	Neutrinos in the standard model	19
2.1.2	Neutrinos beyond standard model	21
2.1.3	Neutrino sources	24
2.2	Supernovae	28
2.2.1	Core collapse mechanism	31
2.2.2	CCSN neutrino spectra	34
3	Neutrino Oscillations	39
3.1	Solar and atmospheric neutrino problem	39
3.2	Neutrino oscillations in vacuum	40
3.3	Neutrino oscillations in matter	44
3.3.1	MSW effect in the star	46
3.3.2	MSW effect in the Earth	55
4	Neutrino Decay	61
4.1	Neutrino lifetime	62
4.2	Nambu-Goldstone neutrino decay model	63
4.3	Neutrino decay scenarios adopted in this work	68
4.4	Earth matter effects in the presence of neutrino decay	70
5	Earth Matter Effect Detection by a Single Detector	76
5.1	The Jiangmen Underground Neutrino Observatory (JUNO)	77
5.1.1	CCSN neutrino detection in a liquid scintillator detector	78
5.1.2	Earth matter effects at JUNO	80
5.2	Hyper-Kamiokande	85
5.2.1	CCSN neutrino detection in a water Cherenkov detector	86
5.2.2	Earth matter effects at Hyper-K	87
5.3	The Deep Underground Neutrino Experiment (DUNE)	90
5.3.1	CCSN neutrino detection in a liquid argon detector	91
5.3.2	Earth matter effects at DUNE	92
6	Sensitivity of the next-generation of neutrino detectors to Earth Matter Effects	95
6.1	Sensitivity parameter d'	96
6.2	Detection probability of Earth matter effects	100
7	Conclusions	104
	Bibliography	107
A	CCSN neutrino spectra in presence of neutrino decay	125

List of figures

- Figure 2.1 Supernovae classification [156]. 29
- Figure 2.2 Expected CCSN neutrino energy spectra associated with the scenarios listed in Table 2.3. Here, the dark (ν_e), red ($\bar{\nu}_e$) and green (ν_x) curves show the un-oscillated neutrino fluences from a CCSN located at 10 kpc from us. 38
- Figure 3.1 Energy dependence of P_ξ for a density profile $\rho = A/r^3$. The dashed lines divide the whole range of E/E^* in three parts: non adiabatic region (I), intermediate region (II) and adiabatic region (III) . 49
- Figure 3.2 Level crossing diagrams. Solid lines correspond to eigenvalues of the effective Hamiltonian and the dashed lines to energies of flavor states. Here, we present the anti-neutrinos as neutrinos traveling through the star matter with an effective negative potential, i.e. $N_e < 0$. 52
- Figure 3.3 Density profile for the Earth according to the PREM model [177]. 56
- Figure 3.4 Regeneration factors as a function of neutrino energy are shown for $L = 4000$ km (left panels), $L = 8000$ km (middle panels) and $L = 12000$ km (right panels) for neutrino (upper panels) and anti-neutrinos (lower panels). 60
- Figure 4.1 ΔF defined in Eqs. (4-32) and (4-33) are shown as a function of neutrino energy computed for $L = 4000$ km . 72
- Figure 4.2 ΔF defined in Eqs. (4-32) and (4-33) are shown as a function of neutrino energy computed for $L = 8000$ km. 73
- Figure 4.3 ΔF defined in Eqs. (4-32) and (4-33) are shown as a function of neutrino energy computed for $L = 12000$ km. 73
- Figure 4.4 ΔF plotted as a function of both the neutrino energy and the distance between the CCSN and the Earth, for each supernova model listed in table 2.3. 74
- Figure 5.1 Inverse energy distribution of IBD events expected at JUNO for $L = 4000$ km and Model D in table 2.3. The red and black histograms refer specifically to S3 (100% decay of $\bar{\nu}_2$) scenario computed for NMO and IMO, respectively. 81
- Figure 5.2 (JUNO) Fourier transform of the inverse energy spectrum for two different distances traveled by neutrinos, $L = 8000$ km (upper and lower-left panels) and $L = 12000$ km (middle and lower-right panels) for NMO (upper and middle panels) and IMO (lower panels). 83

- Figure 5.3 (JUNO) Averaged power spectrum over 1000 Monte Carlo run samples for $L = 4000$ km, model D in table 2.3 and NMO. We present these results for the typical CCSN distance of 10 kpc (upper panels) and for a distance of 5 kpc (lower panels), for the three scenarios, S1, S2 and S3 described in the subsection 4.3. We considered the standard deviation given in each fit (vertical error bars) as error in the measurement. 84
- Figure 5.4 Same as in Fig. 5.3 but for IMO. 84
- Figure 5.5 (Hyper-K) Fourier transform of the inverse energy spectrum for two different distances traveled by neutrinos, $L = 8000$ km (upper and lower-left panels) and $L = 12000$ km (middle and lower-right panels) for NMO (upper and middle panels) and IMO (lower panels). 88
- Figure 5.6 (Hyper-K) Averaged power spectrum over 1000 Monte Carlo run samples for $L = 4000$ km, model D in table 2.3 and NMO. We present these results for the typical CCSN distance of 10 kpc (upper panels) and for a distance of 5 kpc (lower panels), for the three scenarios, S1, S2 and S3 described in the subsection 4.3. We considered the standard deviation given in each fit (vertical error bars) as error in the measurement. 89
- Figure 5.7 Same as in Fig. 5.6 but for IMO. 89
- Figure 5.8 (DUNE) Fourier transform of the inverse energy spectrum for two different distances traveled by neutrinos, $L = 8000$ km (upper panels) and $L = 12000$ km (lower panels) for NMO (left panels) and IMO (right panels). 92
- Figure 5.9 (DUNE) Averaged power spectrum over 1000 Monte Carlo run samples for $L = 4000$ km, model D in table 2.3 and NMO. We present these results for the typical CCSN distance of 10 kpc (upper panels) and for a distance of 5 kpc (lower panels), for the three scenarios, S1, S2 and S3 described in the subsection 4.3. We considered the standard deviation given in each fit (vertical error bars) as error in the measurement. 93
- Figure 5.10 Same as in Fig. 5.9 but for IMO. 93
- Figure 6.1 Background fluctuations (black) and signal (red) area distributions. The background distribution was calculated in the absence of the Earth matter effects whereas the signal distribution was calculated in the presence of the Earth matter effects. We show these distributions for JUNO for the both mass orderings: NMO (upper panels) and IMO (lower panels). The hatched region correspond to a confidence level of 2σ (95.45%). 96
- Figure 6.2 Sensitivity to Earth matter effects detection in presence of invisible neutrino decay for JUNO (upper panel), Hyper-K (middle panel) and DUNE (lower panel) as a function of the ν_2 decay rate r_2 . 98

Figure 6.3 Detection probability of the Earth matter effects at 2σ (95.45% C.L.) by JUNO (upper panel), Hyper-K (middle panel) and DUNE (lower panel), for NMO (upper panel of each subfigure) and IMO (lower panel of each subfigure) for different CCSN emission models B, C2 and D as a function of the distance to CCSN.

101

Figure 6.4 Detection probability of the Earth matter effects at 2σ (95.45% C.L.) by JUNO (upper panel), Hyper-K (middle panel) and DUNE (lower panel), for NMO (upper panel of each subfigure) and IMO (lower panel of each subfigure) for different CCSN emission models B, C3 and D as a function of the distance to CCSN.

102

List of tables

Table 2.1	Neutrino oscillation parameters summary. Adapted from de Salas <i>et al.</i> [14].	22
Table 2.2	Half-life and Majorana mass limits from recent experiments. From Formaggio <i>et al.</i> [81].	24
Table 2.3	CCSN neutrino emission model parameters used in this work. Values with an asterisk as superscript denote that $\widehat{\alpha}_{\nu_e} = \widehat{\alpha}_{\bar{\nu}_e}$ was assumed.	37
Table 5.1	Charged and neutral current detection interactions in JUNO for CCSN neutrinos: (1) IBD, (2) elastic neutrino-proton scattering, (3) elastic neutrino-electron scattering, (4) NC interaction on ^{12}C , (5) and (6) CC interactions on ^{12}C .	78
Table 5.2	Charged and neutral current detection interactions in Hyper-K for CCSN neutrinos: (1) IBD, (2) elastic neutrino-electron scattering, (3) $\bar{\nu}_e$ ^{16}O CC interaction, and (4) ν_e ^{16}O CC interaction.	86
Table 5.3	Charged and neutral current detection interactions in DUNE for CCSN neutrinos: (1) ν_e ^{40}Ar CC interaction, (2) elastic neutrino-electron scattering, (3) ν ^{40}Ar NC interaction, and (4) $\bar{\nu}_e$ ^{40}Ar CC interaction.	91

List of Abbreviations

CC – Charged current.

CCSN – Core-Collapse Supernova.

C.L. – Confidence level.

CP – Charge-Parity.

DUNE – Deep Underground Neutrino Experiment.

Hyper-K – Hyper-Kamiokande.

IBD – Inverse beta decay.

IMO – Inverse mass ordering.

JUNO – Jiangmen Underground Neutrino Observatory.

LMA – Large mixing angle.

LSc – Liquid scintillator.

MSW – Mikheyev - Smirnov - Wolfenstein effect.

NC – Neutral current.

NMO – Normal mass ordering.

$\mathcal{O}(n)$ – Of order n .

PMNS – Pontecorvo - Maki -Nakagawa - Sakata matrix.

PNS – Proto-neutron star.

PREM – Preliminary reference Earth model.

SM – Standard model of fundamental particles and interactions.

*He escrito un viento, un soplo vivo del viento
entre fragancias, entre hierbas mágicas; he
narrado el viento; sólo un poco de viento.*

Aurelio Arturo, *Morada al sur.*

1

Introduction

Neutrino oscillations have been definitively observed and its evidence comes from many experiments that detect solar [1, 2], atmospheric [3, 4], reactor [5, 6, 7, 8, 9], and accelerator neutrinos [10, 11, 12]; thus becoming a major evidence of the massive nature of this particle. In over the last years, the mixing angles and mass-squared differences that describe these oscillations have been measured with excellent precision [13, 14]: $\sin^2 \theta_{12} = 0.318$, $\sin^2 \theta_{13} = 0.0220$, $\sin^2 \theta_{23} = 0.574$, $\Delta m_{21}^2 = 7.50 \times 10^{-5} \text{ eV}^2$, $\Delta m_{31}^2 = 2.55 \times 10^{-3} \text{ eV}^2$. The observation of matter effects in the Sun shows us that the product $\Delta m_{21}^2 \sin 2\theta_{12}$ is positive and, therefore set $\Delta m_{21}^2 > 0$ by definition [15, 16]. However, currently there are still some open questions in neutrino physics, such as the neutrino mass ordering which can be normal or inverted, with normal ordering favored over inverted ordering at 2.5σ level [14]. Also, according to Ref. [14] the value for the Dirac CP phase is still undetermined, being 1.08π (1.58π) for normal (inverted) mass ordering the preferred value for this phase. The best fit value for the mixing angle θ_{23} lies in the second octant, with the first octant solution still allowed at $\sim 2.4\sigma$ [14]. These and other open questions such as the Dirac or Majorana nature [17, 18, 19, 20, 21, 22, 23], the absolute neutrino mass scale [24], the neutrino lifetime [25, 26, 27, 28, 29, 30, 31] are the primary goal of the current and future neutrino experiments.

Almost all the existing neutrino data can be explained consistently in terms of the three-neutrino mass-mixing parameters. However, there are some anomalies that do not fit this model well [32, 33, 34]. These anomalies are often relaxed with the existence of extra neutrino states that does not participate in the weak interactions and, so called sterile neutrinos [35, 36, 37, 38, 39, 40]. The mixing parameters of these neutrinos preferred by the MiniBooNE and LNSD experiments are in strong tension with the exclusion limit from the IceCube experiment, see for example Ref. [41]. This tension has led to propose new physical models in order to explain the IceCube(MiniBooNE) spectrum, among them we cite neutrino decay [42, 43] and neutrino splitting [44].

Supernova neutrinos have only been observed once in history coming from supernova SN 1987A, located at the Large Magallanic Cloud, a dwarf

satellite galaxy of the Milky Way, with a very small number of data collected. Future neutrino detections from these astrophysical sources are not free from anomalies that prevent their data to fit the 3ν mixing model well. Therefore, it is worth taking a closer look at these scenarios allowed by the theory and not yet ruled out by the experiments. In this work we consider the possibility of neutrino decay, much faster than the rate expected for massive neutrinos possessing only standard interactions (but slow enough not to be inconsistent with the SN 1987A events detected by Kamiokande [45], IMB [46] and BAKSAN [47] detectors) and its impact for the observation of Core-Collapse Supernova (CCSN) neutrinos [48, 49, 50, 51, 52, 53, 54] paying particular attention to the Earth matter effect. We note that effect of neutrino decay, if exist, must be subdominant in the currently available neutrino data.

At the Earth, CCSN neutrinos can interact with electrons from the medium through forward coherent elastic scattering which lead to flavor resonant transitions. As a consequence, their energy spectra exhibit small modulations which depend on both the average neutrino energies and the effective ratio between electron and non-electron neutrino fluxes [55, 56, 57, 58, 59]. The observation of such effects in the energy spectrum, using a single detector such as done in Ref. [57], might have little chance even with the next-generation of detectors because of the similarity of average energies, and the tendency of neutrino fluxes to equalize in the cooling phase [60, 61]. Faced with this situation, we contemplate for the first time the possibility that invisible neutrino decay alters the effective ratio between the neutrino fluxes in such a way that the decay effect enhances the observation of Earth matter effects.

This thesis is organized as follows. In chapter 2, we address the most relevant aspects of neutrino physics as well as describe briefly CCSN neutrino emission mechanism. In chapter 3, we give a brief introduction to the physics of neutrino oscillations for both scenarios: in vacuum and matter. These concepts are the vital importance in the study of the Earth matter effects. In chapter 4, we establish the neutrino decay scenarios that are considered throughout the work and we comment a little on the effect that the decay has on the Earth matter effects observation. In chapter 5, we discuss the basic aspects of our experiments in consideration: JUNO [62], Hyper-Kamiokande [63] and DUNE [64]. In Chapter 6 we present our results and finally we summarize our results in chapter 7.

We stress that in order to ensure better readability, throughout this work we made use of natural units, that is $c = \hbar = 1$.

Supernova Neutrinos and Elements of Neutrino Physics

This chapter is divided as follows: in section 2.1 we cover a bit of the neutrino history, their properties within the framework of the standard model of elementary particle physics (SM), the two major problems that SM presents when describing neutrinos and finally we give a brief summary about neutrino sources. Next, in section 2.2, we talk about supernova classification, the explosion mechanisms of a massive star, the model independent characteristics of the core-collapse neutrino spectrum which will be observed with our current and future detectors. And finally, we establish some supernova models that we will use in this work.

2.1

Neutrinos

The existence of neutrinos was postulated by Wolfgang Pauli in 1930 in order to give a satisfactory explanation to different inconsistencies reported in 1914 by James Chadwick in the β radioactive decay, process by which an atomic nucleus is transformed into another and emits an electron¹ [65]. The energy spectrum of the particle β (electrons or positrons) found by Chadwick was continuous, contrary to that found in the α disintegration or in the γ emission; indicating an apparent non-conservation of energy. Furthermore, the kinematic studies of the decay showed that the emitted proton and electron were not moving in the same direction, which seemed to violate momentum conservation. In the same way, the spin was not conserved in that process; the total spin of its products was half-integer, in contradiction to the integer value of the atom prior to the decay. Pauli unveiled its proposal on a letter addressed to the participants at a physics conference in Tübingen (Germany) where the problem of beta decay would be discussed [66], in this letter he called new particle as neutron and outlined some of its properties; among them the new

¹Back then, the β decay was thought to be a two-body decay. Since the mass of the parent nucleus is very close to that of the child one and the latter is in turn several orders greater than that of the electron, it would be expected that the emitted electron takes most of the energy of the process as kinetic energy, thus presenting a mono-energetic spectrum.

particle should:

1. take away the missing energy in order to guarantee the energy conservation,
2. be emitted with a certain speed and direction such that its momentum added vectorially to the momentum of the electron gives the momentum of the proton associated to the process,
3. have zero electrical charge,
4. have spin 1/2 in order to conserve the total angular momentum of the system,
5. interact weakly with matter, since no experiment up to that time had observed its presence.

The discovery of the neutron as we know it today: a particle with the mass comparable to the proton but without an electric charge, made by Chadwick in 1932, led Enrico Fermi to rename the Pauli's neutron as neutrino, which in Italian means small neutron. Two years later, in 1934, Fermi published a three-body β -decay theory known as Fermi theory [67], in which, a neutron that is part of a nucleus is transformed into a proton, producing a nucleus with an atomic number increased by one unit, and a pair of particles (electron and electron anti-neutrino) whose sum of energies must be equal to a constant. In the same 1934, Hans Bethe and Rudolf Peierls noticed the existence of the inverse beta decay (IBD), that is a quasielastic scattering between an electron anti-neutrino ($\bar{\nu}_e$) and a proton (p)

$$\bar{\nu}_e + p \rightarrow n + e^+, \quad (2-1)$$

where e^+ and n indicate, respectively, the positron and the neutron. Using Fermi's theory, they found for this interaction that for every cubic centimeter of water that contains $\sim 7 \times 10^{22}$ protons, there is a probability of 10^{-21} that a neutrino, with a cross section of $\sim 10^{-44} \text{ cm}^2$, will be detected; therefore a volume of 10^{21} cm^3 would be necessary to make a successful observation. Evidently, they concluded that it would be impossible to detect neutrinos through this decay.

However, in 1956, Clyde Cowan and Frederick Reines [68] demonstrated the existence of this elusive particle by observing electron anti-neutrinos from an intense flux $\sim \mathcal{O}(10^{12}) \bar{\nu}_e/\text{cm}^2/\text{s}$, emitted by one nuclear reactor at the Savannah River Plant, using a detector consisting of a multiple-layer

arrangement of scintillation counters (triethylbenzene solution) and target tanks (a water solution of cadmium chloride). When a neutron and a positron are produced according to Eq. (2-1), a prompt signal due to the annihilation of the positron in the target tank is observed at the scintillation detectors as a 0.5 MeV γ ray entering each detector tanks. Then, a delayed signal corresponding to the capture of the neutron by a cadmium atom in the water target is observed after $5\mu\text{s}$ from the first signal. The temporal correlation between the two signals together with the good agreement with the theoretical cross section of the reaction show an indirect detection of the neutrino. Later, in 1962, Leon Lederman, Melvin Schwartz and Jack Steinberger [69] found that there is more than one type of neutrino by detecting the muon anti-neutrino ($\bar{\nu}_\mu$) for the first time, through the reaction

$$\bar{\nu}_\mu + p \rightarrow n + \mu^+, \quad (2-2)$$

where μ^+ is the anti-muon. Finally, in 2000, The DONUT [70] collaboration found the third and final neutrino flavor, ($\bar{\nu}_\tau$) associated to the tau particle. The existence of this neutrino had already been predicted by measurements of the decay width of the Z -boson carried out by the LEP experiment at CERN [71]; which set to three the number of families in the standard model of elementary particles.

2.1.1

Neutrinos in the standard model

The SM is the mathematical theory that describes the weak, strong and electromagnetic interactions between leptons and-or quarks, the ultimate constituents of matter. It is based on the local symmetry group $SU(3)_C \times SU(2)_L \times U(1)_Y$, where the subscripts C , L and Y denote color, left-handed chirality and weak hypercharge, respectively. Each interaction is described by means of one symmetry: $SU(3)_C$ takes account of the strong interaction and it is the basis of the quantum chromodynamics (QCD) while $SU(2)_L \times U(1)_Y$ is associated with the electromagnetic and weak interactions described by the so-called electroweak theory, which combines the Fermi's theory of the weak interactions (i.e., β decay theory) with electromagnetism at high energies (~ 100 GeV) [72, 73, 74]; neutrinos interact only via weak interaction. In the standard model, we can identify two sectors: **Elementary fermions**, with particles that have spin 1/2 and obey the Fermi-Dirac statistics; therefore, they can form structures (e.g., hadrons which are made up of quarks). In this sector, elementary particles that have no internal structure are classified into

leptons and quarks. There are six leptons, three of them have an electric charge: the electron (e), the muon (μ) and the tau particle (τ); the other three are the neutrinos associated with each of the above particles: ν_e , ν_μ and ν_τ . On the other hand we have six quarks: up (u), down (d), charm (c), strange (s), top (t) and bottom (b). Both leptons and quarks are organized into three generations or families. Each generation is heavier than the previous one, which makes unstable the particles of the second and third generation and as a result they can decay into particles of the first generation.

$$1^{\text{st}} \text{ generation} \quad \begin{pmatrix} \nu_e \\ e^- \end{pmatrix}_L, \begin{pmatrix} u \\ d \end{pmatrix}_L, e_R^-, u_R, d_R, \quad (2-3a)$$

$$2^{\text{nd}} \text{ generation} \quad \begin{pmatrix} \nu_\mu \\ \mu^- \end{pmatrix}_L, \begin{pmatrix} c \\ s \end{pmatrix}_L, \mu_R^-, c_R, s_R, \quad (2-3b)$$

$$3^{\text{rd}} \text{ generation} \quad \begin{pmatrix} \nu_\tau \\ \tau^- \end{pmatrix}_L, \begin{pmatrix} t \\ b \end{pmatrix}_L, \tau_R^-, t_R, b_R. \quad (2-3c)$$

Neutrino decay has not yet been observed. A more detailed description of the topic will be presented in chapter 4. According to their chirality, fermions can be classified as right-handed or left-handed fermions (subscripts R and L in Eqs. (2-3)). For a massless particle, chirality and helicity² are equivalent, since negative (positive) helicity corresponds exactly to left (right) chirality. Charged leptons and quarks are Dirac particles as a consequence of the conservation of electric charge, therefore, they obey the Dirac equation and are described by complex four-component spinors $\Psi = \Psi_R + \Psi_L$, where Ψ_R and Ψ_L are the so-called right-handed and left-handed fields, respectively. Neutrinos play a special role in SM, they are massless particles because their negative helicity (anti-neutrinos have positive helicity) [75, 76, 77] therefore, they can be represented using two complex two-component spinors, called Weyl spinors. **Elementary bosons**, this sector includes the eight gauge bosons that correspond to the generators of $SU(3)_C$ which have a color charge, zero mass, are electrically neutral and are the force carriers of the strong interaction; the four gauge boson corresponding to the three generators of $SU(2)_L$ and one generator of $U(1)_Y$, of which W^\pm and Z^0 , the mediators of weak interactions, are massive while the photon (γ), the mediator of the electromagnetic interaction is massless. The Higgs boson is a scalar boson responsible for giving mass to bosons W^\pm , Z^0 and the charged fermions through

²Helicity is a measure of the projection of particle's spin onto the direction of its momentum. It is positive if spin and momentum are in the same direction, and negative if they point in opposite senses.

the Higgs mechanism. All the previous bosons have integer-spin (one for the gauge bosons and zero for the Higgs) and obey the Bose-Einstein statistics.

2.1.2

Neutrinos beyond standard model

Despite its great success in describing interactions between elementary particles, SM presents two main problems when describing neutrinos. First is that neutrinos have nonzero masses as evidenced by Super-Kamiokande (Super-K) [3], SNO [2] and KamLAND [5] neutrino oscillation analysis. Neutrinos are produced and detected as flavor-eigenstates ν_α ($\alpha = e, \mu, \tau$) which are linear superpositions of three neutrino mass-eigenstates ν_i ($i = 1, 2, 3$), where at least two of them have nonzero masses. However, neutrino oscillation experiments cannot determine the absolute value of these masses because they are only sensitive to mass-squared differences. Current neutrino data can be well fitted in terms of two of these differences: the solar mass splitting (Δm_{21}^2) and the atmospheric one (Δm_{31}^2). Thanks to matter effects in the Sun [2], we know that Δm_{21}^2 is positive, that is $m_2 > m_1$; here m_i ($i = 1, 2, 3$) are the mass eigenvalues associated to ν_i 's. On the other hand, we still do not know the sign of the atmospheric mass splitting, it is measured only via neutrino oscillations in quasi-vacuum or with weak matter effects which currently only give us its absolute value. As a consequence, two arrangements for the ordering of neutrino masses are considered: normal mass ordering (NMO)

$$m_1 < m_2 < m_3, \quad (2-4)$$

and inverted mass ordering (IMO)

$$m_3 < m_1 < m_2. \quad (2-5)$$

In the last decades, multiple experiments with different neutrino sources and detection technologies have confirmed the existence of neutrino oscillations and allows us to have a good understanding of the mechanism of neutrino oscillation as well as an excellent measure³ of the oscillation parameters, namely: the two mass splittings, the three mixing angles (θ_{12}, θ_{13} and θ_{23}) and the phase associated with CP violation (δ), whose value we do not know precisely. Table 2.1 shows the value of these parameters according to the most recent global fit to neutrino oscillation data performed by de Salas *et al.* [14]

³The current uncertainties of the relevant oscillation parameters [14] for our study of the Earth matter effects in the presence of neutrino decay, $\Delta m_{21}^2 = 7.50 \times 10^{-5} \text{ eV}^2$ and $\sin^2 \theta_{12} = 0.318$, are of a few percents ($\sim 3-4\%$), which means that these uncertainties have a negligible impact on our analysis.

Parameter	Best fit $\pm 1\sigma$	Mass Ordering
Δm_{21}^2	$(7.50_{-0.20}^{+0.22}) \times 10^{-5} \text{ eV}^2$	-
$ \Delta m_{31}^2 $	$(2.55_{-0.03}^{+0.02}) \times 10^{-3} \text{ eV}^2$	NMO
$ \Delta m_{31}^2 $	$(2.45_{-0.03}^{+0.02}) \times 10^{-3} \text{ eV}^2$	IMO
θ_{12}	$(34.3 \pm 1.0)^\circ$	-
θ_{13}	$(8.53_{-0.12}^{+0.13})^\circ$	NMO
θ_{13}	$(8.58_{-0.14}^{+0.12})^\circ$	IMO
θ_{23}	$(49.26 \pm 0.79)^\circ$	NMO
θ_{23}	$(49.46_{-0.97}^{+0.60})^\circ$	IMO
δ/π	$1.08_{-0.12}^{+0.13}$	NMO
δ/π	$1.58_{-0.16}^{+0.15}$	IMO

Table 2.1: Neutrino oscillation parameters summary. Adapted from de Salas *et al.* [14].

Contrarily to neutrino oscillation experiments, direct laboratory measurements of tritium beta decay can translate into upper bounds on neutrino masses. The KATRIN [24] experiment established the strongest bound to date for the electron-neutrino mass, $m_\beta < 1.1 \text{ eV}$ at 90% C.L..

Since

$$m_\beta^2 = m_1^2 + |U_{e2}|^2 \Delta m_{21}^2 + |U_{e3}|^2 \Delta m_{31}^2, \quad (2-6)$$

where U_{ei} ($i = 1, 2, 3$) denote the elements of the lepton mixing matrix⁴ and Δm_{31}^2 is positive for NMO and negative for IMO. A kinematic measurement of m_β , to a good approximation, measure m_1 independent from the mass ordering because $|U_{e3}|^2$ and Δm_{21}^2 are both quite small. Therefore, it is possible to constrain all three eigenmasses simultaneously. That is:

$$0 < m_1^2 < 1.2 \text{ eV}^2, \quad (2-7a)$$

$$7.5 \times 10^{-5} \text{ eV}^2 < m_2^2 < 1.2 \text{ eV}^2, \quad (2-7b)$$

$$2.6 \times 10^{-3} \text{ eV}^2 < m_3^2 < 1.2 \text{ eV}^2, \quad (2-7c)$$

for NMO and

$$2.5 \times 10^{-3} \text{ eV}^2 < m_1^2 < 1.2 \text{ eV}^2, \quad (2-8a)$$

$$2.6 \times 10^{-3} \text{ eV}^2 < m_2^2 < 1.2 \text{ eV}^2, \quad (2-8b)$$

$$0 < m_3^2 < 1.2 \text{ eV}^2, \quad (2-8c)$$

for IMO. Eqs. (2-7) and (2-8) show that current oscillation data constrain the sum of the neutrino masses

⁴ Matrix which allows to describe the flavor eigenstates as mixtures of the mass eigenstates.

$$m_{tot} = \sum_i m_i, \quad (2-9)$$

to be $> 5.96 \times 10^{-2} \text{ eV}$ ($> 0.1 \text{ eV}$) for NMO (IMO). While KATRIN measurements constrain $m_{tot} < 3.3 \text{ eV}$ in either mass ordering, cosmological observations can also put bounds on m_{tot} thanks to the fact that the presence of massive neutrinos affects the evolution of cosmic microwave background (CMB) fluctuations and suppresses the structure formation at small scales [78]. To get an idea of this upper limit on the sum of neutrino masses, let us first look at the decoupling of neutrinos from thermal equilibrium in the early universe. This happens at temperatures $\mathcal{O}(1) \text{ MeV}$ while neutrinos are still relativistic particles (radiation); their contribution to the total energy density of the universe is given by

$$\rho_\nu \simeq m_{tot} (3/11)(3.045/3)^{3/4} n_\gamma, \quad (2-10)$$

where the factor $3/11$ is the ratio of neutrinos to photons, $(3.045/3)^{3/4}$ is a correction to the effective number of neutrinos in the SM when it is taken into account the heating of γ by e^+e^- annihilation during neutrino decoupling and $n_\gamma = 410.7 \text{ cm}^{-3}$ is the number density of CMB photons. Demanding that the energy density of neutrinos today does not exceed the known value of energy density of matter we obtain

$$m_{tot} < 93 \text{ eV } \Omega_m h^2, \quad (2-11)$$

where Ω_m is the cosmological fraction of matter and h is the dimensionless Hubble parameter. The most strongest constraint to date on m_{tot} is obtained from the observation of CMB, the distribution of clusters of galaxies and the Lyman- α forest, baryon acoustic oscillation (BAO), and Hubble parameter data. These combination gives an upper bound $m_{tot} < 0.111 \text{ eV}$ at 95% C.L. [79]. It should be noted that in the presence of other light particles (e.g., sterile neutrinos) or new neutrino interactions (e.g., neutrino decay), the bound on m_{tot} can be relaxed, we refer the reader interested in this topic to the work of M. Escudero *et al.* [80].

The second problem is the neutrino nature, they can be Dirac or Majorana particles. A Dirac neutrino is the one whose particle and antiparticle represent two different particles while a Majorana neutrino is the one that is its own antiparticle which leads to reactions where lepton-number conservation is not an exact law of nature and has to be violated. Most of the experiments aimed at solving this enigma focus in the search for neutrinoless double beta decay ($0\nu\beta\beta$) process. This is an isobaric SM-forbidden transition in which a parent nucleus (A, Z) decay to a daughter nucleus ($A, Z + 2$) by two

simultaneous beta decays, This causes the atomic number (Z) of the daughter nucleus to increase by two units; while the mass number (A) is conserved. In the $0\nu\beta\beta$ decay two electrons accompany the transition

$$(A, Z) \rightarrow (A, Z+2) + 2e^- + Q_{\beta\beta}, \quad (2-12)$$

where $Q_{\beta\beta}$ is the energy released. Because the neutrinos involved in the process are Majorana particles, the two neutrinos obtained from the β decays annihilate each other. Therefore, the lepton number is violated by two units ($\Delta L = 2$). Table 2.2 shows the isotope half-life $T_{1/2}^{0\nu}$ for the process and the Majorana mass $|m_{\beta\beta}|$ limits from the most recent experiments

So far $0\nu\beta\beta$ has not been observed, however, future experiments such as LEGEND [17, 18, 19], CUPID [20], SNO+ [21], nEXO [22], NEXT [23], KamLAND2-Zen 800 [92] will have a good discovery probability: a better than 50% for normal mass order (NO) and almost 100% for inverted mass order (IO) after 5 years lifetime [95].

Isotope	$T_{1/2}^{0\nu} (\times 10^{25} \text{ years})$	$ m_{\beta\beta} \text{ (eV)}$	Experiment
^{48}Ca	$> 5.8 \times 10^{-3}$	$< 3.5 - 22$	ELEGANT-IV [82]
^{76}Ge	> 18	$< 0.079 - 0.180$	GERDA [83]
	> 2.7	$< 0.200 - 0.433$	M. DEMONSTRATOR [84]
^{82}Se	$> 3.6 \times 10^{-2}$	$< 0.89 - 2.43$	NEMO-3 [85]
^{96}Zr	$> 9.2 \times 10^{-4}$	$< 7.2 - 19.5$	NEMO-3 [86]
^{100}Mo	$> 1.1 \times 10^{-1}$	$< 0.33 - 0.62$	NEMO-3 [87]
^{116}Cd	$> 1.0 \times 10^{-2}$	$< 1.4 - 2.5$	NEMO-3 [88]
^{130}Te	> 3.2	$< 0.075 - 0.350$	CUORE [89, 90]
^{136}Xe	> 10.7	$< 0.061 - 0.165$	KamLAND-Zen [91, 92]
	> 3.5	$< 0.093 - 0.286$	EXO-200 [93]
^{150}Nd	$> 2.0 \times 10^{-3}$	$< 1.6 - 5.3$	NEMO-3 [94]

Table 2.2: Half-life and Majorana mass limits from recent experiments. From Formaggio *et al.* [81].

2.1.3

Neutrino sources

Depending on the origin, we can classify neutrino sources into two large groups: natural and man-made. The first includes neutrinos from the Big-Bang, the Sun, natural radioactivity sources, supernovae, atmosphere and extra-terrestrial high energy neutrinos sources whereas the second takes into account neutrinos created in reactors and accelerators [96].

Neutrinos from Big-Bang constitute the so-called cosmic neutrino background (CNB) and no signal has been identified to this date [97]. They are a relic from the early universe when it was a second old and its temperature was ~ 1 MeV. At this temperature the rate of weak interactions began to be slower than the expansion of the universe, and finally, the neutrinos decoupled from matter as well as from radiation, and cooled as the universe expanded. It is estimated that today there are ~ 112 neutrinos (neutrinos + anti-neutrinos per flavor) per cubic centimeter with an uniform temperature of $1.945 \text{ K} \sim 1.6 \times 10^{-4} \text{ eV}$ [98].

The Sun is one of the most important natural sources that we have for neutrino research. This, like all other stars, is able to create its own energy by nuclear fusion inside its core, process in which hydrogen nuclei are converted into helium-4 nuclei. There exist two well-known processes that ultimately result in helium-4, the most important in small stars like our sun is known as proton-proton chain. In this process, first two protons fuse into deuterium⁵, which later can fuse with another proton to form helium-3, the light isotope of helium. Finally, in a period of approximately 400 years, the nuclei of helium-3 become helium-4 through four possible paths or branches of the process, which are denoted as: p-p I, p-p II, p-p III and p-p IV [99, 100]. Since neutrinos interact weakly with matter, they do not contribute significantly to counteract gravitational collapse by deposition of energy in the solar interior. Therefore, solar electron neutrinos carry away approximately 2.3% of the total nuclear energy produced, implying a solar electron neutrino production (N_{ν_e}) of

$$N_{\nu_e} = 2 \times \frac{L_{\odot}}{26.73 \text{ MeV} - 2 \langle E_{\nu_e} \rangle} = 1.83 \times 10^{38} \text{ s}^{-1}, \quad (2-13)$$

where 26.73 MeV is the total energy yield of a complete p-p chain, the factor 2 is the number of neutrinos per fusion, $L_{\odot} = 2.39 \times 10^{38} \text{ MeV s}^{-1}$ is the solar luminosity without neutrinos and $\langle E_{\nu_e} \rangle$ is the averaged energy of the solar neutrinos. With this value, it is expected an ν_e flux of $\sim 6.51 \times 10^{10} \text{ cm}^{-2} \text{ s}^{-1}$ at Earth; the energy of solar neutrinos range from hundreds of keV to tens of MeV. On the other hand, CNO-cycle, the other series of fusion reactions, only contributes 1.5% to the total nuclear energy produced in the Sun [101].

Geoneutrinos are electron anti-neutrinos produced by natural radioactive decays inside the Earth and constitute a new tool in order to study the interior of our planet [102]. One of the most important tasks of geophysics is to understand the Earth's thermal evolution; since its formation the Earth has been cooling, however the decay of radioactive elements with lifetime

⁵This process can take around 9 billion years to occur.

comparable with the age of the Earth such as isotopes in the ^{238}U ($\tau_{1/2} = 4.47 \times 10^9$ year) decay series, isotopes in the ^{232}Th ($\tau_{1/2} = 14.0 \times 10^9$ year) decay series and ^{40}K ($\tau_{1/2} = 1.28 \times 10^9$ year) constitute a continuing heat source. The heat flow from the interior of the Earth has been measured using temperature gradient and conductivity measurements and setting to 44.2 ± 1.0 TW [103, 104]. Currently, only KamLAND and Borexino have been able to measure geoneutrinos. The authors of Ref. [105], by combining measurements of the geoneutrino flux from these two experiments, found that the decays

$$^{238}\text{U} \rightarrow ^{206}\text{Pb} + 8\alpha + 8e^- + 6\bar{\nu}_e + 51.7 \text{ MeV}, \quad (2-14a)$$

$$^{232}\text{Th} \rightarrow ^{208}\text{Pb} + 6\alpha + 4e^- + 4\bar{\nu}_e + 42.7 \text{ MeV}, \quad (2-14b)$$

contribute together with $20_{-8.6}^{+8.8}$ TW to Earth's heat flux, indicating that it is roughly half of Earth's total heat flux and therefore an indication that Earth's primordial heat has not yet been exhausted. Geoneutrinos energies range from keV to a few MeV.

Core-collapse supernovae (CCSNe) are another interesting source of neutrinos, where almost all the energy (99%) released by gravitational collapse is radiated away as neutrinos and anti-neutrinos of all flavors with energies of a few tens of MeV. So far only neutrinos from supernova SN1987A at the Large Magallanic Cloud, a dwarf satellite galaxy of the Milky Way, have been detected. The neutrino signal was observed by four underground detectors, namely Kamiokande-II [106], IMB [107], Baksan [108] and LSD [109]. The first three observed the CCSN burst at roughly the same time, while LSD reported the signal 4.5 hours earlier than Kamiokande-II, for this reason its data is not taken into consideration in the different analyzes of SN1987A. The Kamiokande-II detector recorded the first event at 7 : 35 : 35 UT (standard for universal time) on 23 February 1987. In total Kamiokande-II observed 12 events in a lapse of time of ~ 12 seconds while IMB observed 8 events in a lapse of ~ 6 seconds, being the first event recorded at 7 : 35 : 41.37 UT on the same day. Despite the limited number of observed events, the data showed compatibility with the expected values for a neutrino-driven CCSN explosion. Among the most relevant characteristics, it was obtained that the duration of the signal, a few seconds, was consistent with the expected neutrino-cooling time of the newly formed proto-neutron star (PNS), and also the total energy carried away by the neutrinos was of the expected order of the gravitational binding energy [106]. On the other hand, the detection of SN1987A neutrinos allowed to put strong constraints on the lifetimes, the masses and magnetic moments of the neutrinos and also to constraint some more exotic scenarios.

Together with solar neutrinos, atmospheric neutrinos are another very important source for neutrino research whose results have allowed us to focus our attention beyond the panorama offered by the standard model of elementary particles. Atmospheric neutrinos are produced by cosmic rays, accelerated charged particles like electrons, protons and heavier nuclei, interacting with the Earth or Sun atmosphere [110, 111, 112]. As a result of this interaction, a secondary particle flux that includes neutrinos is produced. Neutrinos created by cosmic rays have an energy range varying from MeV to TeV and are generated by the following decays:

$$\pi^\pm \rightarrow \mu^\pm + \nu_\mu (\bar{\nu}_\mu) \quad (2-15a)$$

$$\mu^\pm \rightarrow e^\pm + \nu_e (\bar{\nu}_e) + \bar{\nu}_\mu (\nu_\mu), \quad (2-15b)$$

$$K^\pm \rightarrow \mu^\pm + \nu_\mu (\bar{\nu}_\mu). \quad (2-15c)$$

Kaons can also decay into three bodies, such as $K^\pm \rightarrow \pi^0 + e^\pm + \nu_e (\bar{\nu}_e)$ or decay purely into pions, for example $K^\pm \rightarrow \pi^\pm + \pi^0$ which finally produce neutrinos. In a historical context, atmospheric neutrinos played a fundamental role in confirming neutrino oscillations by means of Super-Kamiokande measurements.

High-energy neutrinos are produced by cosmic-ray interactions in the source, its surroundings or during cosmic-ray propagation to Earth. Possibly sources include extragalactic jets, star-forming galaxies (SFGs), gamma-ray bursts (GRBs), active galactic nuclei (AGNs) and galaxy clusters [113, 114, 115, 116, 117]. These neutrinos have energies between few TeV to PeV and the longest baselines, thus providing a unique scenario to study physics beyond the standard model, for example neutrino decay. Neutrinos with these energies can be produced by proton-proton (pp) or proton-photon (p γ) high-energy interactions, which produce secondary particles (pions and muons) that can decay into neutrinos, according to the production channels given in Eqs. (2-15).

Neutrinos produced in accelerators are typically electron-or muon neutrinos (and their antiparticles). Current accelerators use conventional neutrino beam concept for their artificial neutrino beams [118]. The process begins with protons which are accelerated, close to the speed of light, until obtaining a GeV-scale energy, then they are impacted on a graphite or beryllium target. The collision creates numerous particles, among them pions, whose decays produce a beam of high-purity ν_μ (or $\bar{\nu}_\mu$, since charged pions are electrically charged particles, it is possible to use magnetic fields to choose whether the beam will be made up of neutrinos or antineutrinos.) in an energy range

varying from hundreds of MeV to hundreds of GeV. Current conventional-neutrino-beam sources are the 8 GeV Booster Beam at Fermilab (~ 800 MeV ν_μ) [119], the 60-120 GeV highly configurable "Neutrinos at the Main Injector" (NuMI) and "Long Baseline Neutrino Facility" (LBNF) beam line facilities at Fermilab (ν_μ beams in the range of a few to tens of GeV) [120] and the 30 GeV J-PARC (600 MeV ν_μ) [121]. Another source of man-made neutrinos is the Large Hadron Collider (LHC) at the CERN, the world's largest and most powerful particle accelerator, that is currently preparing for run-3 which will start in 2022 [122, 123, 124].

Last, but not least neutrino source, we have the commercial nuclear reactors. Which release a few percent of their energy production in $\bar{\nu}_e$ with energies in the range from keV to a few MeV. There are two really valuable characteristics that make reactor neutrinos an important source in the study of the neutrino properties, the first is that nuclear reactors produce large quantities of neutrinos and the second is that reactor neutrinos come in only one flavor. Among the most outstanding achievements in this sector is the measurement of θ_{13} announced in the middle of 2012 by Double Chooz [8, 125], Daya Bay [126, 127] and RENO [128, 129].

Due to their vast range of energies (from a few eV to hundreds of TeV) and the fact that these particles (neutrinos) interact weakly with matter, we can explore our universe in greater depth as well as gain information about the physics of this particle.

2.2

Supernovae

A supernova (SN) is a stellar explosion that marks the death of some stars. These explosions are one of the most violent and largest that take place in the universe, being possible to be observed even with the naked eye for a period of time that can last from several weeks to several months; they are characterized by rapidly increasing their brightness until they reach a maximum where they can emit nearly as much light as the whole galaxy where the explosion takes place, subsequently their brightness decreases smoothly until it disappears completely from the sky. Initially these events were called as Novae (new stars⁶). However, as the study of extragalactic objects was growing,

⁶A nova is not a new star in the strict sense of the word, but refers to a star that was not noticed until it exploded and therefore, when its brightness is so intense that it can even be seen with the naked eye. This happens when in a binary system formed by a white dwarf star and a red giant, part of the material of the giant star is attracted by the gravity of the dwarf star; As more material accumulates on the surface of the latter, the temperature

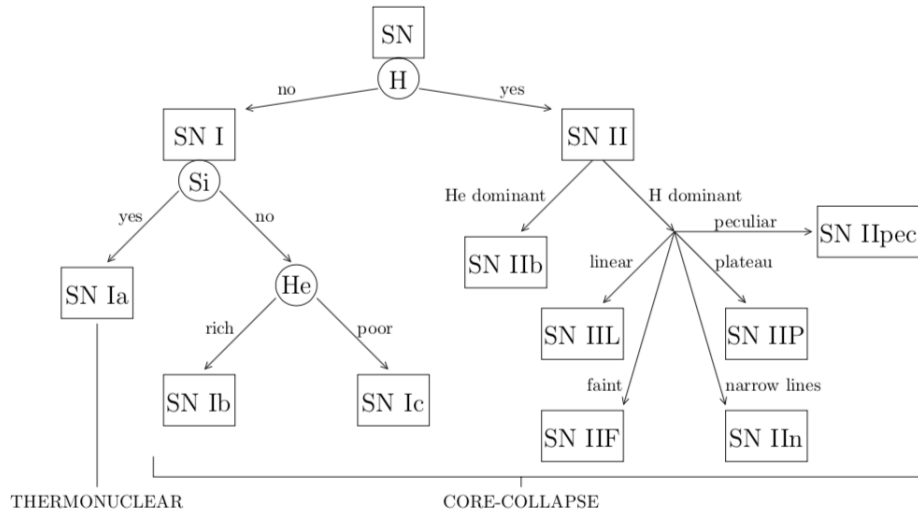


Figure 2.1: Supernovae classification [156].

it was observed that a distinction should be made between the brighter and fainter novae. In 1934, Walter Baade and Fritz Zwicky in their article entitled "On Super-Novae" proposed to use the word *super-novae* to denote the brightest, those with a more negative value of their absolute brightness [130].

Observationally, astronomers classify SNe types by their optical spectra and the properties of their light curves using the Minkowski-Zwicky system [131]. According to this system (see Fig.2.1), SNe that do not show hydrogen lines in their optical spectrum are called type I supernovae (SNe I) while those in which the hydrogen lines are present are called type II supernovae (SNe II).

SNe I present a spectroscopic sub-classification distinguishing three subtypes Ia and Ib/Ic depending on the absence or the presence of silicon lines in the spectrum. Further, the types Ib and Ic that have not silicon lines differ from each other because SNe Ib are richer in He than those of type Ic.

Similarly, SNe II also present more sub-classifications: IIb if helium dominates over hydrogen, IIL if the decrease of the luminosity is approximately linear in time, IIF if the SN is faint, IIn if the spectrum shows narrow line emissions, IIP if the time evolution of the luminosity shows a plateau and IIpec if the SN has peculiar characteristics.

However, for the objectives outlined in this work it is more important the

increases enough to rapidly transform large amounts of hydrogen and helium into heavier elements through nuclear fusion. As a consequence, a thermonuclear explosion occurs that releases material from the outermost layers of the dwarf star. Unlike what happens with the SN progenitor, the white dwarf can generate multiple explosions of this type as long as the red giant has material to deposit on its surface.

mechanism that generates the supernovae, which distinguishes SNe Ia from the others (Ib, Ic, and II). SNe Ia are the result of the thermonuclear explosion of a carbon-oxygen white dwarf. A white dwarf is a stellar remnant that is generated when a star of mass less than $\sim 8 M_{\odot}$ has exhausted its nuclear fuel. 97 % of stars in the mass range indicated above develop carbon-oxygen nuclei at the end of their stellar evolution. At this point, the star does not have an energy source capable of stopping the gravitational collapse, so the star is compressed on itself which makes the density at its core reach orders of $\sim 10^6 \text{ g/cm}^3$. Now, the electrons in the nucleus degenerate and their pressure stops the collapse as long as the mass of the white dwarf does not exceed the Chandrasekhar mass which depends on the number of electrons per nucleon (Y_e). For a typical white dwarf $Y_e = 0.5$ and the Chandrasekhar mass is $\sim 1.4 M_{\odot}$. If the white dwarf has a close companion star from which it can gain mass, for example a red giant, the pressure of the degenerate electrons will not be enough to support the collapse. After exceeding Chandrasekhar's mass limit, the white dwarf becomes unstable which restores the fusion of carbon and oxygen into heavier nuclei, As a result of these reactions large amounts of energy are released which eventually leads to an explosion that only leaves behind a planetary nebula whose optical spectrum exhibits silicon lines and the presence of ^{56}Fe , a product of the radioactive decay chain $^{56}\text{Ni} \rightarrow ^{56}\text{Co} \rightarrow ^{56}\text{Fe}$ [132].

As we have just seen, mass is the main determinant of a star fate. Stars with mass greater than $\sim 8 M_{\odot}$ produce core-collapse supernovae (CCSNe); in this category we find supernovae of type Ib, Ic and II. During their stay in the main sequence, stars spend most of their lives transforming hydrogen and helium at their cores. Only until the end of their lives, massive stars pass through all the stages of nuclear fusion (H, He, C, O, Ne, Si) to form an iron core of $\sim 1 M_{\odot}$. For CCSNe typical main-sequence lifetimes are given by

$$t_{ms} \approx 10 \left(\frac{M}{M_{\odot}} \right)^{-2.5} \times 10^9 \text{ yr} \leq 3 \times 10^7 \text{ yr}, \quad (2-16)$$

where M is the progenitor mass. From Eq. (2-16) we conclude that CCSNe are associated with young stars while SNe Ia due to the small mass of their progenitors are associated with old stars.

According to the mass of the core of a collapsing star, after the explosion there will be a neutron star or a black hole as a remnant (i.e., if its mass is greater than $\sim 3 M_{\odot}$). From now on and throughout this work, we will only consider CCSNe whose progenitor mass leads to the formation of a neutron star, $10 M_{\odot} \leq M \leq 25 M_{\odot}$. The newly formed neutron star is a highly efficient

source of neutrino and anti-neutrino production of all flavors. The whole CC-SNe neutrino burst is emitted in a time window of a few seconds, this signal arrives to Earth before than its electromagnetic counterpart, since neutrinos interact weakly with matter in the SN environment.

2.2.1

Core collapse mechanism

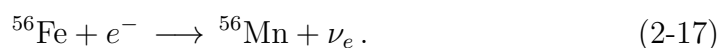
Despite the large number of supernovae that have been optically observed to date, the mechanism that leads a massive star to explode like CCSN is not precisely known. The information obtained from the electromagnetic spectrum of the star only gives information on its surface layers. Neutrinos, being particles that weakly interact with matter, play a crucial role in understanding the dynamics of the star's explosion, which takes place in the core [133]. There are two possible scenarios that account for the explosion mechanism: the prompt and the delayed explosion. The latter has been extensively studied through numerical simulations in one, two and three dimensions [134, 135, 136, 137, 138, 139].

In the prompt explosion, the envelope of progenitor star is ejected by the shock wave ~ 10 ms after the core bounce formation. Numerical simulations have shown that this mechanism work only when the progenitor mass is small, $\sim 10 M_{\odot}$. In contrast, in the delayed explosion, the shock wave loses energy through electron capture and photodissociation processes and then stalls. The stalled shock wave is revived by neutrino energy deposition on the region that the wave leaves behind. In the following we describe in more detail the main stages of this mechanism [133].

2.2.1.1

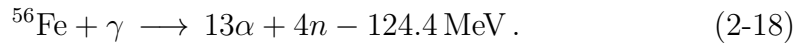
Initial phase of collapse

At the end of silicon burning, the Fermi energy of electrons in the contracting core increases to the point that its value is enough to establish electron captures by nuclei and free protons. At densities above $\sim 10^{10}$ g cm $^{-3}$, iron nuclei will capture electrons by the reaction:



According to Eq. (2-17), we can intuit that in the initial phase of the collapse more electron neutrinos are produced; this process is known as neutronization. So far, the star has avoided the collapse of its core mainly due to the pressure

of the degenerate relativistic electron gas and in small proportion by the remaining thermal pressure in the core. However, each capture decreases the lepton number by one, consequently the star becomes unstable. Let us remember that neutrinos are weak interacting particles, therefore, despite the high degree of compression of the core, they can easily escape carrying with them a significant amount of energy, this increases the instability of the core. Another endothermic reaction that exhausts the internal energy and therefore reduces the thermal pressure support is the partial disintegration of iron-material by high energy photons,



The electron-capture and photodisintegration of nuclei processes finally lead to core collapse. This occur as soon as the mass of the core exceeds $\sim 1.4 M_{\odot}$ [133, 140, 141].

2.2.1.2

Neutrino trapping

As the average core density reaches $\sim 10^{12} \text{ g cm}^{-3}$, the core begins to become opaque to neutrinos, mainly as a consequence of elastic scattering of neutrinos on nucleons. At this point, the neutrino mean free path becomes smaller than the size of the iron core. Finally, the neutrino diffusion time scale is longer than the collapse free-fall time scale, thus trapping neutrinos inside the so-called neutrinosphere where neutrinos are in thermal equilibrium in a degenerate Fermi sea and diffuse from hot to cold regions. At this point the neutrino flux begins to decrease [133, 142].

2.2.1.3

Bounce and shock propagation

When the collapsing core reaches densities of $\sim 10^{14} \text{ g cm}^{-3}$, the core becomes highly incompressible as a consequence of the repulsive nucleon-nucleon interaction, then the collapse of the inner core stops abruptly, but this does not happen beyond the point where the speed of sound equals the infall velocity. Since the outer core collapses at supersonic velocities, material from the outer core keeps falling and bounces off the inner core; this process creates waves that spread out the inner core. Their propagation slows down as they leave the central part of the star, stopping just at the border of the inner core. As more material fall in, more waves are produced and in a fraction

of a millisecond they are at the boundary between the two central regions of the star. Here, the continuous deposition of energy increases the pressure in the area and creates what is commonly known as a shock wave, which now propagates out of the outer core.

As the wave propagates it breaks the atomic nuclei into nucleons, losing ~ 8.8 MeV per nucleon. The wave gradually weakens and finally stalls at a radial distance of 100 - 200 km, this happens about 200 ms after starting the collapse. Although more particles are produced in this process, the energy cost is quite high that leads to a decrease in temperature and pressure. The newly created protons can quickly capture electrons by the reaction



where the emitted neutrinos can escape carrying energy from the star. On the other hand, when the shock wave passes through the sphere where neutrinos were trapped, a huge emission of electron neutrinos, known as neutronization burst, occurs in a very short period of time of ~ 20 ms. During this time approximately 1% of the total binding energy is emitted [143, 144].

2.2.1.4

Accretion phase and delayed explosion

As the shock wave propagates, the material just behind the wave has a low concentration of degenerate electrons, which makes possible the thermal creation of relativistic positrons and with them the creation of electron anti-neutrinos by the reaction:



The other flavors are produced by way of thermal mechanisms that act via the annihilation of virtual and real pairs $e^{+} e^{-}$. Among them, we have:

1. electron pair annihilation $e^{-} + e^{+} \longrightarrow \nu + \bar{\nu}$,
2. plasmon decay $\gamma^{*} \longrightarrow \nu + \bar{\nu}$,
3. photoannihilation $\gamma + e^{\pm} \longrightarrow e^{\pm} + \nu + \bar{\nu}$,
4. electron-nucleon bremsstrahlung $e^{\pm} + N \longrightarrow N + e^{\pm} + \nu + \bar{\nu}$,
5. nucleon-nucleon bremsstrahlung $N + N \longrightarrow N + N + \nu + \bar{\nu}$,

where N stands for a nucleon.

As we discussed, the shock wave stalls ~ 200 ms after starting the collapse. Their fronts define a region called the gain layer, which consists of the region that the shock wave has left behind. In this region, neutrinos deposit energy via inverse beta decays. When the deposited energy is high enough, this mechanism revives the shock wave and explodes the star [145, 146].

2.2.1.5

Cooling phase of neutron star

The cooling phase lasts a few tens of seconds and become important 0.5 s after core bounce. During this time window more than 90% of the gravitational binding energy of the newly formed proto-neutron star (PNS) is realased via neutrino emission of all flavors⁷. This quickly reduces the temperature of the PNS. The cooling phase ends when the core temperature drops below $\sim 10^{10}$ K , then the PNS becomes transparent to neutrinos.

2.2.2

CCSN neutrino spectra

Intuitively, it would be thought that the CCSN neutrino spectrum could be described with a Fermi-Dirac distribution since they are thermally emitted. However, because the neutrino opacity within the proto-neutron star depends on the neutrino energy, therefore, the emergent spectrum differs somewhat from a pure Fermi-Dirac distribution (i.e., with zero chemical potential), both the low- and high-energy tails are suppressed compared to the spectrum obtained by a Fermi-Dirac distribution without chemical potential [148].

Deep in the proto-neutron star, the opacity of both the electron neutrino and electron anti-neutrino are dominated by their charged current interactions with nucleons, that is the inelastic scattering β -processes $\bar{\nu}_e + p \rightarrow n + e^+$ and $\nu_e + n \rightarrow p + e^-$. These interactions keep ν_e and $\bar{\nu}_e$ in local thermal equilibrium (LTE). However, since the density of the PNS decreases as the neutrinos leave their central part, these interactions are less and less frequent, in addition the inverse beta decay cross sections increase with neutrino energy. Consequently, depending on the neutrino energy, the processes β become inefficient at some radius. This defines a set of energy dependent spheres where neutrinos are in LTE, which are commonly known as neutrino spheres. From which ν_e and $\bar{\nu}_e$ can propagate freely. Since there is not an unique neutrino sphere for each

⁷It is expected that the bulk ($\sim 90\%$) of the neutrinos that reach our detectors come from process $e^+ + e^- \rightarrow \nu + \bar{\nu}$, which is dominant in the cooling phase [147].

flavor, the emergent neutrino spectrum cannot be described using a thermal distribution (i.e., Fermi-Dirac distribution).

Due to its nature, the mantle of the proto-neutron star contains more neutrons than protons, which leads ν_e to interact more with matter than $\bar{\nu}_e$, therefore the neutrino spheres associated with ν_e have radii larger than the $\bar{\nu}_e$ spheres. This can be interpreted as: electron anti-neutrinos have an average energy greater than electron neutrinos.

On the other hand, ν_x ($x = \mu, \tau$) interacts with matter by neutral currents. In the innermost region of the proto-neutron star ν_x 's are mainly in LTE by bremsstrahlung, neutrino pair annihilation and electron pair annihilation processes. After some energy-dependent radius these interactions stop and ν_x can no longer be in LTE, this boundary defines the ν_x neutrino spheres. But the ν_x transport has a more complex picture than the electron neutrino counterpart, beyond their neutrino spheres ν_x can still exchange energy with the medium by $N + \nu_\mu \rightarrow N + \nu_\mu$ and $e^\pm + \nu_\mu \rightarrow e^\pm + \nu_\mu$ reactions. These processes define two more spheres the energy and transport spheres. The first ends at the radius where scattering on e^\pm does not work and the second where scattering on nucleons become inefficient. From this point on, ν_μ start streaming freely. Since the above mentioned neutral current interactions have a low rate compared to the charged current ones, ν_μ sphere radii are the smallest among the others. From the numerical results based on complex simulations [134, 135, 136, 137, 138, 139, 140], we expect that from the accretion phase the following hierarchy will be established in the average energy,

$$\langle E_{\nu_e} \rangle < \langle E_{\bar{\nu}_e} \rangle < \langle E_{\nu_x} \rangle. \quad (2-21)$$

The un-oscillated neutrino energy spectrum $\varphi_\nu^0(E_\nu) \equiv dN_\nu/dE_\nu$ at a given time can be satisfactorily described using a quasi-thermal spectrum. Throughout the literature it is common to use a "pinched Fermi-Dirac distribution" characterized by an effective temperature (T_ν) and a chemical potential (η) [148], that is

$$\varphi_\nu^0(E_\nu) = \frac{1}{T_\nu^4} \frac{E_\nu^2}{f_3(\eta_\nu) e^{E_\nu/T_\nu - \eta_\nu} + 1}, \quad (2-22)$$

where $\nu = (\nu_e, \nu_\mu, \nu_\tau)$ in the standard notation, E_ν is the neutrino energy and the function $f_n(\eta_\nu)$ is defined by

$$f_n(\eta_\nu) \equiv \int_0^\infty \frac{x^n}{e^{x - \eta_\nu} + 1} dx. \quad (2-23)$$

The interpretation of T_ν and η is more complicated because the emergent spectra is not thermal. In a crude approximation $\langle E \rangle / T_\nu \simeq 3.1514 + 0.1250\eta + 0.0429\eta^2 + \mathcal{O}(\eta^3)$ where the parameter η is used to describe the

pinch effect [149]. Typical values of η are $\eta_{\nu_e} \simeq 2$, $\eta_{\bar{\nu}_e} \simeq 3$, $\eta_{\nu_x} \simeq 1$.

Another way to describe the CCSN neutrino energy spectra is to use the analytic two-parameter fit given in Ref. [149, 150]

$$\varphi_\nu^0(E_\nu) = \frac{(1 + \alpha_\nu)^{1+\alpha_\nu}}{\langle E_\nu \rangle \Gamma(1 + \alpha_\nu)} \left(\frac{E_\nu}{\langle E_\nu \rangle} \right)^{\alpha_\nu} \exp \left(-\frac{(1 + \alpha_\nu) E_\nu}{\langle E_\nu \rangle} \right), \quad (2-24)$$

where $\Gamma(1 + \alpha_\nu)$ is the Gamma function. The energy-shape parameter

$$\alpha_\nu \equiv \frac{2 \langle E_\nu \rangle^2 - \langle E_\nu^2 \rangle}{\langle E_\nu^2 \rangle - \langle E_\nu \rangle^2}, \quad (2-25)$$

takes into account the deviation from a thermal spectrum, for example it has a value of $\alpha_\nu = 2.3$ ($\alpha_\nu = 2$) for a Fermi-Dirac (Maxwell-Boltzmann) distribution. In general, $\langle E_\nu \rangle$, α_ν and also the neutrino luminosity L_ν are time-dependent functions, and are directly extracted from the simulations. According to Ref. [151], the neutrino fluence (time-integrated neutrino spectra) at Earth can be computed as

$$F_\nu^0(E_\nu) = \frac{\epsilon_\nu}{4\pi D^2 \langle E_\nu \rangle} \widehat{\varphi_\nu^0(E_\nu)}, \quad (2-26)$$

where D is the distance between the CCSN and the Earth, $\epsilon_\nu = \int_{t_0}^{t_1} dt L_\nu(t)$ is the total energy carried by each neutrino flavor from time t_0 to t_1 , the time-averaged mean energy is given by

$$\widehat{\langle E_\nu \rangle} = \frac{\int_{t_0}^{t_1} dt L_\nu(t)}{\int_{t_0}^{t_1} dt L_\nu(t) / \langle E_\nu \rangle(t)}, \quad (2-27)$$

and to obtain $\widehat{\varphi_\nu^0(E_\nu)}$, we only replace both $\langle E_\nu \rangle$ and α_ν by $\widehat{\langle E_\nu \rangle}$ and $\widehat{\alpha_\nu} = \int_{t_0}^{t_1} dt \alpha_\nu(t) / (t_1 - t_0)$ in Eq. (2-24).

Hereafter, in this work Eq. (2-26) will be used to calculate the unoscillated CCSN neutrino spectra. Table 2.3 lists the fitting parameters of Eq. (2-24) for the time-integrated neutrino spectra that will be used in this thesis. The scenarios A, B, C_n ($n = 1, 2, 3$ for the neutronization burst, accretion and cooling phases, respectively.) and D corresponding to a CCSN neutrino emission are based on the $20 M_\odot$ progenitor model simulated by Totani *et al.* [148], the accretion phase of a Garching simulation for a $15 M_\odot$ progenitor [152, 153], the results obtained by Fischer *et al* [154] for a $18 M_\odot$ progenitor and the MC (Monte Carlo) study of spectral formation by Keil *et al* [149], respectively.

Scenario	ν flavor	ϵ_ν [10^{50} erg]	$\langle E_\nu \rangle$ [MeV]	$\widehat{\alpha}_\nu$
A (all phases, $t_{pb} \leq 10$ s)	ν_e	462.2	12.3	3.8*
	$\bar{\nu}_e$	485.9	15.8	3.8
	ν_x	478.7	22.3	1.8
B (accretion, $t_{pb} \leq 0.25$ s)	ν_e	92.48	10.7	3.7*
	$\bar{\nu}_e$	87.77	13.4	3.5
	ν_x	59.64	14.1	2.6
C ₁ (ν_e burst, $t_{pb} \leq 10$ ms)	ν_e	21.51	12.6	3.0
	$\bar{\nu}_e$	0.354	10.7	3.0
	ν_x	1.325	15.9	3.0
C ₂ (accretion, $t_{pb} \leq 0.4$ s)	ν_e	142.6	9.4	3.4
	$\bar{\nu}_e$	137.2	11.7	4.0
	ν_x	78.34	15.7	2.0
C ₃ (cooling, $t_{pb} \geq 1$ s)	ν_e	142.6	8.8	2.8
	$\bar{\nu}_e$	137.8	10.4	1.9
	ν_x	163.2	11.1	1.5
D (accretion)	ν_e	-	13.0	3.4
	$\bar{\nu}_e$	-	15.4	4.2
	ν_x	-	15.7	2.5

Table 2.3: CCSN neutrino emission model parameters used in this work. Values with an asterisk as superscript denote that $\widehat{\alpha}_{\nu_e} = \widehat{\alpha}_{\bar{\nu}_e}$ was assumed.

The values of $\widehat{\alpha}_\nu$ for the scenarios A and C_n (with $n = 2, 3$) were taken from Refs. [155] and [60], respectively. Since it was not possible to obtain such information for the scenario C₁, we get by setting $\widehat{\alpha}_\nu = 3$ for all flavors, as in Ref. [151]. Also, the totally time-integrated neutrino flux is unknown in Ref. [149], so we assume perfect equipartition for the scenario D (i.e., $L_{\nu_e} = L_{\bar{\nu}_e} = L_{\nu_x} = 5 \times 10^{52}$ ergs).

Finally, in Fig.2.2 we show the expected CCSN neutrino flux spectra as a function of the true neutrino energy for the scenarios established in Table 2.3: A (upper left panel), B (upper middle panel), C₁ (upper right panel), C₂ (lower left panel), C₃ (lower middle panel) and D (lower right panel). The dark (ν_e), red ($\bar{\nu}_e$) and green (ν_x) curves show the un-oscillated neutrino fluences from a CCSN located at 10 kpc from the Earth.

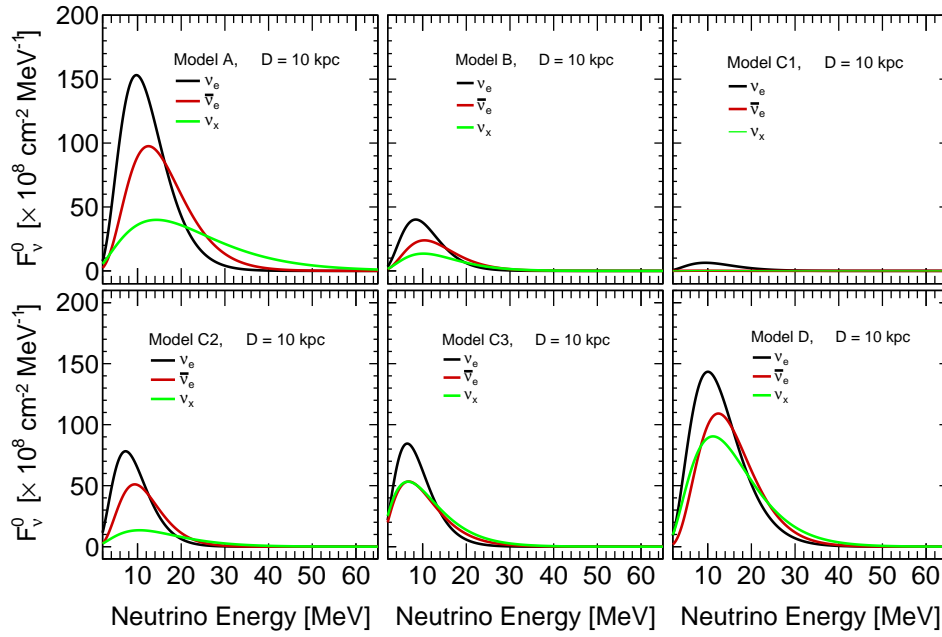


Figure 2.2: Expected CCSN neutrino energy spectra associated with the scenarios listed in Table 2.3. Here, the dark (ν_e), red ($\bar{\nu}_e$) and green (ν_x) curves show the un-oscillated neutrino fluences from a CCSN located at 10 kpc from us.

3

Neutrino Oscillations

To date we know that neutrinos exist in at least three flavor states, electron neutrino, muon neutrino and tau neutrino. On their way from the source to the detector, neutrinos can oscillate in flavor due to quantum interference effects between the eigenstates of the Hamiltonian, different from the flavor eigenstates, ν_e , ν_μ and ν_τ . By neutrino oscillation we understand the mechanism by which a neutrino of a certain flavor is transformed into another neutrino flavor different from the initial state. Consequently, the probability that a neutrino will preserve the same flavor at a later time is different from one. In this section we will deal in more details with the relationship between mass and flavor eigenstates. In section 3.1, we comment on the solar neutrino problem and the atmospheric neutrino anomaly. In the following sessions, based on Ref. [156] we address the phenomenon of neutrino oscillations both in the vacuum, in section 3.2, and in matter, in section 3.3.

3.1

Solar and atmospheric neutrino problem

From an experimental point of view, the mechanism of neutrino oscillations as we know it today arises as a solution to the unexpected result of the Homestake experiment led by Raymond Davis in the mid-1960's. The objective of this experiment was to detect solar neutrinos¹ using the reaction $\nu_e + {}^{37}\text{Cl} \rightarrow e^- + {}^{37}\text{Ar}$. The first results from 1968 showed the existence of a deficit in the number of observed neutrinos. The experiment ended in 1995 and lead to the following result for the mean number of measured events² [157]:

$$\Phi_{\text{Homestake}} = 2.56 \pm 0.16(\text{stat}) \pm 0.16(\text{syst}) \text{ SNU}, \quad (3-1)$$

¹The threshold energy of $\nu_e + {}^{37}\text{Cl} \rightarrow e^- + {}^{37}\text{Ar}$ reaction is 0.814 MeV. Hence, more than 91% of the solar neutrinos coming from the Sun are transparent to this reaction, only the ${}^7\text{Be}$, ${}^8\text{B}$ and hep solar neutrino flux are sensitive to it, but the hep contribution is so small and then neglected.

²A Solar Neutrino Unit (SNU) is the product of the calculated or measured solar neutrino fluxes and the calculated cross sections. Therefore $1 \text{ SNU} = 10^{-36} \text{ captures/atom/sec}$.

only a third of the expected number, $7.6_{-1.1}^{+1.3}$ SNU which was calculated by John Bahcall. This result came to be known as the solar neutrino problem and raised three possible explanations: 1) the experiment was not working well, 2) the standard solar model (SSM) was incorrect or 3) the standard model of weak interactions was not complete. The first was rapidly discarded with the confirmation of this problem by SAGE [158], GALLEX [159], Kamiokande and Super-Kamiokande neutrino experiments. After the 1968 article [157] in which the problem of solar neutrinos was first established, Bahcall and his collaborators estimated analytically and numerically the possible uncertainties in the fluxes of solar neutrinos and obtained the following conclusion [161, 162]: "Standard solar models predict the structure of the Sun more accurately than is required for applications involving solar neutrinos". In this way, the possibility of new physics beyond the standard model of elementary particles was left open [163]. In the early 2000s, the SNO experiment [2] established the transformation of ν_e into ν_μ and ν_τ by comparing the electron neutrino flux to the total flux of all neutrino flavors. Finally, the solar neutrino problem was definitively resolved by KamLAND [5] which selected a unique solution (large mixing angle adiabatic conversion) to this problem and showed that neutrino mass was behind the SNO result.

At the time, the IMB-1 (Irvine-Michigan-Brookhaven) experiment, whose main goal was to discover proton decay, measured fewer muon decay events than expected from atmospheric neutrinos (background for the proton decay search) [160]. This so-called atmospheric neutrino anomaly soon was confirmed by Kamiokande, they found that the number of μ -like events had a significant deficit compared with the Monte Carlo prediction, while the number of e -like events was in agreement with the prediction within the statistical and systematic errors. In 1998, SuperKamiokande [3] provided overwhelming evidence that explained the IMB and Kamiokande anomaly in terms of neutrino oscillations: $\nu_\mu \leftrightarrow \nu_\tau$.

3.2

Neutrino oscillations in vacuum

To date, many experiments have confirmed the existence of neutrino oscillations among all neutrino flavors and thus have helped to build the three-flavor neutrino oscillation scenario. As we commented before, neutrino oscillations are consequences of mixing, that is, of the fact that the flavor eigenstates ν_α ($\alpha = e, \mu, \tau$) do not coincide with the mass eigenstates ν_i ($i = 1, 2, 3$). Flavor eigenstates are linear superpositions of three neutrino mass

eigenstates and at least two of them have nonzero masses, that is

$$|\nu_\alpha\rangle = \sum_i U_{\alpha i}^* |\nu_i\rangle, \quad (3-2)$$

where the mass and flavor eigenstates follow the normalization condition $\langle \nu_j | \nu_k \rangle = \delta_{jk}$ and $\langle \nu_\alpha | \nu_\beta \rangle = \delta_{\alpha\beta}$ respectively. Inversely, the mass eigenstates are linear superpositions of the flavor eigenstates,

$$|\nu_i\rangle = \sum_\alpha U_{\alpha i} |\nu_\alpha\rangle. \quad (3-3)$$

Here and after, Latin indices (e.g., i, j, k) will denote indices belonging to the mass eigenstate basis and Greek indices (e.g., α, β, γ) will denote indices belonging to the flavor basis.

In Eqs. (3-2) and (3-3), $U_{\alpha i}$ are the elements of the Pontecorvo-Maki-Nakagawa-Sakata (PMNS) lepton mixing matrix defined as:

$$U = \begin{pmatrix} U_{e1} & U_{e2} & U_{e3} \\ U_{\mu 1} & U_{\mu 2} & U_{\mu 3} \\ U_{\tau 1} & U_{\tau 2} & U_{\tau 3} \end{pmatrix}, \quad (3-4)$$

which is an unitary matrix, this means

$$\sum_j U_{\alpha j}^* U_{\beta j} = \delta_{\alpha\beta} \quad \text{and} \quad \sum_\alpha U_{\alpha j}^* U_{\alpha k} = \delta_{jk}. \quad (3-5)$$

The most common parametrization of U is given by the Particle Data Group which uses three mixing angles θ_{12} , θ_{13} and θ_{23} , a CP-violating phase δ . Therefore,

$$U = \begin{pmatrix} c_{12} c_{13} & s_{12} c_{13} & s_{13} e^{-i\delta} \\ -s_{12} c_{23} - c_{12} s_{13} s_{23} e^{i\delta} & c_{12} c_{23} - s_{12} s_{13} s_{23} e^{i\delta} & c_{13} s_{23} \\ s_{12} s_{23} - s_{12} s_{13} c_{23} e^{i\delta} & c_{12} s_{23} - s_{12} s_{13} c_{23} e^{i\delta} & c_{13} c_{23} \end{pmatrix}, \quad (3-6)$$

where $c_{ij} \equiv \cos \theta_{ij}$ and $s_{ij} \equiv \sin \theta_{ij}$.

Neutrinos in vacuum can be modeled as free particles, and hence they are stationary states of the free Hamiltonian \mathcal{H}_0 ,

$$\mathcal{H}_0 |\nu_i\rangle = E_i |\nu_i\rangle, \quad (3-7)$$

where E_i is the energy eigenvalue corresponding to the eigenstate $|\nu_i\rangle$ of the free Hamiltonian. Since the neutrino is an ultra-relativistic particle (i.e., the neutrino momentum is much greater than its mass.), we can compute an approximation of E_i by using the first two terms of the Taylor series expansion

of the total energy of the particle, the assumption that all neutrinos have the same momentum³, $|\vec{p}_i| = |\vec{p}|$, and neglecting the mass contribution to the neutrino energy, i.e., $|\vec{p}| = E$. That is

$$E_i = \sqrt{|\vec{p}|^2 + m_i^2} \approx E + \frac{m_i^2}{2E}, \quad (3-8)$$

where E is the neutrino energy and $m_i (i = 1, 2, 3)$ are the masses of the mass eigenstates. Under Eqs. (3-2) and (3-3) there are two bases in terms of which we can express our results: the flavor $\{\nu_e, \nu_\mu, \nu_\tau\}$ and the mass $\{\nu_1, \nu_2, \nu_3\}$ bases. In the mass basis, the vacuum Hamiltonian takes the form:

$$\mathcal{H}_0 = \begin{pmatrix} E + \frac{m_1^2}{2E} & 0 & 0 \\ 0 & E + \frac{m_2^2}{2E} & 0 \\ 0 & 0 & E + \frac{m_3^2}{2E} \end{pmatrix}. \quad (3-9)$$

We can flip between the bases at our convenience, hence in the flavor basis the time evolution of the favor eigenstates $|\nu_\alpha\rangle$ is given by the Schrödinger-like equation:

$$i \frac{d}{dt} |\nu_\alpha, t\rangle = \mathcal{H}_0 |\nu_\alpha, t\rangle, \quad (3-10)$$

whose solution is

$$|\nu_\alpha, t\rangle = e^{-i\mathcal{H}_0 t} |\nu_\alpha\rangle \quad \text{with} \quad |\nu_\alpha\rangle = |\nu_\alpha, t = 0\rangle. \quad (3-11)$$

In order that the operator $e^{-i\mathcal{H}_0 t}$ can act on the state $|\nu_\alpha\rangle$ it is necessary to write it in the mass basis, therefore we have:

$$\begin{aligned} |\nu_\alpha, t\rangle &= \sum_k e^{-i\mathcal{H}_0 t} U_{\alpha k}^* |\nu_k\rangle, \\ &= \sum_k e^{-iE_k t} U_{\alpha k}^* |\nu_k\rangle, \\ &= \sum_k e^{-iE_k t} U_{\alpha k}^* \left(\sum_\beta U_{\beta k} |\nu_\beta\rangle \right), \\ &= \sum_{\beta=e,\mu,\tau} \left(\sum_k U_{\alpha k}^* e^{-iE_k t} U_{\beta k} \right) |\nu_\beta\rangle. \end{aligned} \quad (3-12)$$

Therefore, a pure flavor state $|\nu_\alpha\rangle$ at $t = 0$ becomes a linear superposition of different flavor states at $t > 0$. The probability of transition from a flavor neutrino ν_α to a flavor neutrino ν_β is given by

³It is necessary to emphasize that the common assumptions of "same energy" and "same momentum" for neutrino mass eigenstates are both wrong, but they lead to the correct oscillation probability formula [164].

$$\begin{aligned}
P(\nu_\alpha \rightarrow \nu_\beta) &= |\langle \nu_\beta | \nu_\alpha, t \rangle|^2, \\
&= \sum_{j,k} U_{\alpha k}^* U_{\beta k} U_{\alpha j} U_{\beta j}^* e^{-i(E_k - E_j)t}, \\
&= \sum_{j,k} U_{\alpha k}^* U_{\beta k} U_{\alpha j} U_{\beta j}^* \exp\left(-i \frac{\Delta m_{kj}^2 L}{2E}\right),
\end{aligned} \tag{3-13}$$

where $\Delta m_{kj}^2 \equiv m_k^2 - m_j^2$ is the mass squared differences of neutrinos and $L \sim t$ the source-detector distance. This probability depends on the quartic products $U_{\alpha k}^* U_{\beta k} U_{\alpha j} U_{\beta j}^*$ which do not depend on the phases that can be factorized from the mixing matrix, global phases. In general Eq. (3-6) contains two additional phases, the Majorana ones. Since the Majorana phases can be factorized from the mixing matrix, the transition probability Eq. (3-13) is not influenced by them. Neutrino oscillation experiments cannot give insights on whether neutrino is a Dirac or Majorana particle.

A useful way to rewrite Eq. (3-13) is in terms of the real and imaginary parts of the quartic products. For this, we introduce the following notation: $M_{\alpha\beta}^{kj} = U_{\alpha k}^* U_{\beta k} U_{\alpha j} U_{\beta j}^*$ and $\Phi_{kj} = \Delta m_{kj}^2 L/2E$. Now we split the summation and keep in mind that $\Re e(z) = (z + z^*)/2$, that is:

$$\begin{aligned}
\sum_{k,j} M_{\alpha\beta}^{kj} e^{-i\Phi_{kj}} &= \sum_{k=j} M_{\alpha\beta}^{kj} + \sum_{k>j} M_{\alpha\beta}^{kj} e^{-i\Phi_{kj}} + \sum_{k<j} M_{\alpha\beta}^{kj} e^{-i\Phi_{kj}}, \\
&= \sum_k |U_{\alpha k}|^2 |U_{\beta k}|^2 + \sum_{k>j} \left(M_{\alpha\beta}^{kj} e^{-i\Phi_{kj}} + M_{\alpha\beta}^{kj*} e^{i\Phi_{kj}} \right), \\
&= \sum_k |U_{\alpha k}|^2 |U_{\beta k}|^2 + 2 \sum_{k>j} \Re e \left(M_{\alpha\beta}^{kj} e^{-i\Phi_{kj}} \right).
\end{aligned} \tag{3-14}$$

On the other hand, from Eq. (3-5) we have that

$$\begin{aligned}
\sum_{k,j} M_{\alpha\beta}^{kj} &= \sum_k U_{\alpha k}^* U_{\beta k} \sum_j U_{\alpha j} U_{\beta j}^* = (\delta_{\alpha\beta})^2 = \delta_{\alpha\beta}, \\
\delta_{\alpha\beta} &= \sum_k |U_{\alpha k}|^2 |U_{\beta k}|^2 + 2 \sum_{k>j} \Re e \left[M_{\alpha\beta}^{kj} \right],
\end{aligned} \tag{3-15}$$

therefore, we can use Eqs. (3-14) and (3-15) to rewrite Eq. (3-13):

$$\begin{aligned}
P(\nu_\alpha \rightarrow \nu_\beta) &= \delta_{\alpha\beta} - \sum_{k>j} \left(M_{\alpha\beta}^{kj} + M_{\alpha\beta}^{kj*} \right) + \sum_{k>j} \left(M_{\alpha\beta}^{kj} e^{-i\Phi_{kj}} + M_{\alpha\beta}^{kj*} e^{i\Phi_{kj}} \right), \\
&= \delta_{\alpha\beta} - \sum_{k>j} \left(M_{\alpha\beta}^{kj} + M_{\alpha\beta}^{kj*} \right) + \frac{1}{2} \sum_{k>j} \left[\left(M_{\alpha\beta}^{kj} + M_{\alpha\beta}^{kj*} \right) \left(e^{-i\Phi_{kj}} + e^{i\Phi_{kj}} \right) \right] \\
&\quad + \frac{1}{2} \sum_{k>j} \left[\left(M_{\alpha\beta}^{kj} - M_{\alpha\beta}^{kj*} \right) \left(e^{-i\Phi_{kj}} - e^{i\Phi_{kj}} \right) \right], \\
&= \delta_{\alpha\beta} - \frac{1}{2} \sum_{k>j} \left[\left(M_{\alpha\beta}^{kj} - M_{\alpha\beta}^{kj*} \right) \left(e^{i\Phi_{kj}} - e^{-i\Phi_{kj}} \right) \right] - 2 \sum_{k>j} \Re e \left[M_{\alpha\beta}^{kj} \right] \\
&\quad + 2 \sum_{k>j} \Re e \left[M_{\alpha\beta}^{kj} \right] \cos \Phi_{kj},
\end{aligned}$$

$$\begin{aligned}
&= \delta_{\alpha\beta} - 2 \sum_{k>j} \Re e[M_{\alpha\beta}^{kj}] (1 - \cos \Phi_{kj}) + 2 \sum_{k>j} \Im m[M_{\alpha\beta}^{kj}] \sin \Phi_{kj}, \\
&= \delta_{\alpha\beta} - 4 \sum_{k>j} \Re e[M_{\alpha\beta}^{kj}] \sin^2 \left(\frac{\Phi_{kj}}{2} \right) + 2 \sum_{k>j} \Im m[M_{\alpha\beta}^{kj}] \sin \Phi_{kj}.
\end{aligned} \tag{3-16}$$

Since the sum of all probabilities must be equal to unity, the survival probability ($\alpha = \beta$) can be written as

$$P(\nu_\alpha \rightarrow \nu_\alpha) = 1 - 4 \sum_{k>j} |U_{\alpha k}|^2 |U_{\alpha j}|^2 \sin^2 \left(\frac{\Delta m_{kj}^2 L}{4E} \right), \tag{3-17}$$

where we have used $\Im m[M_{\alpha\beta}^{kj}] = 0$. In the case of two-neutrino mixing, this probability takes a more simplified form:

$$P(\nu_\alpha \rightarrow \nu_\alpha)(L, E) = 1 - \sin^2 2\theta \sin^2 \left(\frac{\Delta m^2 L}{4E} \right), \tag{3-18}$$

where θ is the mixing angle, which defines how different are the flavor states from the mass states. If $\theta = 0$, the flavor states are identical to the mass states.

Maybe the main characteristic that we see from Eq. (3-18) is the periodic dependence on the L/E parameter. Flavor oscillations depend on the spacial scale, with

$$L_{osc} = \frac{4\pi E}{\Delta m^2}, \tag{3-19}$$

corresponding to the oscillation length, which is defined as the location of the first dip of the transition probability, i.e. $1 - P(\nu_\alpha \rightarrow \nu_\alpha)$.

3.3

Neutrino oscillations in matter

Neutrinos propagating in matter can interact via coherent forward elastic scattering with electrons and nucleons in the medium. This reaction is the main mechanism behind matter effects on neutrino oscillations⁴. The effect of these interactions is described by an effective potential that depends on the composition and density of matter, this potential modifies the neutrino mixing [165]. Since ordinary matter is rich in electrons and the muon content is exactly zero, only the electron neutrinos present coherent forward elastic weak charged-current scatterings. On the other hand, all flavors (including the electron type) experience neutral interactions. The effective matter potential

⁴In matter, neutrinos can also exhibit incoherent scatterings with the particles in the medium, however these interactions can be neglected because their cross sections are too small, typically, $\sigma \sim 10^{-43} \text{ cm}^2 \left(\frac{E}{\text{MeV}} \right)^2$.

is defined as

$$V_\alpha = \overbrace{\sqrt{2} G_F N_e \delta_{\alpha e}}^{\text{charged-current potential } (V_{CC})} \quad (3-20a)$$

$$+ \underbrace{\frac{\sqrt{2}}{2} G_F \left[-N_e(1 - 4 \sin^2 \theta_w) + N_p(1 - 4 \sin^2 \theta_w) - N_n \right]}_{\text{neutral-current potential } (V_{NC})}, \quad (3-20b)$$

where N_e , N_p and N_n are the electron, proton and neutron number densities, respectively. G_F is the Fermi constant, and θ_w is the weak mixing angle (or Weinberg angle). In neutral matter $N_e = N_p$ so the contributions from electrons and protons cancel each other. In the case of anti-neutrinos we must substitute $V_\alpha \rightarrow -V_\alpha$.

In order to understand the matter effects on the neutrino oscillations, let us consider a neutrino in the state $|\nu_\alpha\rangle = |\nu_\alpha, t=0\rangle$ which obeys the evolution equation

$$i \frac{d}{dt} |\nu_\alpha, t\rangle = \mathcal{H} |\nu_\alpha, t\rangle, \quad (3-21)$$

where

$$\mathcal{H} = \mathcal{H}_0 + \mathcal{H}_I \quad \text{with} \quad \mathcal{H}_I |\nu_\alpha\rangle = V_\alpha |\nu_\alpha\rangle. \quad (3-22)$$

Now, if we define the amplitude of $\nu_\alpha \rightarrow \nu_\beta$ transition after a time t as

$$A_{\alpha\beta}(t) = \langle \nu_\beta | \nu_\alpha, t \rangle \quad \text{with} \quad A_{\alpha\beta}(t=0) = \delta_{\alpha\beta}, \quad (3-23)$$

and also taking into account that neutrinos are ultra-relativistic particles that result in Eq. (3-8), we can use Eqs. (3-2), (3-20) and (3-22) into Eq. (3-21) to write the time evolution equation for the flavor transition amplitude as:

$$i \frac{d}{dt} A_{\alpha\beta}(t) = \left(E + \frac{m_1^2}{2E} + V_{NC} \right) A_{\alpha\beta}(t), \quad (3-24)$$

$$+ \sum_\gamma \left(\sum_k U_{\beta k} \frac{\Delta m_{k1}^2}{2E} U_{\gamma k}^* + \delta_{\beta e} \delta_{\gamma e} V_{CC} \right) A_{\alpha\gamma}(t).$$

The first term in Eq (3-24) generates a phase common to all flavors, and can be eliminated by the rephasing:

$$A_{\alpha\beta}(t) \longrightarrow A_{\alpha\beta}(t) \exp \left[-i \left(E + \frac{m_1^2}{2E} \right) t - i \int_0^t V_{NC}(t') dt' \right]. \quad (3-25)$$

With this phase shift and rewriting Eq. (3-24) in terms of $x \approx t$, we finally obtain the time evolution equation for the flavor transition amplitude,

$$i \frac{d}{dx} A_{\alpha\beta}(x) = \sum_\gamma \left(\sum_k U_{\beta k} \frac{\Delta m_{k1}^2}{2E} U_{\gamma k}^* + \delta_{\beta e} \delta_{\gamma e} V_{CC} \right) A_{\alpha\gamma}(x). \quad (3-26)$$

The above equation has the structure of a Schrödinger-like equation with an effective Hamiltonian

$$\mathcal{H}_{eff}^{(f)}(x) = \frac{1}{2E} \left[U \begin{pmatrix} 0 & & \\ & \Delta m_{21}^2 & \\ & & \Delta m_{31}^2 \end{pmatrix} U^\dagger + \begin{pmatrix} a(x) & & \\ & 0 & \\ & & 0 \end{pmatrix} \right], \quad (3-27)$$

where E is the neutrino energy, $\Delta m_{ij}^2 \equiv m_i^2 - m_j^2$ are the neutrino mass squared differences with $m_i (i = 1, 2, 3)$ being the neutrino masses, U is the standard mixing matrix which allows to describe the flavor eigenstates $\nu_\alpha (\alpha = e, \mu, \tau)$ as mixtures of the mass eigenstates $\nu_i (i = 1, 2, 3)$ as in the Eq. (3-2) and the superscript (f) refers to the flavor basis. The term $a(x)$ in Eq. (3-27) takes into account the charged current interactions between electron (anti-) neutrinos and electrons of the medium:

$$a(x) = 2E V_{CC}(x) \approx 7.56 \times 10^{-8} \text{ eV}^2 \left(\frac{\rho(x)}{\text{g/cm}^3} \right) \left(\frac{E}{\text{MeV}} \right), \quad (3-28)$$

where $\rho(x)$ is the density in the medium at the position x .

3.3.1

MSW effect in the star

For simplicity let us analyze the Eq. (3-27) for the two-flavor neutrino oscillation scenario $\{\nu_e, \nu_{\mu'}\}$, with $\alpha = e$ as initial condition. Here, $\nu_{\mu'}$ must be understood as a linear combination of ν_μ and ν_τ . Under these assumptions the effective Hamiltonian in the flavor basis can be written as

$$\mathcal{H}_{eff}^{(f)} = \frac{1}{4E} \begin{pmatrix} -\Delta m^2 \cos 2\theta + a(x) & \Delta m^2 \sin 2\theta \\ \Delta m^2 \sin 2\theta & \Delta m^2 \cos 2\theta - a(x) \end{pmatrix}, \quad (3-29)$$

where $\Delta m^2 = m_2^2 - m_1^2$ and θ is the angle that define the vacuum mixing:

$$\nu_e = \cos \theta \nu_1 + \sin \theta \nu_2, \quad \nu_{\mu'} = -\sin \theta \nu_1 + \cos \theta \nu_2. \quad (3-30)$$

Since $\mathcal{H}_{eff}^{(f)}$ is Hermitian and, even more, real and symmetric, we can diagonalize it by the orthogonal transformation $U_M^T \mathcal{H}_{eff}^{(f)} U_M = \check{\mathcal{H}}_{eff}^{(m)}$, where $\check{\mathcal{H}}_{eff}^{(m)}$ is the effective Hamiltonian in the mass basis in matter and

$$U_M = \begin{pmatrix} \cos \theta_M & \sin \theta_M \\ -\sin \theta_M & \cos \theta_M \end{pmatrix} \quad (3-31)$$

is the effective mixing matrix in matter with θ_M denoting the effective mixing

angle in matter, and hence

$$\sin 2\theta_M = \frac{\sin 2\theta}{\sqrt{\sin^2 2\theta + \left(\cos 2\theta - \frac{a(x)}{\Delta m^2}\right)^2}}. \quad (3-32)$$

$\Delta m_M^2(x)$ is the effective mass-squared difference in matter and is given by

$$\Delta m_M^2(x) = \sqrt{(\Delta m^2 \cos 2\theta - a(x))^2 + (\Delta m^2 \sin 2\theta)^2}. \quad (3-33)$$

We can observe from these equations that there is a resonance when $a(x) \approx \Delta m^2 \cos 2\theta$, i.e., for $\theta_M \sim 45^\circ$. The oscillations can be significantly enhanced, leading to the possibility of total transitions between the two flavors if the resonance region is wide enough. If $a(x) \ll \Delta m^2$ matter and vacuum mixing angles are almost equal, $\theta_M \approx \theta$. While if $a(x) \gg \Delta m^2$ the oscillation effect is strongly suppressed because $\theta_M \approx \pi/2$. This happens in regions where the matter density is very high, much higher than in the center of the Sun or Earth. This mechanism is the essence of the Mikheyev-Smirnov-Wolfenstein effect (MSW effect) [165, 166].

Massive stars in gravitational collapse present two regions where neutrinos, during their propagation out of the star, can undergo resonant flavor conversions [55], these regions are known as resonance layers and are located in the outer layers of the mantle, where the matter density is given by

$$\rho_{res} \approx 1.4 \times 10^6 \left(\frac{\Delta m^2}{1 \text{ eV}^2}\right) \left(\frac{10 \text{ MeV}}{E}\right) \left(\frac{0.5}{Y_e}\right) \cos 2\theta \text{ g cm}^{-3}, \quad (3-34)$$

Here Y_e is the number of electrons per nucleon in the medium and θ the mixing angle associated with the mass-squared difference Δm^2 , which can be either Δm_{31}^2 or Δm_{21}^2 , depending on whether the density in that region is higher (H) or lower (L). The resonance layer associated with the solar mass splitting is referred as the low resonance layer, while that associated with the atmospheric mass splitting is the high resonance layer.

Due to the fact that $\Delta m_{31}^2 \gg \Delta m_{21}^2$, the flavor conversions in both the high- and low-resonance layers are considered as independent of each other and each conversion is approximately reduced to a two-flavor neutrino oscillation problem [55], just like the one that we have been considering, i.e., Eqs. (3-29), (3-31), (3-32) and (3-33).

In order to extract more information that allows us to understand the MSW effect, Eq. (3-26) can be written in the matrix form and adapted to the

two-flavor scenario, then by means of the transformation $\Psi_e = U_M \Phi_e$, where

$$\Psi_e(x) = \begin{pmatrix} A_{ee}(x) \\ A_{e\mu'}(x) \end{pmatrix} \quad \text{and} \quad \Phi_e(x) = \begin{pmatrix} \phi_{e1}(x) \\ \phi_{e2}(x) \end{pmatrix}, \quad (3-35)$$

with $\phi_{e1}(x)$ and $\phi_{e2}(x)$ being the transition amplitudes of ν_1 and ν_2 to ν_e , respectively. So we can write in the mass basis in matter the Schrödinger-like equation for the evolution of the amplitudes of the effective neutrinos in matter, that is:

$$i \frac{d}{dx} \Phi_e = \frac{1}{4E} \begin{pmatrix} -\Delta m_M^2 & -4iE \frac{d\theta_M}{dx} \\ 4iE \frac{d\theta_M}{dx} & \Delta m_M^2 \end{pmatrix} \Phi_e. \quad (3-36)$$

From the last equation we can see that when $d\theta_M/dx = 0$, the amplitudes can evolve in a decoupled way. This occurs in environments where the density of matter is constant, e.g., in the Earth's mantle (roughly speaking), and leads to enhance the oscillation probability. Such probability is similar in form to that obtained in vacuum for the two-neutrino mixing scenario and it is given by

$$P(\nu_e \rightarrow \nu_{\mu'}) = \sin^2 2\theta_M \sin^2 \left(\frac{\Delta m_M^2 x}{4E} \right). \quad (3-37)$$

On the other hand, when neutrinos propagate in a medium with varying density, i.e., $\frac{d\theta_M}{dx} \neq 0$, the hamiltonian changes in the course of propagation, which implies the eigenstates of the instantaneous Hamiltonian are no more eigenstates of the propagation, and transitions between the effective mass eigenstates in matter can occur. If the matter density changes slowly, the system has time to adjust the change and the evolution is adiabatic, i.e, there is no transitions between the mass eigenstates in matter. A way to quantify the adiabaticity of the transition is to define a adiabaticity parameter at the resonance (see Refs. [167, 55] and references therein)

$$\gamma \equiv \left| \frac{\Delta m_M^2 / 4E}{d\theta_M / dx} \right|_{res} = \frac{\Delta m^2 \sin^2 \theta}{2E \cos 2\theta \left| \frac{d}{dx} \ln a(x) \right|_{res}}, \quad (3-38a)$$

$$= \left(\frac{\Delta m^2}{E} \right)^{2/3} \left(\frac{\sin^2 2\theta}{6(\cos 2\theta)^{4/3}} \right) \left(\frac{2\sqrt{2}G_F Y_e A}{m_N} \right)^{1/3}, \quad (3-38b)$$

where m_N is the mass of the nucleons and $\gamma \gg 1$ corresponds to the adiabatic case and $\gamma \ll 1$ corresponds to the non-adiabatic one. Here we have considered a matter density profile in the star of the form $\rho = A/r^3$, with A the proportionality constant. Then we can obtain the probability for the transition between the mass eigenstates in matter (or more abbreviated:

crossing probability) by using the Landau-Zener formula

$$P_\xi = \exp\left(-\frac{\pi}{2}\gamma\right) = \exp\left[-\left(\frac{E^*}{E}\right)^{2/3}\right], \quad (3-39)$$

where

$$E^* \equiv \left(\frac{\pi}{12}\right)^{2/3} \left(\frac{\Delta m^2 \sin^3 2\theta}{\cos^2 2\theta}\right) \left(\frac{2\sqrt{2}G_F Y_e A}{m_N}\right)^{1/2}. \quad (3-40)$$

The Landau-Zener formula is only valid for a linear variation of density in the resonance layers and a small mixing angle [156]. However, we use this formula with a density profile $\rho = A/r^3$ because our objective is only to visualize the most relevant features of the transitions between states in matter. From Eq. (3-40), clearly we can see that the probability of neutrino transitions in matter depends on the mixing angle and the mass squared difference. Indeed, the crossing probability in the high resonance layer ($\xi = H$) is governed by θ_{13} and Δm_{31}^2 , while in the low resonance layer this probability ($\xi = L$) depends on θ_{12} and Δm_{21}^2 . Figure 3.1 shows the energy dependence of the crossing probability, P_ξ increase with the energy.

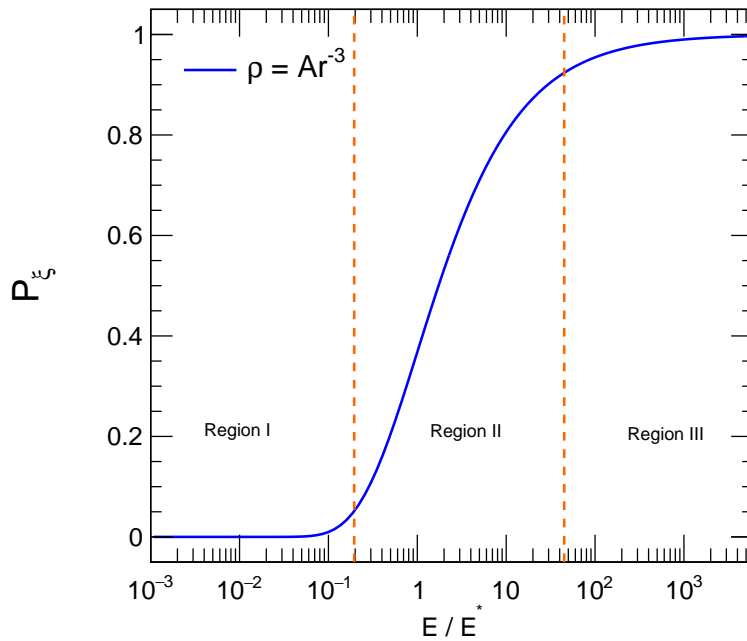


Figure 3.1: Energy dependence of P_ξ for a density profile $\rho = A/r^3$. The dashed lines divide the whole range of E/E^* in three parts: non adiabatic region (I), intermediate region (II) and adiabatic region (III) .

We can distinguish three regions:

1. *Adiabatic region (region I)*: P_ξ is equal to 0 for any value of the neutrino energy. Therefore, there is no transitions between the mass eigenstates in the resonance layer.

2. *Intermediate region (region II)*: in this region the value of P_ξ increase with the neutrino energy. For relatively low energies, the system may exhibit partially adiabatic transitions.
3. *Non adiabatic region (region III)*: the crossing probability is almost equal to 1, independently of the neutrino energy.

Going back to Eq. (3-36). This equation has an effective Hamiltonian in matter given by

$$\check{\mathcal{H}}_{eff}^{(m)} = \frac{1}{4E} \begin{pmatrix} -\Delta m_M^2 & -4iE \frac{d\theta_M}{dx} \\ 4iE \frac{d\theta_M}{dx} & \Delta m_M^2 \end{pmatrix}, \quad (3-41)$$

whose eigenvalues are

$$\lambda_{1,2} = \pm \sqrt{(\Delta m_M^2)^2 + 16E^2 \left(\frac{d\theta_M}{dx} \right)^2}. \quad (3-42)$$

For $\check{\mathcal{H}}_{eff}^{(m)}$ to be diagonal, its eigenvalues must be equal to $\pm \Delta m_M^2$. In fact, this happens if $\frac{d\theta_M}{dx} \neq 0$ (trivial case, which has already been analyzed) or when

$$\left| \frac{d\theta_M}{dx} \right| \ll \left| \frac{\Delta m_M^2}{4E} \right|, \quad (3-43)$$

or equivalently, $\gamma \gg 1$ for all points of the neutrino trajectory. In this adiabatic scenario, the time evolution of each amplitude in Eq. (3-36) is independent of the other. That is:

$$i \frac{d}{dx} \Phi_e^{ad} \sim \frac{1}{4E} \begin{pmatrix} -\Delta m_M^2 & 0 \\ 0 & \Delta m_M^2 \end{pmatrix} \Phi_e^{ad}. \quad (3-44)$$

The solution of this equation simply leads to the following results:

$$\phi_{e1}(x) = \cos \theta_M(x=0) \exp \left(i \int_0^x \frac{\Delta m_M^2(x')}{4E} dx' \right), \quad (3-45a)$$

$$\phi_{e2}(x) = \sin \theta_M(x=0) \exp \left(-i \int_0^x \frac{\Delta m_M^2(x')}{4E} dx' \right). \quad (3-45b)$$

As a consequence an electron neutrino (i.e., ν_2 since $\theta_M \sim \pi/2$), produced deep within the core where $a(x) \gg \Delta m^2$, will emerge from the star like a muon neutrino (i.e., $\sim \nu_1$) with a transition probability given by

$$\begin{aligned}
P^{ad}(\nu_e \rightarrow \nu_\mu) &= \left| A_{e\mu} \right|^2, \\
&= \left| -\sin \theta_M(x) \phi_{e1} + \cos \theta_M(x) \phi_{e2} \right|^2, \\
&= \frac{1}{2} - \frac{1}{2} \cos 2\theta_M(x=0) \cos 2\theta_M(x) - \\
&\quad \frac{1}{2} \sin 2\theta_M(x=0) \sin 2\theta_M(x) \cos \left(\int_0^x \frac{\Delta m_M^2(x')}{2E} dx' \right).
\end{aligned} \tag{3-46}$$

3.3.1.1

High and low resonances

So far we have obtained important information using only the two-flavor neutrino scenario. However, there is no reason other than mathematical simplicity to limit ourselves to two-flavor mixing. Let us rewrite the Hamiltonian of Eq. (3-27) in terms of vacuum mass basis, by a redefinition of the mixing matrix $U \rightarrow U \text{diag}(1, 1, e^{i\delta})$, the Hamiltonian becomes real, that is

$$\mathcal{H}_{eff}^{(m)}(x) = \frac{a(x)}{2E} \begin{bmatrix} c_{12}^2 c_{13}^2 & c_{12} s_{12} c_{13}^2 & c_{12} c_{13} s_{13} \\ c_{12} s_{12} c_{13}^2 & \frac{\Delta m_{21}^2}{a(x)} + s_{12}^2 c_{13}^2 & s_{12} c_{13} s_{13} \\ c_{12} c_{13} s_{13} & s_{12} c_{13} s_{13} & \frac{\Delta m_{31}^2}{a(x)} + s_{13}^2 \end{bmatrix}. \tag{3-47}$$

Thus, δ and θ_{23} do not influence the propagation in matter. By diagonalizing this Hamiltonian we obtain the mass eigenvalues in matter and therefore we can visualize its dependence on the density of the medium by means of the so-called level crossing diagrams (see e.g. [55]). In Fig. 3.2 we shows the eigenvalues of the Hamiltonian in matter as a function of the electron number density for both cases of neutrino mass ordering, normal and inverted.

In the case of normal mass ordering (i.e. left panel of Fig. 3.2) electron neutrinos undergo two resonances, the high resonance (H) and the low resonance (L), when they pass through the mantle of the star; while electron anti-neutrinos reach the surface of the star without undergo any resonance effect along their propagation. In the case of inverted mass ordering (i.e. right panel of Fig. 3.2) electron neutrinos are influenced by the low resonance whereas electron anti-neutrinos are influenced by the high resonance.

As indicated in chapter 2, CCSN neutrinos are produced deep in the core of the star, where density is extremely high and hence all mixings are strongly suppressed. We find under these conditions that the flavor states coincide with

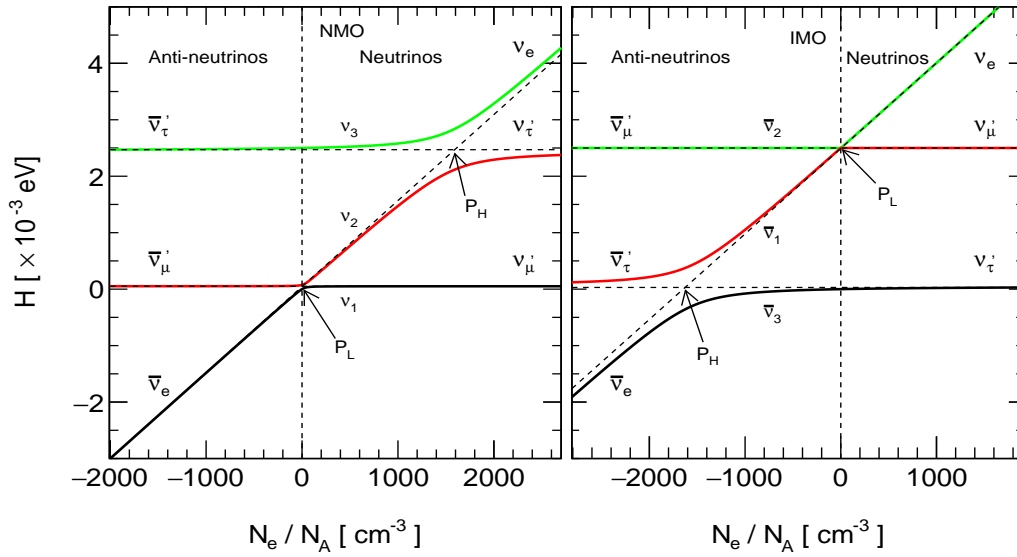


Figure 3.2: Level crossing diagrams. Solid lines correspond to eigenvalues of the effective Hamiltonian and the dashed lines to energies of flavor states. Here, we present the anti-neutrinos as neutrinos traveling through the star matter with an effective negative potential, i.e. $N_e < 0$.

the matter eigenstates and hence

$$\nu_e = \nu_{3m}, \quad \nu_{\mu'} = \nu_{1m}, \quad \nu_{\tau'} = \nu_{2m} \quad \text{for neutrinos, and} \quad (3-48a)$$

$$\bar{\nu}_e = \bar{\nu}_{1m}, \quad \bar{\nu}_{\mu'} = \bar{\nu}_{2m}, \quad \bar{\nu}_{\tau'} = \bar{\nu}_{3m} \quad \text{for anti-neutrinos,} \quad (3-48b)$$

for NMO and,

$$\nu_e = \nu_{2m}, \quad \nu_{\mu'} = \nu_{1m}, \quad \nu_{\tau'} = \nu_{3m} \quad \text{for neutrinos, and} \quad (3-49a)$$

$$\bar{\nu}_e = \bar{\nu}_{3m}, \quad \bar{\nu}_{\mu'} = \bar{\nu}_{2m}, \quad \bar{\nu}_{\tau'} = \bar{\nu}_{1m} \quad \text{for anti-neutrinos,} \quad (3-49b)$$

in the case of IMO. Here, ν_{im} ($i = 1, 2, 3$) refer to the mass eigenstates in matter and $\nu_{x'}$ ($x' = \mu', \tau'$ and their antiparticles) must be understood that they are linear combinations of the original ν_μ ($\bar{\nu}_\mu$) and ν_τ ($\bar{\nu}_\tau$) [55]. When neutrinos pass through the resonance layers on their way out of the star, they undergo adiabatic flavor conversions. To understand how these conversions work, let us stop to analyze what happens with the mass eigenstates fluxes, which we will denote as F_{ν_i} ($i = 1, 2, 3$) and $F_{\bar{\nu}_i}$ ($i = 1, 2, 3$) for the neutrino and anti-neutrino channels, respectively. Although neutrinos are created and detected as flavor states, let us recall that it is precisely ν_{im} ($\bar{\nu}_{im}$) who propagate within the star and ν_i ($\bar{\nu}_i$) in vacuum after leaving it. In these circumstances, from figure 3.2 we can write the total fluxes of neutrino mass eigenstates at the surface of the

estar as:

$$F_{\nu_1} = P_H P_L F_{\nu_e}^0 + (1 - P_H P_L) F_{\nu_x}^0, \quad (3-50a)$$

$$F_{\nu_2} = (P_H - P_H P_L) F_{\nu_e}^0 + (1 - P_H + P_H P_L) F_{\nu_x}^0, \quad (3-50b)$$

$$F_{\nu_3} = (1 - P_H) F_{\nu_e}^0 + P_H F_{\nu_x}^0, \quad (3-50c)$$

for NMO and,

$$F_{\nu_1} = P_L F_{\nu_e}^0 + (1 - P_L) F_{\nu_x}^0, \quad (3-51a)$$

$$F_{\nu_2} = (1 - P_L) F_{\nu_e}^0 + P_L F_{\nu_x}^0, \quad (3-51b)$$

$$F_{\nu_3} = P_L P_H F_{\nu_e}^0 + (1 - P_L P_H) F_{\nu_x}^0, \quad (3-51c)$$

for IMO. The wave packets associated with these neutrinos lose coherence quickly on the way to the Earth and unless neutrinos present some type of non-standard property or interaction along their way, they arrive at the surface of the Earth as incoherent mixtures of ν_1 , ν_2 and ν_3 . In the next chapter we will discuss how the invisible decay of neutrinos modifies these fluxes. For now let us continue in the standard scenario and calculate, for example, the total flux of electron neutrinos that would reach our detectors. After the neutrino mass eigenstates fluxes at the surface of the star are known, Eq.(A-1), we can calculate the fluxes for any neutrino flavor through the relationship:

$$F_{\nu_\alpha} = \sum_i |U_{\alpha i}|^2 F_{\nu_i}, \quad (3-52)$$

which in the particular case of electron neutrinos give us the following result:

$$F_{\nu_e} = p F_{\nu_e}^0 + (1 - p) F_{\nu_x}^0. \quad (3-53)$$

Here, p is the total survival probability of electron neutrinos, which is given by

$$p = |U_{e1}|^2 P_H P_L + |U_{e2}|^2 (P_H - P_H P_L) + |U_{e3}|^2 (1 - P_H), \quad (3-54)$$

in the case of NMO and,

$$p = |U_{e1}|^2 P_L + |U_{e2}|^2 (1 - P_L), \quad (3-55)$$

for IMO. Where the $|U_{e3}|^2 (P_L P_H)$ term was not included because the resonance is in the anti-neutrino channel and the mixing $|U_{e3}|$ is very small.

We know from the large mixing angle (LMA) solution to the solar neutrino problem [168] that the low resonance is adiabatic, and also due to the current value of θ_{13} [125, 169, 170] we know that the neutrino evolution

through the high resonance should be adiabatic, therefore, ignoring possible neutrino-neutrino self-interactions effects in the central region of CCSN and using the matrix elements in Eq. (3-6), we can write the total flux of ν_e and through a similar procedure that of $\bar{\nu}_e$ and ν_x . So the CCSN neutrino fluxes expected at the surface of the star are given by [55]:

$$F_{\nu_e} = s_{13}^2 F_{\nu_e}^0 + c_{13}^2 F_{\nu_x}^0, \quad (3-56a)$$

$$F_{\bar{\nu}_e} = c_{12}^2 c_{13}^2 F_{\bar{\nu}_e}^0 + (1 - c_{12}^2 c_{13}^2) F_{\nu_x}^0. \quad (3-56b)$$

$$2F_{\nu_x}(= F_{\nu_\mu} + F_{\nu_\tau}) = c_{13}^2 F_{\nu_e}^0 + (1 + s_{13}^2) F_{\nu_x}^0, \quad (3-56c)$$

$$2F_{\bar{\nu}_x}(= F_{\bar{\nu}_\mu} + F_{\bar{\nu}_\tau}) = (1 - c_{12}^2 c_{13}^2) F_{\bar{\nu}_e}^0 + (1 + c_{12}^2 c_{13}^2) F_{\bar{\nu}_x}^0, \quad (3-56d)$$

for the normal mass ordering and,

$$F_{\nu_e} = s_{12}^2 c_{13}^2 F_{\nu_e}^0 + (1 - s_{12}^2 c_{13}^2) F_{\nu_x}^0, \quad (3-57a)$$

$$F_{\bar{\nu}_e} = s_{13}^2 F_{\bar{\nu}_e}^0 + c_{13}^2 F_{\bar{\nu}_x}^0. \quad (3-57b)$$

$$2F_{\nu_x}(= F_{\nu_\mu} + F_{\nu_\tau}) = (1 - s_{12}^2 c_{13}^2) F_{\nu_e}^0 + (1 + s_{13}^2 c_{13}^2) F_{\nu_x}^0, \quad (3-57c)$$

$$2F_{\bar{\nu}_x}(= F_{\bar{\nu}_\mu} + F_{\bar{\nu}_\tau}) = c_{13}^2 F_{\bar{\nu}_e}^0 + (1 + s_{13}^2) F_{\bar{\nu}_x}^0, \quad (3-57d)$$

for the inverted mass ordering. Here, we have used the notation $c_{ij} \equiv \cos \theta_{ij}$ and $s_{ij} \equiv \sin \theta_{ij}$ and consider as implicit the energy dependence of the fluxes. Since $s_{13}^2 \simeq 0.022$, in this thesis, as a good approximation, we set $\theta_{13} = 0$ in Eqs. (3-56) and (3-57). Therefore the CCSN neutrino spectra, after neutrinos exit the star, takes the simple form:

$$F_{\nu_e} \approx F_{\nu_x}^0, \quad (3-58a)$$

$$F_{\bar{\nu}_e} \approx c_{12}^2 F_{\bar{\nu}_e}^0 + s_{12}^2 F_{\bar{\nu}_x}^0. \quad (3-58b)$$

$$2F_{\nu_x} = F_{\nu_e}^0 + F_{\nu_x}^0, \quad (3-58c)$$

$$2F_{\bar{\nu}_x} \approx s_{12}^2 F_{\bar{\nu}_e}^0 + (1 + c_{12}^2) F_{\bar{\nu}_x}^0, \quad (3-58d)$$

for the normal mass ordering, and

$$F_{\nu_e} \approx s_{12}^2 F_{\nu_e}^0 + c_{12}^2 F_{\nu_x}^0, \quad (3-59a)$$

$$F_{\bar{\nu}_e} \approx F_{\bar{\nu}_x}^0, \quad (3-59b)$$

$$2F_{\nu_x} = c_{12}^2 F_{\nu_e}^0 + (1 + s_{12}^2) F_{\nu_x}^0, \quad (3-59c)$$

$$2F_{\bar{\nu}_x} \approx F_{\bar{\nu}_e}^0 + F_{\bar{\nu}_x}^0, \quad (3-59d)$$

for the inverted mass ordering. As was already commented, in this thesis we do not consider for simplicity the possible neutrino-neutrino self interactions

effects in the core of the supernova [171, 172, 173, 174, 175, 176].

3.3.2

MSW effect in the Earth

Before reaching the detector, the CCSN neutrino fluxes can interact with the matter of the Earth as they propagate inside it towards the detector. As a consequence, the neutrinos undergo an additional flavor transformation. Such flavor transitions are governed by the MSW effect, the mechanism of which was already explained in this chapter. Since the Earth is less dense, the effect on the neutrino energy spectra will be smaller than that experienced by the neutrinos in the star. Indeed, the Earth matter potential, V , is much smaller than the kinetic energy of the neutrino system, i.e.,

$$V(x) \ll \frac{\Delta m^2}{2E}. \quad (3-60)$$

In this case, it is possible to define a small parameter

$$\epsilon(x) \equiv \frac{2EV(x)}{\Delta m^2} \approx 0.02 \left(\frac{E}{10 \text{ MeV}} \right) \left(\frac{N_e(x)}{N_A} \right) \left(\frac{7.5 \times 10^{-5} \text{ eV}^2}{\Delta m^2} \right), \quad (3-61)$$

in terms of which, we can consider an expansion of the oscillation probabilities. This is not the only difference we find, the Earth presents a more complex density profile than the one we consider inside the supernova, namely $\rho \sim 1/r^3$. The structure of the Earth is often approximated by a set of layers with constant density (mainly one or two corresponding to the mantle and the core). Figure 3.3 shows the Earth density profile according to the Preliminary reference Earth model (PREM) [177]. The presence of transitions or jumps in the Earth density will lead to non-zero crossing probabilities and hence non-adiabatic transitions between the mass eigenstates in matter, which at the same time govern the dynamics of flavor transformation, because of the connection between flavor and mass eigenstates by the mixings.

3.3.2.1

Regeneration factors

Since CCSN neutrinos arrive at the surface of the Earth as incoherent fluxes of the mass eigenstates (ν_1 , ν_2 and ν_3), in this section we are interested in determining the probability $P_{\nu_i \rightarrow \nu_e}$ ($P_{\bar{\nu}_i \rightarrow \bar{\nu}_e}$) that a mass eigenstate ν_i ($\bar{\nu}_i$) entering the Earth reaches the detector as a ν_e ($\bar{\nu}_e$). These probabilities will be very important in the following chapters and therefore in the determination of

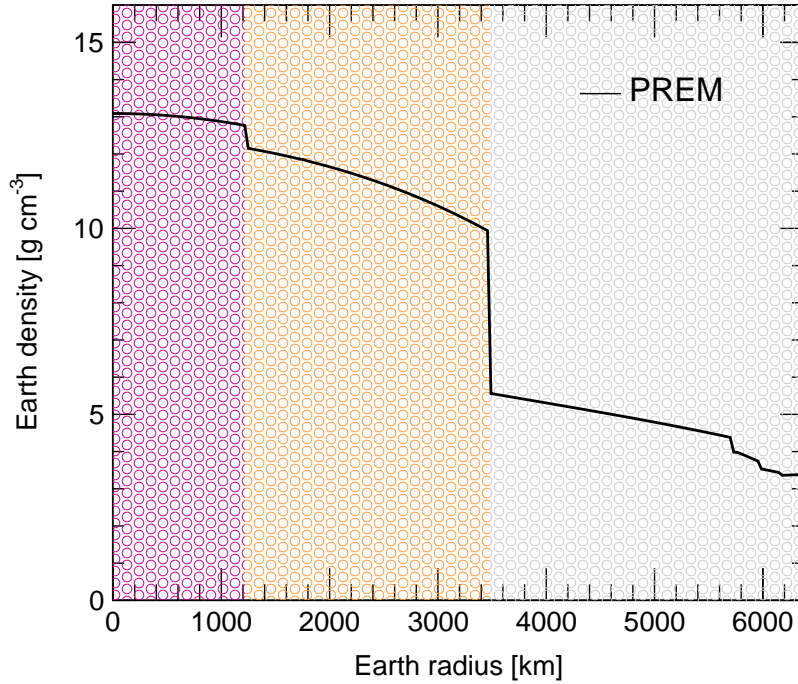


Figure 3.3: Density profile for the Earth according to the PREM model [177].

the sensitivity of next-generation neutrino detectors to the observation of Earth matter effects on supernova neutrinos in the presence of invisible neutrino decay, which is the main goal of this work. We compute these probabilities by numerically solving the evolution equation of neutrinos using the PREM model for the Earth matter density profile. This way of obtaining the probabilities is very useful for numerical computation, but it does not allow us to visualize the physics behind the problem. Therefore, with the purpose of understanding the features of these oscillation effects, let us consider the analytical approach offered by Refs. [178, 179].

The starting point is the Schrödinger-like equation

$$i \frac{d}{dx} |\nu_i, t\rangle = \mathcal{H}_{eff}^{(m)}(x) |\nu_i, t\rangle, \quad (3-62)$$

where $\mathcal{H}_{eff}^{(m)}(x)$ is the Hamiltonian in matter given by Eq. (3-47). As we have already commented, at low energies $\mathcal{O}(10 \text{ MeV})$ the parameter ϵ is small enough to find the transition probabilities through a theory of perturbations in that parameter. In order to facilitate future calculations, we rewrite the Hamiltonian in the form

$$\mathcal{H}_{eff}^{(m)}(x) = \mathcal{H}_0(x) + \mathcal{E}(x), \quad (3-63)$$

where

$$\mathcal{H}_0(x) = \begin{pmatrix} 0 & 0 & 0 \\ 0 & \Delta_s^m & 0 \\ 0 & 0 & \Delta_a^m \end{pmatrix}, \quad (3-64)$$

and

$$\mathcal{E}(x) = \mathcal{H}_{eff}^{(m)}(x) - \mathcal{H}_0(x) + \text{diag}(0, \Delta_s, \Delta_a) - \frac{V + \Delta_s + \Delta_a - \Delta_s^m - \Delta_a^m}{3} I,$$

$$\mathcal{E}(x) = V c_{13}^2 \begin{pmatrix} 0 & \sin 2\theta_{12}/2 & c_{12} s_{13}/c_{13} \\ \sin 2\theta_{12}/2 & 0 & s_{12} s_{13}/c_{13} \\ c_{12} s_{13}/c_{13} & s_{12} s_{13}/c_{13} & 0 \end{pmatrix} + \mathcal{O}(V^2). \quad (3-65)$$

Here, $\Delta_s = \Delta m_{21}^2/(2E)$ and $\Delta_a = \Delta m_{31}^2/(2E)$ are the eigenvalues of the Hamiltonian in vacuum. $\Delta_s^m \approx \Delta_s \sqrt{\sin^2 2\theta_{12} + (\cos 2\theta_{12} - (V c_{13}^2/\Delta_s))^2} + \mathcal{O}(s_{13}^2 (V^2/\Delta_a))$ and $\Delta_a^m \approx \Delta_a + \mathcal{O}(V)$ are the eigenstates of the Hamiltonian in matter.

The time evolution of the neutrino state, Eq. (3-62), can be obtained by the evolution matrix $S(x_f, x_o)$ from the initial point x_o to the final point x_f ,

$$S(x_f, x_o) = T e^{-i \int_{x_o}^{x_f} \mathcal{H}_{eff}^{(m)}(x) dx}, \quad (3-66)$$

where T is the so-called time-ordering or Dyson operator. Now, let us divide the trajectory that neutrinos follow inside the earth into n equal parts of size $\Delta x = (x_f - x_o)/n$, each of them with constant density $\rho(x_j)$. Then according to Eq. (3-63) we have

$$S(x_f, x_o) = T \prod_{j=n \dots 1} e^{-i \mathcal{H}_{eff}^{(m)}(x_j) \Delta x} = T \prod_{j=n \dots 1} (D_j - i \mathcal{E}(x_j) \Delta x), \quad (3-67)$$

where

$$D_j = \begin{pmatrix} 1 & 0 & 0 \\ 0 & \exp(-i \Delta_s^m(x_j) \Delta x) & 0 \\ 0 & 0 & \exp(-i \Delta_a^m(x_j) \Delta x) \end{pmatrix}, \quad (3-68)$$

is the evolution matrix of the matter eigenstates in the j -th layer, $\Delta_s^m(x_j) \Delta x$ and $\Delta_a^m(x_j) \Delta x$ the relative phase between the matter eigenstates in the layer j , for the solar and atmospheric sectors respectively. In the limit $n \rightarrow \infty$ and $\Delta x \rightarrow 0$ the sums must be substituted by integrals:

$$\prod_{j=k\dots n} \exp(-i \Delta_s^m(x_j) \Delta x) \longrightarrow \exp(-i \phi_{x_k \rightarrow x_n}^m), \quad (3-69)$$

and

$$\prod_{j=k\dots n} \exp(-i \Delta_a^m(x_j) \Delta x) \longrightarrow \exp(-i \psi_{x_k \rightarrow x_n}^m), \quad (3-70)$$

where, in general,

$$\phi_{p_1 \rightarrow p_2}^m \equiv \int_{p_1}^{p_2} dx \Delta_s^m(x) \quad \text{and} \quad \psi_{p_1 \rightarrow p_2}^m \equiv \int_{p_1}^{p_2} dx \Delta_a^m(x), \quad (3-71)$$

After some calculations, the expression for the S matrix in the mass eigenstates basis can be written as

$$S(x_f, x_o) = A - i \int_{x_o}^{x_f} dx B \mathcal{E} C, \quad (3-72)$$

where

$$A = \begin{pmatrix} 1 & 0 & 0 \\ 0 & \exp(-i \phi_{x_o \rightarrow x_f}^m) & 0 \\ 0 & 0 & \exp(-i \psi_{x_o \rightarrow x_f}^m) \end{pmatrix}, \quad (3-73)$$

$$B = \begin{pmatrix} 1 & 0 & 0 \\ 0 & \exp(-i \phi_{x \rightarrow x_f}^m) & 0 \\ 0 & 0 & \exp(-i \psi_{x \rightarrow x_f}^m) \end{pmatrix}, \quad (3-74)$$

and

$$C = \begin{pmatrix} 1 & 0 & 0 \\ 0 & \exp(-i \phi_{x_o \rightarrow x}^m) & 0 \\ 0 & 0 & \exp(-i \psi_{x_o \rightarrow x}^m) \end{pmatrix}. \quad (3-75)$$

Now, by using the matrix elements of both the mixing matrix, Eq. (3-6), and the evolution matrix Eq. (3-72), we can compute the probability of the mass-to-flavor transition. This is

$$P_{\nu_i \rightarrow \nu_\alpha}(x) = \left| U_{\alpha j} S_{ji}(x) \right|^2. \quad (3-76)$$

Therefore, the transition probabilities of the mass eigenstates to ν_e can be written as

$$P_{\nu_1 \rightarrow \nu_e}(x) = c_{13}^2 c_{12}^2 - \frac{c_{13}^4 \sin^2 \theta_{12}}{2} \int_{x_o}^{x_f} dx V(x) \sin \phi_{x \rightarrow x_f}^m - 2c_{12}^2 c_{13}^2 s_{13}^2 \int_{x_o}^{x_f} dx V(x) \sin \psi_{x \rightarrow x_f}^m, \quad (3-77)$$

$$\begin{aligned}
P_{\nu_2 \rightarrow \nu_e}(x) = & c_{13}^2 s_{12}^2 + \frac{c_{13}^4 \sin^2 \theta_{12}}{2} \int_{x_o}^{x_f} dx V(x) \sin \phi_{x \rightarrow x_f}^m - \\
& 2s_{12}^2 c_{13}^2 s_{13}^2 \int_{x_o}^{x_f} dx V(x) \sin(\psi_{x \rightarrow x_f}^m - \phi_{x \rightarrow x_f}^m), \tag{3-78}
\end{aligned}$$

$$\begin{aligned}
P_{\nu_3 \rightarrow \nu_e}(x) = & s_{13}^2 + 2c_{12}^2 c_{13}^2 s_{13}^2 \int_{x_o}^{x_f} dx V(x) \sin \psi_{x \rightarrow x_f}^m + \\
& 2s_{12}^2 c_{13}^2 s_{13}^2 \int_{x_o}^{x_f} dx V(x) \sin(\psi_{x \rightarrow x_f}^m - \phi_{x \rightarrow x_f}^m). \tag{3-79}
\end{aligned}$$

As a good approximation, the third terms in Eqs. (3-77), (3-78) and (3-79) can be omitted, since they are much smaller than the first ones because the function $\psi_{x \rightarrow x_f}^m$ oscillates faster than $\phi_{x \rightarrow x_f}^m$ and they also have a prefactor s_{13}^2 , i.e.,

$$P_{\nu_1 \rightarrow \nu_e}(x) \approx c_{13}^2 c_{12}^2 - \frac{c_{13}^4 \sin^2 \theta_{12}}{2} \int_{x_o}^{x_f} dx V(x) \sin \phi_{x \rightarrow x_f}^m, \tag{3-80}$$

$$P_{\nu_2 \rightarrow \nu_e}(x) \approx c_{13}^2 s_{12}^2 + \frac{c_{13}^4 \sin^2 \theta_{12}}{2} \int_{x_o}^{x_f} dx V(x) \sin \phi_{x \rightarrow x_f}^m, \tag{3-81}$$

$$P_{\nu_3 \rightarrow \nu_e}(x) \approx s_{13}^2 \tag{3-82}$$

If we ignore the effect of θ_{13} on CCSN neutrinos crossing the Earth, it is possible to recreate the two-neutrino scenario results, since $P_{\nu_3 \rightarrow \nu_e}(x) \sim 0$. Under this assumption, we have:

$$P_{\nu_2 \rightarrow \nu_e}(x) = 1 - P_{\nu_1 \rightarrow \nu_e}(x) \approx \sin^2 \theta_{12} + f_{reg} \tag{3-83a}$$

$$f_{reg} = \frac{\sin^2 2\theta_{12}}{2} \int_{x_o}^{x_f} dx V(x) \sin \phi_{x \rightarrow x_f}^m, \tag{3-83b}$$

where the term f_{reg} is known in the literature as regeneration factors [179]. We can understand these factors as the result of the interaction of the neutrinos with the electrons of the Earth; due to de fact that the neutrino mass eigenstates in vacuum do not coincide with the neutrino mass eigenstates in the Earth matter, the presence of these terms in the probabilities $P_{\nu_1 \rightarrow \nu_e}$ and $P_{\nu_2 \rightarrow \nu_e}$ allows the partial restoration of the neutrino flavor oscillations. In Fig. 3.4 we show some example of the regeneration factors as a function of neutrino energy for three different distances traveled by neutrinos, $L = 4000$ km (left panels), $L = 8000$ km (middle panels) and $L = 12000$ km (right panels) for neutrino (upper panels) and anti-neutrinos (lower panels). For the Earth matter density profile we used PREM model and computed the proba-

bilities by numerically solving the neutrino evolution equation. These results agree very well with those obtained from Eq. (3-83). On the other hand, the regeneration factors corresponding to the distances of 8000 km and 12000 km can be compared with the results shown in Fig. 1 of [61] which are in good agreement with our results.

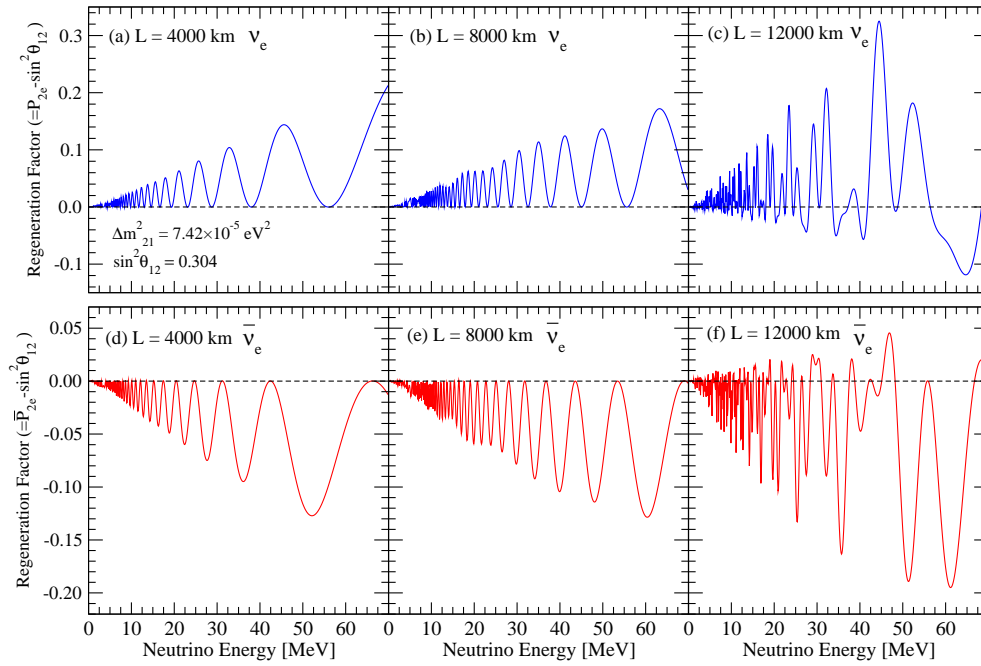


Figure 3.4: Regeneration factors as a function of neutrino energy are shown for $L = 4000$ km (left panels), $L = 8000$ km (middle panels) and $L = 12000$ km (right panels) for neutrino (upper panels) and anti-neutrinos (lower panels).

4

Neutrino Decay

As we have already discussed, neutrinos can oscillate in flavor. The evidence supporting the existence of this physical phenomenon comes from many experiments using solar, atmospheric, reactor, and accelerator neutrinos. Thanks to these results, today we know that at least two neutrinos are massive (therefore either Dirac or Majorana particles), which allows us to contemplate the possibility of neutrino decay [180, 181]. In the early 70's, neutrino decay was considered as a possible solution to the problem of solar neutrinos [182, 183], but with the Large Mixing Angle MSW solution to this problem, neutrino decay came to be considered as a subdominant effect that to date has not been observed. From a phenomenological point of view, based on the nature of the decay products there are two kinds of neutrino decay [184]:

1. *Invisible neutrino decay*: In this type of decay, the final states cannot be observed in our detectors, either because they are sterile or because their energies are too low that their interactions with the targets in the detector do not produce a measurable signal.
2. *Visible neutrino decay*: Where the final states are detectable lighter active neutrinos. Neutrinos that result from visible decay differ from any other light neutrino in the energy, they have a lower energy than the parent neutrino. This fact is reflected in an increase in the number of neutrinos in the lower energy bins.

The structure of this chapter is the following: In section 4.1, we give a short summary of the bounds on the neutrino lifetime. According to Ref. [185] In section 4.2, we present a broad outline of the vacuum neutrino decay via a Nambu-Goldstone boson. It should be noted that for the purposes of this work it is not necessary to consider a particular neutrino decay model, since the discussion of our problem will be approached within the framework of invisible decay. In section 4.3 we present the three decay possibilities that we use in this work: no decay (scenario S1), $\sim 50\%$ decay (scenario S2) and 100% decay (scenario S3). Finally, in section 4.4, one of the most important sections of the

thesis, we show the effect that neutrino decay has on the magnitude of Earth matter effects.

4.1

Neutrino lifetime

The relevant quantity for neutrino decay in the observer's frame is $\tau E/(mD)$, where τ is the rest frame lifetime for the neutrino decay channel, m and E are respectively the mass and energy of the parent mass eigenstate and D is the distance between the source (CCSN) and the detector. The factor E/m takes account time dilatation effects due to the ultra-relativistic nature of the neutrino. If the energy corrections are higher than the first order, we can approximate the energy of the parent mass eigenstate by the average energy $\langle E_\nu \rangle$ of the produced flavor eigenstate [186]. For the distance $D = 10$ kpc, and typical energy of CCSN neutrinos, ~ 10 MeV, we can roughly estimate the condition for a large decay effect, just by considering the situation where $\mathcal{O}(\tau E/(mD)) \sim 1$. This is

$$\frac{\tau}{m} \sim \frac{D}{E} \sim 10^5 \left[\frac{D}{10 \text{ kpc}} \right] \left[\frac{E}{10 \text{ MeV}} \right]^{-1} \frac{\text{s}}{\text{eV}}. \quad (4-1)$$

In general, we refer the condition $\tau/m \sim D/E$ as the kinematic estimate [26]; this condition helps us to place lower bounds on neutrino lifetime. In an informal way, we can establish three types of bounds:

1. *Weak*: The weakest constraints come from atmospheric, accelerator and reactor neutrinos. From the combined Super-Kamiokande, K2K and MINOS data the lifetime of ν_3 is $\tau_3/m_3 > 2.9 \times 10^{-10}$ s/eV at 90% C.L. [25]. It is expected that JUNO and DUNE can obtain a better bounds on the lifetime of ν_3 . In Ref. [26], under the assumption of invisible neutrino decay, its authors found that future medium-baseline reactor neutrino experimentes like JUNO can constrain $\tau_3/m_3 > 5.5 \times 10^{-11}$ s/eV at 99% C.L.. While Ref. [27] found that DUNE will have a sensitivity of $\tau_3/m_3 \geq 4.27 \times 10^{-11}$ s/eV at 90% C.L.. Studies regarding visible neutrino decay, such as those considered in Ref. [28] constraint in the inverted ordering for both KamLAND and JUNO the lifetime of $\tau_2/m_2 \geq 1.4 \times 10^{-9}$ s/eV at 90% C.L. and in the normal mass ordering for JUNO $\tau_3/m_3 \geq 1.0 \times 10^{-10}$ s/eV at 90% C.L..

2. *Intermediate*: In this group we find the imposed constraints on the

lifetime of ν_1 or ν_2 from solar neutrinos. Model-independent¹ bounds on the lifetime of ν_2 using the ^8B solar neutrinos constrain $\tau_2/m_2 > 10^{-3}$ s/eV, while those involving low energy solar neutrinos² constrain $\tau_1/m_1 > 10^{-4}$ s/eV [29, 30, 31].

3. *Strong:* The strongest constraint on neutrino decay comes from SN 1987A. However, due to the limited number of observed ν_e events and the uncertainties in the CCSN fluxes, this bound may apply either to ν_1 or ν_2 , not at the same time. The kinematic estimate is $\tau_{1,2}/m_{1,2} > 5.7 \times 10^5$ s/eV [147]

Non-radiative neutrino decay lifetime bounds depend on neutrino nature, i.e., Dirac or Majorana, and also whether the result products are active (visible neutrinos) or sterile. In the case of active neutrinos, lifetime bounds can be quite different depending on the neutrino mass ordering, if it is normal or inverted, see e.g. [28].

4.2

Nambu-Goldstone neutrino decay model

Within the minimally extended standard model of elementary particles, neutrino decay can occur within the standard electroweak interactions, but the expected neutrino lifetimes are much longer than the age of the Universe [187]. On the other hand, beyond the standard model neutrinos can decay faster. The simplest model is that neutrinos couple to a massless boson carrying lepton number [182].

For simplicity, we write this section assuming the neutrino as a Majorana particle³, in which case the neutrino interact with a Nambu-Goldstone boson (ϕ) via a combination of Yukawa scalar (g_{ij}) and-or pseudoscalar (g'_{ij}) couplings [188]. This boson commonly called Majoron is produced as a result of spontaneous breaking of the global lepton number symmetry and it is the responsible of the decay channel $\nu_i \rightarrow \nu_j + \phi$ [189, 190, 191, 181, 192]. Where, the mass eigenstates (ν_i) are usually referred to as parent neutrinos and the mass eigenstates (ν_j) as daughter neutrinos.

¹Model-independent bounds to neutrino decay are constraints obtained from experiments where the number of neutrinos produced in the source can be compared to the number of neutrinos detected some distance away [29].

²The obtained bounds for ν_1 from $p-p$ or ^7Be solar neutrinos are stronger than that for ν_2 with the ^8B solar data, because D/E is greater for these low neutrinos than for those of the ^8B line

³If neutrinos are Dirac particles, the decay channel $\nu_i \rightarrow \bar{\nu}_{jR} + \chi$ is possible. Here, $\bar{\nu}_{jR}$ is a right-handed singlet and χ is an iso-singlet scalar [193].

Therefore, the relevant part of the Lagrangian that describe this non-standard interaction is given by

$$\mathcal{L} \supset \frac{1}{2} \sum_{i,j(i \neq j)}^3 (g_{ij} \bar{\nu}_i \nu_j + g'_{ij} \bar{\nu}_i i\gamma_5 \nu_j) \phi. \quad (4-2)$$

Now let us consider a large collection of mass eigenstates of the same specie (e.g., incoherent mass eigenstate fluxes at the surface of a CCSN) and denote by $N(t)$ the number of them at time t . Some time later dt , we observe that by virtue of their mass, $\Gamma N(t)dt$ of them could decay. Where Γ is the probability per unit of time that a given neutrino will decay, or in other words it is the decay rate. Since the change in the number of neutrinos will be $dN = -\Gamma N(t)dt$, the survival probability for a mass eigenstate ν_i in the rest reference frame follows the exponential decay formula

$$\mathcal{P}_{i \rightarrow i} = \left| \langle \nu_i, t | \nu_i, t + dt \rangle \right|^2 = e^{-\Gamma_i t}. \quad (4-3)$$

In order to obtain Γ , we need to calculate two quantities: (1) the amplitude (\mathcal{M}) of the process, that according to the Lagrangian in Eq. (4-2) leads to two different allowed decay channels [43]: chirality-preserving processes ($\nu_i \rightarrow \nu_j + \phi$) and chirality-violating processes ($\nu_i \rightarrow \bar{\nu}_j + \phi$); (2) A phase space factor, which depends on the masses, energies and momenta of the neutrinos involved [194, 195].

Now, following Ref. [185]. The dynamical information of the avobe-mentioned processes is given by

$$\begin{aligned} \mathcal{M}(\nu_i \rightarrow \nu_j + \phi) &= \overbrace{\frac{g_{ij}}{2} \bar{\nu}_j(p_j, s_j) \nu_i(p_i, s_i)}^{\mathcal{M}_1} \\ &+ i \overbrace{\frac{g'_{ij}}{2} \bar{\nu}_j(p_j, s_j) \gamma_5 \nu_i(p_i, s_i)}^{\mathcal{M}_2}, \end{aligned} \quad (4-4)$$

where, we have assumed a mass hierarchy $m_i > m_j$ ($i \neq j$) and computed the amplitudes in the laboratory reference system. p_x, s_x ($x = i, j$) are the momentum and the spin of the neutrino, respectively. Then, the squared modulus of the transition amplitude can be written as

$$|\mathcal{M}|^2 = |\mathcal{M}_1|^2 + |\mathcal{M}_2|^2 + 2\mathcal{R}e(\mathcal{M}_1 \mathcal{M}_2^*), \quad (4-5)$$

where,

$$\left| \mathcal{M}_1 \right|^2 = \frac{g_{ij}^2}{4m_i m_j} \left[(p_j \cdot p_i + m_i m_j)(1 - s_j \cdot s_i) - (p_j \cdot s_i)(p_i \cdot s_j) + 4(p_i \cdot s_i)(p_j \cdot s_j) \right], \quad (4-6)$$

$$\left| \mathcal{M}_2 \right|^2 = \frac{g'_{ij}{}^2}{4m_i m_j} \left[(p_j \cdot p_i - m_i m_j)(1 + s_j \cdot s_i) - (p_j \cdot s_i)(p_i \cdot s_j) + 4(p_i \cdot s_i)(p_j \cdot s_j) \right], \quad (4-7)$$

and

$$2\mathcal{R}e\left(\mathcal{M}_1\mathcal{M}_2^*\right) = -\frac{g_{ij}g'_{ij}}{2m_i m_j} \epsilon^{\mu\nu\lambda\sigma} p_{i\mu} s_{i\nu} p_{j\lambda} s_{j\sigma}. \quad (4-8)$$

To evaluate these expressions for the case of either chirality-preserving or chirality-violating processes, we set $s_i = s_L$ and $s_j = \pm s_{L(R)}$, with

$$s_R^\mu = -s_L^\mu = \frac{p^\mu}{m\beta} - \frac{\sqrt{1-\beta^2}}{\beta} \eta^{\mu 0}, \quad (4-9)$$

where β is the neutrino velocity relative to the speed of light, $\eta_{\mu\nu}$ is the Minkowski metric, and the subscripts L and R denote neutrinos and anti-neutrinos, respectively. Therefore, we find that

$$\begin{aligned} p \cdot s &= p^\mu \left(\frac{p_\mu}{m\beta} - \frac{\sqrt{1-\beta^2}}{\beta} \eta_{\mu 0} \right), \\ &= \frac{p^2}{m\beta} - \frac{\sqrt{1-\beta^2}}{\beta} E, \\ &= 0, \end{aligned} \quad (4-10)$$

and,

$$\begin{aligned} &\epsilon^{\mu\nu\lambda\sigma} p_{i\mu} s_{i\nu} p_{j\lambda} s_{j\sigma} = \\ &\epsilon^{\mu\nu\lambda\sigma} \left(\frac{\sqrt{(1-\beta_i^2)(1-\beta_j^2)}}{\beta_i \beta_j} p_{i\mu} p_{i\lambda} \eta_{\nu 0} \eta_{\sigma 0} + \frac{1}{m_i m_j \beta_i \beta_j} p_{i\mu} p_{i\nu} p_{j\lambda} p_{j\sigma} \right. \\ &\left. - \frac{\sqrt{1-\beta_i^2}}{m_i \beta_i \beta_j} p_{j\lambda} p_{j\sigma} p_{i\mu} \eta_{\nu 0} - \frac{\sqrt{1-\beta_j^2}}{m_i \beta_i \beta_j} p_{j\lambda} p_{j\sigma} p_{i\mu} \eta_{\nu 0} \right). \end{aligned} \quad (4-11)$$

Since the Levi-Civita tensor $\epsilon^{\mu\nu\lambda\sigma}$ is antisymmetric under the interchange of any pair of indices, the contraction with the symmetric term within parentheses (...) is zero. Therefore $\mathcal{R}e\left(\mathcal{M}_1\mathcal{M}_2^*\right) = 0$, and equation Eq. (4-5) reduces to

$$\begin{aligned}
|\mathcal{M}|^2 = & \frac{g_{ij}^2}{4m_i m_j} \left[(p_j \cdot s_i)(p_i \cdot s_j) - (p_j \cdot p_i)(s_j \cdot s_i) + p_j \cdot p_i + m_i m_j - \right. \\
& \left. m_i m_j (s_j \cdot s_i) \right] + \frac{g'_{ij}{}^2}{4m_i m_j} \left[(p_j \cdot p_i)(s_j \cdot s_i) - (p_j \cdot s_i)(p_i \cdot s_j) + \right. \\
& \left. p_j \cdot p_i - m_i m_j - m_i m_j (s_j \cdot s_i) \right]. \quad (4-12)
\end{aligned}$$

To calculate $|\mathcal{M}(\nu_i \rightarrow \nu_j + \phi)|^2$, we first find:

$$p_{i\mu} \left(-\frac{p_j^\mu}{m_j \beta_j} + \frac{\sqrt{1 - \beta_j^2}}{\beta_j} \eta^{\mu 0} \right) = -\frac{p_i \cdot p_j}{m_j \beta_j} + \frac{\sqrt{1 - \beta_j^2}}{\beta_j} E_i, \quad (4-13a)$$

$$p_{j\mu} \left(-\frac{p_i^\mu}{m_i \beta_i} + \frac{\sqrt{1 - \beta_i^2}}{\beta_i} \eta^{\mu 0} \right) = -\frac{p_i \cdot p_j}{m_i \beta_i} + \frac{\sqrt{1 - \beta_i^2}}{\beta_i} E_j, \quad (4-13b)$$

and then,

$$\begin{aligned}
(p_i \cdot s_j)(p_j \cdot s_i) = & \frac{\sqrt{(1 - \beta_i^2)(1 - \beta_j^2)}}{\beta_i \beta_j} E_i E_j - \frac{(p_i \cdot p_j)\sqrt{1 - \beta_j^2}}{m_i \beta_i \beta_j} E_i \\
& - \frac{(p_i \cdot p_j)\sqrt{1 - \beta_i^2}}{m_j \beta_i \beta_j} E_j + \frac{(p_i \cdot p_j)^2}{m_i m_j \beta_i \beta_j}, \quad (4-14)
\end{aligned}$$

$$\begin{aligned}
(p_i \cdot p_j)(s_i \cdot s_j) = & \frac{\sqrt{(1 - \beta_i^2)(1 - \beta_j^2)}}{\beta_i \beta_j} (p_i \cdot p_j) - \frac{(p_i \cdot p_j)\sqrt{1 - \beta_j^2}}{m_i \beta_i \beta_j} E_i \\
& - \frac{(p_i \cdot p_j)\sqrt{1 - \beta_i^2}}{m_j \beta_i \beta_j} E_j + \frac{(p_i \cdot p_j)^2}{m_i m_j \beta_i \beta_j}, \quad (4-15)
\end{aligned}$$

and,

$$\begin{aligned}
s_i \cdot s_j = & \frac{\sqrt{(1 - \beta_i^2)(1 - \beta_j^2)}}{\beta_i \beta_j} - \frac{\sqrt{1 - \beta_j^2}}{m_i \beta_i \beta_j} E_i - \frac{\sqrt{1 - \beta_i^2}}{m_j \beta_i \beta_j} E_j \\
& + \frac{p_i \cdot p_j}{m_i m_j \beta_i \beta_j}. \quad (4-16)
\end{aligned}$$

Now, substituting Eqs. (4-14), (4-15) and (4-16) in Eq. (4-12) we get that

$$\begin{aligned}
|\mathcal{M}_1|^2 = & \frac{g_{ij}^2}{4\beta_i \beta_j} \left[\frac{m_i^2 + m_j^2}{2} \left(\frac{\beta_i \beta_j}{m_i m_j} - \frac{1}{m_i m_j} - \frac{1}{E_i E_j} \right) + \right. \\
& \left. \frac{m_i E_j}{m_j E_i} + \frac{m_j E_i}{m_i E_j} - \frac{m_i m_j}{E_i E_j} + \beta_i \beta_j + 1 \right], \quad (4-17)
\end{aligned}$$

and,

$$\begin{aligned} |\mathcal{M}_2|^2 = \frac{g_{ij}^{\prime 2}}{4\beta_i\beta_j} & \left[\frac{m_i^2 + m_j^2}{2} \left(\frac{\beta_i\beta_j}{m_i m_j} - \frac{1}{m_i m_j} + \frac{1}{E_i E_j} \right) + \right. \\ & \left. \frac{m_i E_j}{m_j E_i} + \frac{m_j E_i}{m_i E_j} - \frac{m_i m_j}{E_i E_j} - \beta_i\beta_j - 1 \right]. \end{aligned} \quad (4-18)$$

Since neutrinos are ultrarelativistic particles, i.e., $\beta_i = \beta_j \approx 1$ and $E_x \gg m_x (x = i, j)$ the amplitud of a chirality-preserving neutrino decay can be written as

$$\left| \mathcal{M}(\nu_i \rightarrow \nu_j + \phi) \right|^2 = \frac{g_{ij}^2}{2}(A + 2) + \frac{g_{ij}^{\prime 2}}{2}(A - 2), \quad (4-19)$$

where

$$A = \frac{m_j E_i}{m_i E_j} + \frac{m_i E_j}{m_j E_i}. \quad (4-20)$$

In the case of a chirality-violating neutrino decay, $\left| \mathcal{M}(\nu_i \rightarrow \bar{\nu}_j + \phi) \right|^2$ is found by substitute $s_j \rightarrow -s_j$. Therefore in the ultrarelativistic approximation the neutrino decay amplitude is

$$\left| \mathcal{M}(\nu_i \rightarrow \bar{\nu}_j + \phi) \right|^2 = \frac{g_{ij}^2 + g_{ij}^{\prime 2}}{4} \left(\frac{m_i^2 + m_j^2}{m_i m_j} - A \right). \quad (4-21)$$

Now, adopting spherical coordinates for the kinematics in the phase space, the Golden Rule gives us the differential decay rate for each decay channel [194], that is

$$\frac{d\Gamma_{i \rightarrow j}}{dE_j} = \left(\frac{m_i}{E_i} \right) \frac{m_j}{4\pi |\mathbf{p}_i|} |\mathcal{M}(E_j)|^2. \quad (4-22)$$

Using Eqs. (4-19) and (4-21), we can integrate the differential decay rate over the energy range $(m_j/m_i)^2 E_i \leq E_j \leq E_i$ [147]. Thus, the total decay rates are given by

$$\Gamma(\nu_i \rightarrow \nu_j + \phi) = \left(\frac{m_i m_j}{16\pi E_i} \right) \left[g_{ij}^2 f(x) + g_{ij}^{\prime 2} g(x) \right], \quad (4-23a)$$

$$\Gamma(\nu_i \rightarrow \bar{\nu}_j + \phi) = \left(\frac{m_i m_j}{16\pi E_i} \right) \left[g_{ij}^2 + g_{ij}^{\prime 2} \right] k(x), \quad (4-23b)$$

where $x = m_i/m_j$, and the auxiliary functions f , g and k are given by

$$f(x) = \frac{x}{2} + 2 + \frac{2}{x} \ln x - \frac{2}{x^2} - \frac{1}{2x^3}, \quad (4-24a)$$

$$g(x) = \frac{x}{2} - 2 + \frac{2}{x} \ln x + \frac{2}{x^2} - \frac{1}{2x^3}, \quad (4-24b)$$

$$k(x) = \frac{x}{2} - \frac{2}{x} \ln x - \frac{1}{2x^3}. \quad (4-24c)$$

Finally, we can see that in the limit $m_i \gg m_j$ the total decay rates for both chirality-preserving and chirality-violating decays become equal. This is

$$\Gamma(\nu_i \rightarrow \nu_j + \phi) = \Gamma(\nu_i \rightarrow \bar{\nu}_j + \phi) = \frac{g_{ij}^2 + g'_{ij}{}^2}{32\pi E_i} m_i^2. \quad (4-25)$$

With this result, we can estimate the neutrino lifetime as

$$\tau \equiv \frac{1}{\Gamma} = \frac{32\pi E_i}{m_i^2(g_{ij}^2 + g'_{ij}{}^2)}. \quad (4-26)$$

Model-dependent bounds of neutrino lifetime depend on the neutrino nature, i.e., Dirac or Majorana, and also whether the result products are active (visible neutrinos) or sterile. In the case of active neutrinos, lifetime bounds can be quite different if neutrino mass ordering is normal or inverted.

4.3

Neutrino decay scenarios adopted in this work

Before we begin with the discussion of the combined effect of the resonant flavor conversion inside the star, i.e., Eqs. (3-56) and (3-57), the ν_2 decay while in flight to the detector and the Earth matter effects, on the neutrino signal from supernova. It is important to make the following aspects clear: (1) In the previous section we considered neutrino decay in the context of Majoron model only for the sake of completeness. Hereafter in this work, we do not consider any particular model of neutrino decay but just assume that the product of neutrino decay are not observable from a phenomenological point of view, that is invisible neutrino decay. And (2), we ignore for simplicity any decay effects of neutrinos inside the supernova.

Let us start by analyzing the general case where the ν_i state can decay into some undetectable states with a decay probability r_i ($i = 1, 2$ or 3), which from now on will be called the decay parameter. In the observer's reference frame, we define it as

$$r_i \equiv 1 - \exp\left(-\frac{D}{E} \frac{m_i}{\tau_i}\right), \quad (4-27)$$

where m_i and τ_i are the mass and the lifetime of the i -th neutrino mass eigenstate, respectively. E and D are, respectively, the neutrino energy and the traveled neutrino distance.

In the presence of neutrino decay, CCSN neutrino fluxes at Earth can be explicitly written in terms of the decay parameter, the time-integrated primary

spectra and the mixing parameters, i.e.,

$$F_{\nu_e} \approx (1 - r_1 c_{12}^2 - r_2 s_{12}^2) F_{\nu_x}^0, \quad (4-28a)$$

$$F_{\bar{\nu}_e} \approx c_{12}^2(1 - r_1) F_{\bar{\nu}_e}^0 + s_{12}^2(1 - r_2) F_{\bar{\nu}_x}^0, \quad (4-28b)$$

$$2F_{\nu_x} = (1 - r_3) F_{\nu_e}^0 + (1 - r_2) F_{\nu_x}^0, \quad (4-28c)$$

$$2F_{\bar{\nu}_x} \approx s_{12}^2(1 - r_1) F_{\bar{\nu}_e}^0 + [1 - r_3 + c_{12}^2(1 - r_2)] F_{\bar{\nu}_x}^0, \quad (4-28d)$$

for the normal mass ordering, and

$$F_{\nu_e} \approx s_{12}^2(1 - r_2) F_{\nu_e}^0 + c_{12}^2(1 - r_1) F_{\nu_x}^0, \quad (4-29a)$$

$$F_{\bar{\nu}_e} \approx (1 - c_{12}^2 r_1 - s_{12}^2 r_2) F_{\bar{\nu}_x}^0, \quad (4-29b)$$

$$2F_{\nu_x} = c_{12}^2(1 - r_2) F_{\nu_e}^0 + [1 - r_3 + s_{12}^2(1 - r_1)] F_{\nu_x}^0, \quad (4-29c)$$

$$2F_{\bar{\nu}_x} \approx (1 - r_1) F_{\bar{\nu}_e}^0 + (1 - r_3) F_{\bar{\nu}_x}^0, \quad (4-29d)$$

for the inverted mass ordering, where energy dependence is implicit. For a more detailed description regarding to the calculation of these fluxes, see Appendix A.

We can see that $r_i = 1$ means that ν_i decay completely whereas $r_i = 0$ corresponds to the case where there is no neutrino decay, i.e. the fluxes are given by the Eqs. (3-58) and (3-59). On the other hand, in the intermediate case, r_i is expected to have energy dependence as shown in Eq. (4-27). Let us focus for a while on the Eq. (4-29a), neutrino decay may completely turn off the chance of observing $F_{\nu_e}^0$ in the electron neutrino flux at the Earth. This feature, which is model-independent (it does not depend on any particular decay model or the CCSN neutrino emission scenarios listed in the table 2.3) characteristic occurs when ν_2 disappear completely, which implies that the neutronization peak will disappear completely from the CCSN neutrino burst.

Since we are mainly interested in the impact of decay for ν_e and $\bar{\nu}_e$ observations at the terrestrial detectors like JUNO, Hyper-K and DUNE, from now on we will ignore the decay of ν_3 because it does not have impact for ν_e and $\bar{\nu}_e$ observations under the considerations made in this thesis and, we consider the following three representative scenarios where the mass eigenstate ν_1 is always stable and the mass eigenstate ν_2 has the possibility to decay:

(S1) $\tau_{1,2}/m_{1,2} \gg 10^5$ s/eV corresponding to the case without neutrino decay, or $r_1 = r_2 = 0$.

(S2) $\tau_1/m_1 \gg 10^5$ s/eV with $\tau_2/m_2 = 10^5$ s/eV, or $r_1 = 0, r_2 \simeq 1 - \exp(-[10 \text{ MeV}/E])$

(S3) $\tau_1/m_1 \gg 10^5$ s/eV but $\tau_2/m_2 \ll 10^5$ s/eV, or $r_1 = 0, r_2 \simeq 1$

4.4

Earth matter effects in the presence of neutrino decay

As commented in the chapter 3, neutrino interactions with the constituents of the Earth matter lead to partial coherence restoration of the neutrino flux incident on the Earth and as a consequence, the CCSN neutrino spectrum [196] is altered. Then, we expect that Eqs (4-28) and (4-29) will get modified as the neutrinos propagate through the Earth as follows,

$$F_{\nu_e}^\oplus \approx (1 - r_1 P_{1e}^\oplus - r_2 P_{2e}^\oplus) F_{\nu_x}^0, \quad (4-30a)$$

$$F_{\bar{\nu}_e}^\oplus \approx \bar{P}_{1e}^\oplus (1 - r_1) F_{\bar{\nu}_e}^0 + \bar{P}_{2e}^\oplus (1 - r_2) F_{\bar{\nu}_x}^0, \quad (4-30b)$$

for the normal mass ordering, and

$$F_{\nu_e}^\oplus \approx P_{2e}^\oplus (1 - r_2) F_{\nu_e}^0 + P_{1e}^\oplus (1 - r_1) F_{\nu_x}^0, \quad (4-31a)$$

$$F_{\bar{\nu}_e}^\oplus \approx (1 - \bar{P}_{1e}^\oplus r_1 - \bar{P}_{2e}^\oplus r_2) F_{\bar{\nu}_x}^0, \quad (4-31b)$$

for the inverted mass ordering, where $P_{ie}^\oplus \equiv P_{\nu_i \rightarrow \nu_e}$ ($\bar{P}_{ie}^\oplus \equiv P_{\bar{\nu}_i \rightarrow \bar{\nu}_e}$) is the probability that a mass eigenstate ν_i ($\bar{\nu}_i$) entering the Earth reaches the detector as ν_e ($\bar{\nu}_e$), which according to Eq. (3-83) depends on neutrino energy, the distance (L) traveled by neutrino inside the Earth and the mixing parameters, Δm_{21}^2 and θ_{12} (in our approximation of ignoring the effect of θ_{13}). As we discussed in chapter 3, All of our calculations involving these probabilities were performed by numerically solving the evolution equation of neutrinos using the PREM model for the matter density profile for the Earth showed in figure 3.3.

The impact of the interaction of the CCSN neutrinos with the electrons of the Earth on the oscillations can be characterized by ΔF_{ν_e} or $\Delta F_{\bar{\nu}_e}$, the difference between the CCSN neutrino spectra with (F_ν^\oplus) and without (F_ν) Earth matter effect as,

$$\Delta F_{\nu_e} \equiv F_{\nu_e}^\oplus - F_{\nu_e} = f_{\text{reg}}(r_1 - r_2) F_{\nu_x}^0, \quad (4-32a)$$

$$\Delta F_{\bar{\nu}_e} \equiv F_{\bar{\nu}_e}^\oplus - F_{\bar{\nu}_e} = \bar{f}_{\text{reg}}[(1 - r_2) F_{\bar{\nu}_x}^0 - (1 - r_1) F_{\bar{\nu}_e}^0], \quad (4-32b)$$

for the normal ordering, and

$$\Delta F_{\nu_e} \equiv F_{\nu_e}^\oplus - F_{\nu_e} = f_{\text{reg}}[(1 - r_2)F_{\nu_e}^0 - (1 - r_1)F_{\nu_x}^0], \quad (4-33a)$$

$$\Delta F_{\bar{\nu}_e} \equiv F_{\bar{\nu}_e}^\oplus - F_{\bar{\nu}_e} = \bar{f}_{\text{reg}}(r_1 - r_2)F_{\bar{\nu}_x}^0, \quad (4-33b)$$

for the inverted ordering. f_{reg} and \bar{f}_{reg} in the above equations are the Earth regeneration factors for ν and $\bar{\nu}$, respectively. Following Eq. (3-83) these factors can be defined as

$$f_{\text{reg}} \equiv P_{2e}^\oplus - s_{12}^2 = c_{12}^2 - P_{1e}^\oplus, \quad (4-34a)$$

$$\bar{f}_{\text{reg}} \equiv \bar{P}_{2e}^\oplus - s_{12}^2 = c_{12}^2 - \bar{P}_{1e}^\oplus. \quad (4-34b)$$

Since the main purpose of this thesis is to study the observability (or not) of the Earth matter effects by using a single detector such as JUNO, Hyper-Kamiokande or DUNE, we stress the fact that ΔF_{ν_e} and $\Delta F_{\bar{\nu}_e}$ are not directly observable because for a given detector location, CCSN neutrinos either pass or not through the Earth so that we can not take the difference of the two neutrino fluxes with and without Earth effects. In this section we use ΔF 's only to get a general idea of the impact that neutrino decay has on the detectability of such matter effects.

In the absence of ν_2 decay, Earth matter effects for CCSN neutrinos only exist for ν_e for IMO and $\bar{\nu}_e$ for NMO, as can be seen in Eqs. (4-32) and (4-33), which is consistent with the discussion in [55]. But with the effects of neutrino decay, the Earth matter effects can exist for both ν_e and $\bar{\nu}_e$ for both mass orderings; roughly speaking, imitating the results that will be obtained if the high resonance (in the star) were partially adiabatic or completely non-adiabatic, as observed in Table 2 of [55]. Therefore, if the Earth matter effects will be observed in both ν_e and $\bar{\nu}_e$ events at the same time, or if the Earth matter effects will be observed in the ν_e channel and simultaneously the neutronization peak will be absent from the CCSN neutrino burst, we could consider these observations as an indication of neutrino decay.

Another important feature that neutrino decay introduces in Eqs. (4-32) and (4-33) is the possibility of observing Earth matter effects even if $F_{\nu_e}^0 = F_{\nu_x}^0$. This scenario could take place during the cooling phase of the newly proto-neutron star, where it has been recently observed (in numerical simulations) a tendency to the equalization of the fluxes. In the special case when ν_2 disappear

completely, ΔF 's take the simplified form

$$\Delta F_{\nu_e}^{\text{NMO}} = \Delta F_{\nu_e}^{\text{IMO}} = -f_{\text{reg}} F_{\nu_x}^0, \quad (4-35a)$$

$$\Delta F_{\bar{\nu}_e}^{\text{IMO}} = -\bar{f}_{\text{reg}} F_{\bar{\nu}_x}^0, \quad (4-35b)$$

$$\Delta F_{\bar{\nu}_e}^{\text{NMO}} = -\bar{f}_{\text{reg}} F_{\bar{\nu}_e}^0. \quad (4-35c)$$

In Figs. 4.1, 4.2 and 4.3 we show the ΔF defined in Eqs. (4-32) and (4-33) as a function of neutrino energy computed for the model D in table 2.3, for the case where $L = 4000, 8000$ and 12000 km, respectively. Each figure shows the Earth matter effects for neutrino (upper panels) and anti-neutrinos (lower panels), for NMO (left panels) and IMO (right panels). The solid blue, green and red curves refer to S1, S2 and S3 scenarios, respectively. In the construction of these figures we have eliminated the dependence of the distance to supernova by normalizing the spectra such that $\int dF_{\nu}^0(E_{\nu})dE_{\nu} = 1$ for all species of neutrino. Figs. 4.1 and 4.2 correspond to neutrinos that only pass through the Earth mantle on their way to the detector, for which they exhibit similar characteristics. On the other hand, Fig. 4.3 differs from the first two due to the fact that neutrinos pass through the Earth core. Another thing that we can notice from these figures is that the larger the decay, the larger the effect on ΔF . That can be seen by comparing the green ($\sim 50\%$ decay) and red (100% decay) curves.

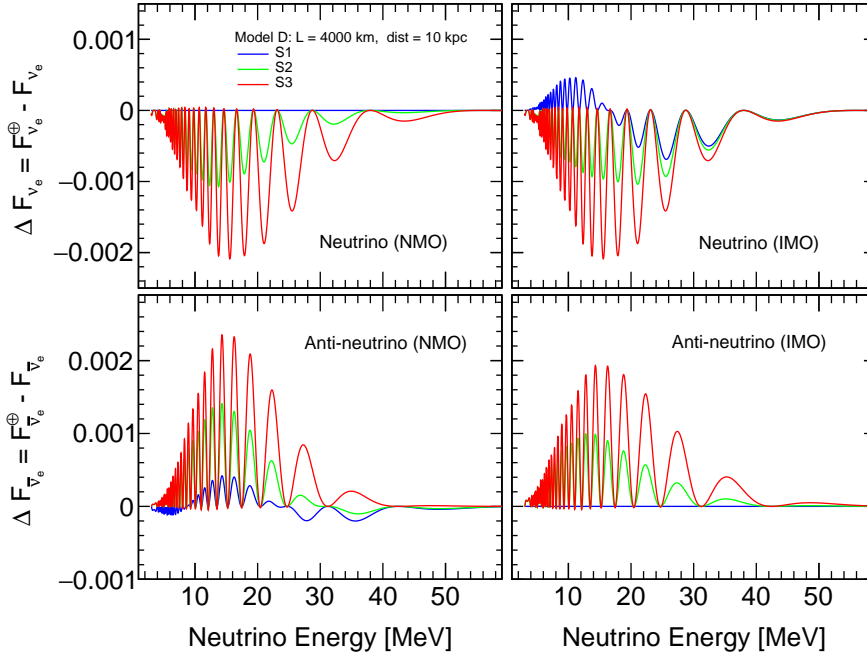


Figure 4.1: ΔF defined in Eqs. (4-32) and (4-33) are shown as a function of neutrino energy computed for $L = 4000$ km .

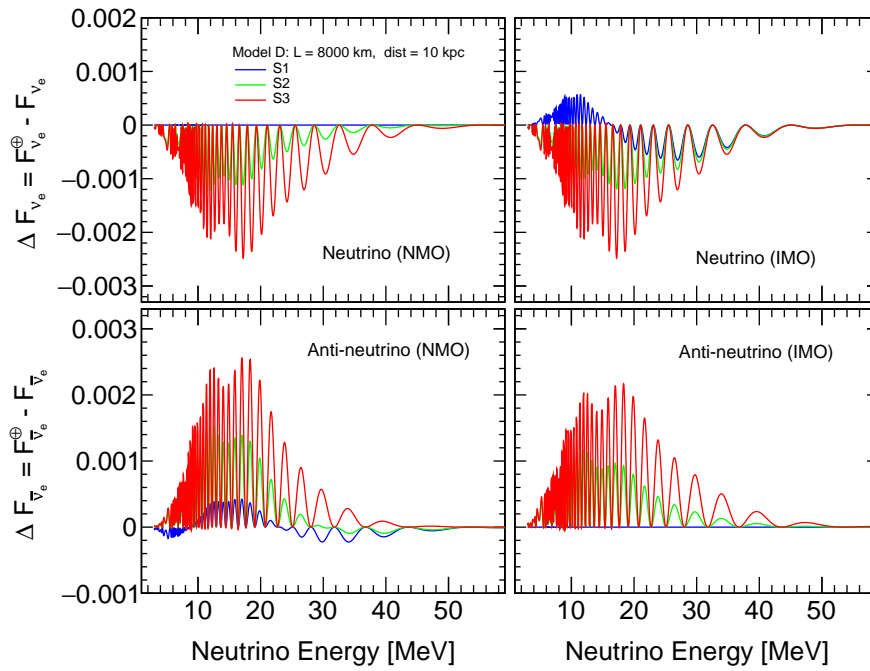


Figure 4.2: ΔF defined in Eqs. (4-32) and (4-33) are shown as a function of neutrino energy computed for $L = 8000$ km.

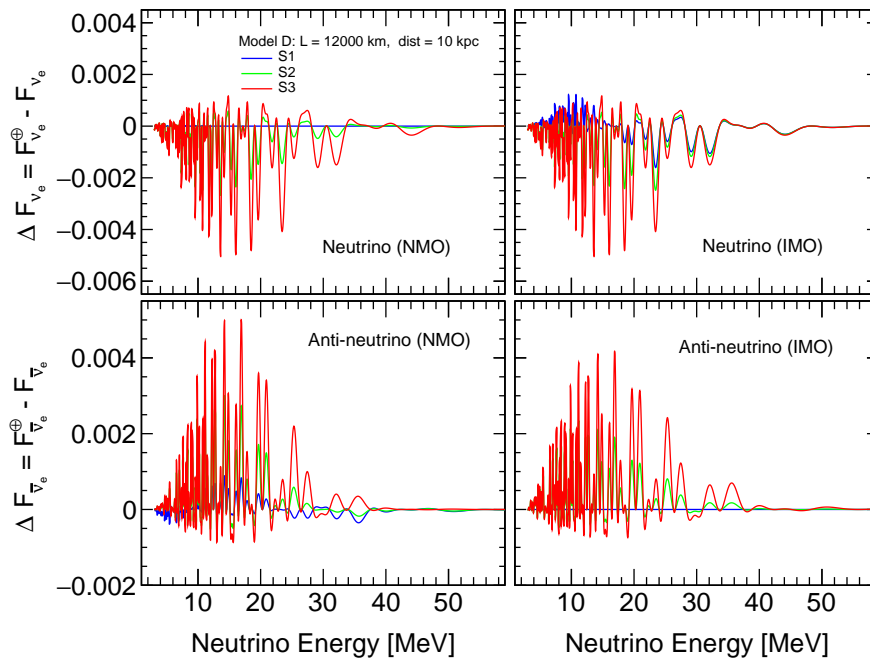


Figure 4.3: ΔF defined in Eqs. (4-32) and (4-33) are shown as a function of neutrino energy computed for $L = 12000$ km.

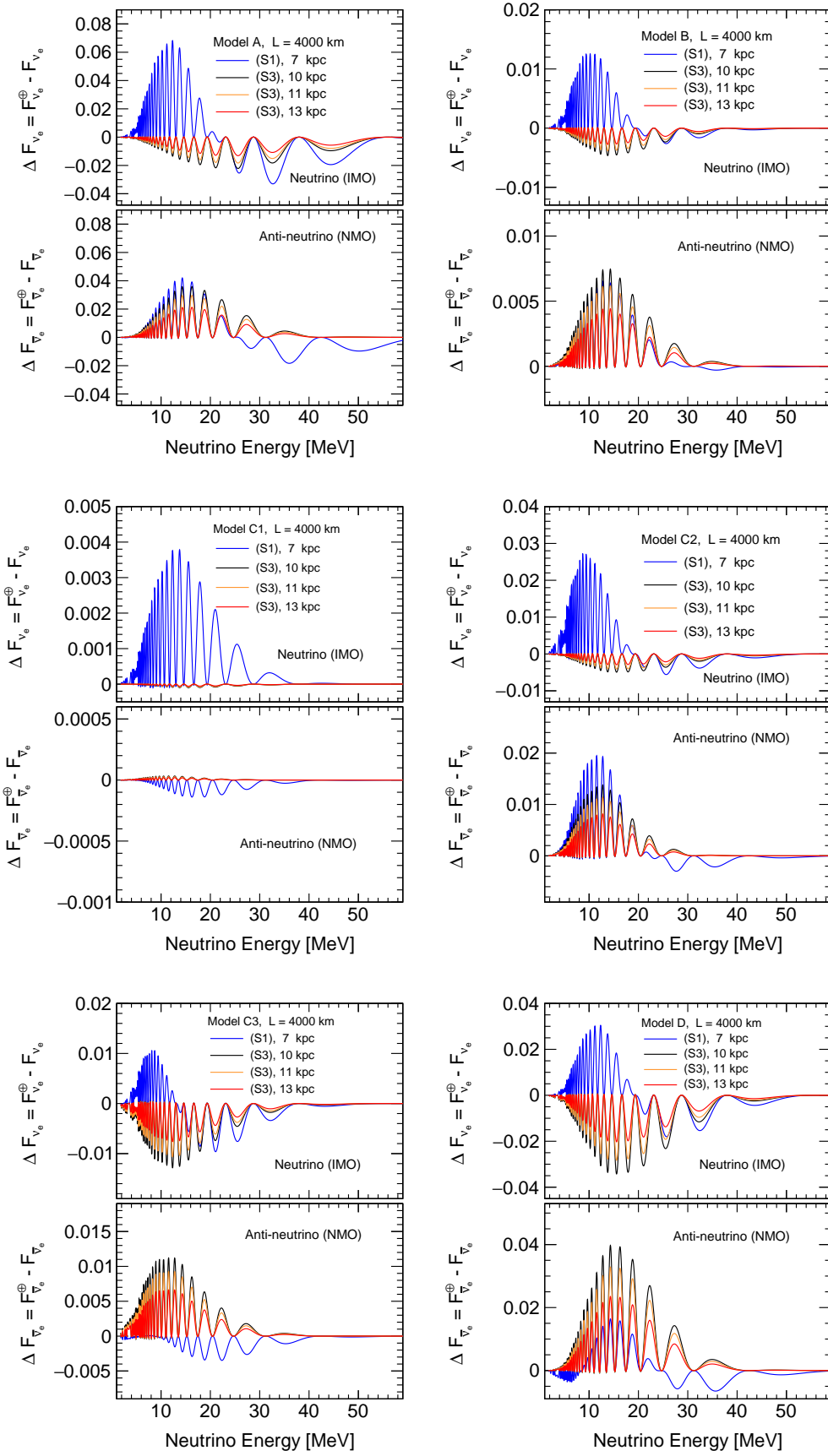


Figure 4.4: ΔF plotted as a function of both the neutrino energy and the distance between the CCSN and the Earth, for each supernova model listed in table 2.3.

On the other hand, in Fig. 4.4 we show a collage of ΔF 's plotted as a function of neutrino energy for each supernova model listed in table 2.3. Each figure shows also the dependence on the distance⁴ between the CCSN and the Earth, for both neutrino (upper panels) and anti-neutrinos (lower panels) channels. In these plots we have omitted the neutrino (NMO) and anti-neutrino (IMO) scenarios since here neutrino decay always increases the possibility of observing matter effects which for the purposes of the following comparison is not relevant. Remember that, in the absence of decay, these observation channels do not exhibit Earth effects.

First of all, we observe that the intensity of the Earth matter effects increases with the proximity of the supernova to the Earth, as shown by the black ($D = 10$ kpc), orange ($D = 11$ kpc), and red ($D = 13$ kpc) curves.

And second, since the distance to CCSN may not be well determined, the comparison of the blue (no decay) and red (100% of ν_2 decay) curves after a certain value of energy, for example ~ 23 MeV for model A and neutrino channel, shows that Earth matter effects are greater in absence of neutrino decay (S1) than for the case of 100% decay (S3).

⁴In this particular case the results are not normalized as it was done with Figs. 4.1, 4.2 and 4.3, we only scale ΔF 's dividing by 10^{10} to get a good visualization.

Earth Matter Effect Detection by a Single Detector

In the previous chapter we presented an analysis of Earth matter effects in terms of Eqs. (4-32) and (4-33), however, unless we have two identical detectors which receive CCSN neutrinos with and without Earth matter effect, this procedure is not experimentally viable. With a single detector, a way of identifying the presence of Earth matter effects in CCSN neutrino fluxes is to observe the modulations that appear in their energy spectra which are caused by the regeneration effects [57]. However, recent studies indicate that these features are expected to be difficult to be observed for a typical CCSN at a distance of ~ 10 kpc because the similarity of average energies and the tendency of neutrino fluxes to equalize in the cooling phase [60].

Supernova neutrinos have only been observed once in history coming from supernova SN 1987A, located at the Large Magallanic Cloud, a dwarf satellite galaxy of the Milky Way. Although a supernova can emit neutrinos of all flavors, those detected in 1987 were electron anti-neutrinos as a consequence of the fact that the cross section used for their detection, i.e. inverse beta decay reaction, is much larger than that for other detection channels. This observation imposed the most stringent bound on the neutrino lifetime. However, due to the limited number of observed events and the uncertainties in the CCSN fluxes, this bound may apply only to one of the neutrino mass eigenstates ν_1 or ν_2 but not to both at the same time. This statistical limitation in the determination of the $\bar{\nu}_e$ spectrum currently allows us to look towards the possibility of invisible $\nu_2(\bar{\nu}_2)$ decay leading to situations where Earth matter effects are observable at a single detector like JUNO [62], Hyper-Kamiokande [63] or DUNE [64].

In this chapter, we quickly describe each of these detectors, focusing on their supernova neutrino detection channels. As well as, we expose the most general aspects of the method that will be used in this work for the identification of Earth effects by using a single detector, which is based on Refs. [57, 203, 60, 61, 197].

5.1

The Jiangmen Underground Neutrino Observatory (JUNO)

JUNO is a multipurpose underground neutrino detector currently under construction in China, in the province Guangdong, close to Jiangmen city [198]. Its main aim is to determine, with $\sim 3\sigma$ or more of significance within six years of operation, the still unknown neutrino mass ordering by measuring very precisely the energy spectrum of nuclear reactor anti-neutrinos from the Yangjiang and Taishan nuclear power plants, both at a distance of ~ 53 km. Since to solve the mass ordering problem it is needed a very good energy resolution, JUNO must reach a energy resolution of $3\%/\sqrt{E(\text{MeV})}$, where E is the prompt energy, see subsection 5.1.1. This resolution is derived from a photoelectron (pe) statistics of at least 1100 pe/MeV. With such energy resolution, JUNO will be able to measure the solar and atmospheric mixing parameters with an accuracy of 1% or better. Among other capabilities, JUNO can detect CCSN neutrinos [62, 199, 200] mainly via the inverse beta decay (IBD) reaction and also by some other channels which give much less relevant contributions for our study. The detector mainly consists of three parts [198]:

1. *The central detector*: It consists of a transparent acrylic sphere with ~ 35.4 m inner diameter and 120 mm in shell thickness, surrounded by a stainless steel support structure of ~ 40 m outer diameter, in which ~ 18000 20" high-quantum efficiency photomultiplier tubes (PMTs) and ~ 26000 3" PMTs will be accommodated [201]. The whole structure of the central detector is immersed in a cylindrical water tank of ~ 44 m of diameter. The acrylic sphere will be filled with 20 kt of liquid scintillator (LSc) made of Linear Alkyl-Benzene (LAB), which serves as target material.
2. *The water Cherenkov detector*: It is a pool filled with ~ 35 kt of ultra-pure water and instrumented with ~ 2000 additional 20" PMTs, which acts as a Cherenkov detector to tag and veto cosmic muons. To archive its goal, JUNO must precisely measure the neutrino spectrum and to look for any distortion in it. Therefore, it is necessary to shield the experiment as much as possible and to take account of any external event that can mimic the signal in the central detector; this task is largely performed by the water Cherenkov detector and the top tracker.
3. *The top tracker*: This muon tracker is located on top of the water Cherenkov detector. Its main function is to independently provide muon information to tag these events and track their trajectories.

We stress that in this work we consider only some main features of the JUNO detector such as its size and its energy resolution, which is sufficient for our purpose.

5.1.1

CCSN neutrino detection in a liquid scintillator detector

A liquid scintillator detector like JUNO provides six detection channels for CCSN neutrinos, three charged current and three neutral current channels. Table 5.1 shows a summary of the detection interactions, which are presented in descending order according to the number of events that each one of them can detect [198].

No.	Type	Channel
1	CC	$\bar{\nu}_e + p \rightarrow e^+ + n$
2	NC	$\nu + p \rightarrow \nu + p$
3	CC + NC	$\nu + e^- \rightarrow \nu + e^-$
4	NC	$\nu + {}^{12}\text{C} \rightarrow \nu + {}^{12}\text{C}^*$
5	CC	$\bar{\nu}_e + {}^{12}\text{C} \rightarrow e^+ + {}^{12}\text{B}$
6	CC	$\nu_e + {}^{12}\text{C} \rightarrow e^- + {}^{12}\text{N}$

Table 5.1: Charged and neutral current detection interactions in JUNO for CCSN neutrinos: (1) IBD, (2) elastic neutrino-proton scattering, (3) elastic neutrino-electron scattering, (4) NC interaction on ${}^{12}\text{C}$, (5) and (6) CC interactions on ${}^{12}\text{C}$.

According to Table 5.1, and hence Ref [198], IBD is the dominant channel of CCSN neutrino detection at JUNO with $\sim \mathcal{O}(10^3)$ events for a galactic supernova at 10 kpc. The elastic scattering of neutrinos on protons is also a relatively large detection channel with the same order in the number of events, but this channel, as well as (3) and (4), would not be sensitive to the Earth matter effect (or any oscillation effect among active neutrino flavors) as they are induced by neutral current reactions common for all flavor. The other CC channels give much less contributions and for simplicity we ignore them.

An electron anti-neutrino interacting in the central detector with a free proton from the target material (Linear Alkyl-Benzene) creates via IBD a positron and a neutron. The positron quickly annihilates with an electron and deposits at the detector an energy composed of the rest and kinetic energy of the positron and the rest energy of the electron, i.e.,

$$E_\nu \equiv E_{e^+} + m_e, \quad (5-1)$$

where E_{e^+} is the positron kinetic energy, m_e is the electron (or positron) rest energy, and E_ν is the so-called visible energy from the reaction (the prompt signal at the detector). The neutron scatters through the detector and is later captured by a hydrogen nucleus producing a photon of 2.2 MeV (the delayed signal at the detector). The coincidence of the positron and neutron signal, in space (few cm) and time ($\sim 250 \mu\text{s}$) is a clear identification of $\bar{\nu}_e$ events. Since the short duration of CCSN neutrino burst ~ 10 s, we can consider the IBD detection as free of background associated with external sources, e.g. reactor neutrinos (~ 0.01 events/10s), geo-neutrinos (~ 0.0002 events/10s) [62].

For the purpose of this thesis we are interested in the energy spectrum rather than the total number of detected events, therefore if we divide in n bins the visible energy interval for CCSN neutrinos, the number of events in the i -th bin is given by

$$(\mathcal{N}_{\bar{\nu}_e})_i = N_T \int_{E_i^{\nu} - \Delta E_i^{\nu}/2}^{E_i^{\nu} + \Delta E_i^{\nu}/2} dE_\nu \int_{E_{\bar{\nu}_e}^{\text{th}}}^{\infty} dE_{\bar{\nu}_e} F_{\bar{\nu}_e}^{\oplus}(E_{\bar{\nu}_e}) \sigma_{\bar{\nu}_e p}(E_{\bar{\nu}_e}) \mathfrak{R}(E_\nu; E_{\bar{\nu}_e}, \delta E_\nu), \quad (5-2)$$

where $F_{\bar{\nu}_e}^{\oplus}$ is the electron anti-neutrino flux at the detector after passing through the Earth matter as given by Eqs. (4-30) and (4-31), $\sigma_{\bar{\nu}_e p}(E_{\bar{\nu}_e})$ is the cross section of the IBD interaction, which is implemented by using the formula found in Ref [202]. This formula gives a very good approximation for the energy range under consideration, less than 100 MeV. According to the JUNO main characteristics described in the previous section, we found that the number of free protons at the detector is $N_T \sim 1.46 \times 10^{33}$. Finally, $E_{\bar{\nu}_e}^{\text{th}} = 1.806$ MeV is the energy threshold of the reaction and $\mathfrak{R}(E_\nu; E_{\bar{\nu}_e}, \delta E_\nu)$ is the normalized Gaussian smearing function which takes into account the photon energy smearing of the detector. We define this function to be:

$$\mathfrak{R}(E_\nu; E_{\bar{\nu}_e}, \delta E_\nu) = \frac{1}{\sqrt{2\pi}\delta E_\nu} \exp \left[-\frac{1}{2} \left(\frac{E_\nu - E_{\bar{\nu}_e} + 0.782 \text{ MeV}}{\delta E_\nu} \right)^2 \right], \quad (5-3)$$

where $\delta E_\nu/\text{MeV} = 3\% \sqrt{E_\nu/\text{MeV}}$ is the energy resolution of the detector.

Since CCSN neutrino energies are a few MeV, the recoil energy of the neutron can be neglected due to the higher neutron mass. Hence, the neutrino energy ($E_{\bar{\nu}_e}$) and the positron energy can be related by $E_{e^+} = E_{\bar{\nu}_e} - (m_n - m_p) \approx E_{\bar{\nu}_e} - 1.293$ MeV and therefore, the visible energy can be approximated to $E_\nu \approx E_{\bar{\nu}_e} - 0.782$ MeV.

5.1.2

Earth matter effects at JUNO

In this section we will present the most general aspects of the method that will be used in this work for the identification of Earth effects by using a single detector. This method is based on the procedure adopted in Ref. [57]. To make this procedure clearer, first let us note that Eq. (4-30b) for the NMO case can be rewritten as follows:

$$F_{\bar{\nu}_e}^{\oplus} \approx c_{12}^2 F_{\bar{\nu}_e}^0 + s_{12}^2 (1 - r_2) F_{\bar{\nu}_x}^0 - \bar{f}_{reg} \left[F_{\bar{\nu}_e}^0 - (1 - r_2) F_{\bar{\nu}_x}^0 \right], \quad (5-4)$$

where the first two terms represent the flux of electron anti-neutrinos at the surface of the Earth; they include resonant flavor transitions in the mantle of the star and $\bar{\nu}_2$ decays on the way to the Earth. While the third term takes into account the interaction of neutrinos with the matter of the Earth.

Now, with the purpose of making explicit the energy dependence of the regeneration factor, let us first consider the simplest case of a constant matter potential¹ in Eq. (3-83). In which case the regeneration factor takes the form

$$\bar{f}_{reg} \approx -\epsilon \sin^2 \theta_{12} \sin^2 \left(\Delta m_{21}^2 \sqrt{1 + 2\epsilon \cos 2\theta + \epsilon^2} L y \right), \quad (5-5)$$

where $y \equiv 12.7/E$ is the inverse energy. Here, the mass squared difference between ν_1 and ν_2 is given in units of 10^{-5} eV^2 , L is given in units of 1000 km and E in units of MeV.

We can observe from Eq. (5-5) that f_{reg} is a periodic function of inverse energy, with a frequency $\omega \approx 2\Delta m_{21}^2 L$. Consequently, $F_{\bar{\nu}_e}^{\oplus}$ is also a periodic function on y . Since the coefficient of f_{reg} and the first two terms in Eq. (5-4) are slowly varying functions of the inverse energy, they contain frequencies much smaller than ω and hence $F_{\bar{\nu}_e}^{\oplus}$ exhibits the same frequency as f_{reg} [57].

This characteristic is also reflected in the spectrum of neutrinos observed at the detector, since $(\mathcal{N}_{\bar{\nu}_e})_i$ depends on $F_{\bar{\nu}_e}^{\oplus}$. In a similar way we can reach the same conclusion in the case of Eq. (4-31b) for IMO. Fig. 5.1 shows us an example of the modulations in the inverse energy spectrum, for a baseline $L = 4000$ km and Model C3 in table 2.3. The blue (NMO) and cyan (IMO) histograms refer specifically to scenario S1 (no decay). The red (NMO) and orange (IMO) histograms refer to scenario S3 (100% decay of $\bar{\nu}_2$). We can clearly note for S3 the presence of modulations which are approximately equally

¹It should be clarified that in general $V(x)$ is not a constant function and that the results that we will present in this chapter and in the next one are made without any approximation, this is by numerically solving Eq. (3-62). Here, a constant density is considered just for mathematical simplicity when presenting the method that we will use to identify the presence of Earth matter effects.

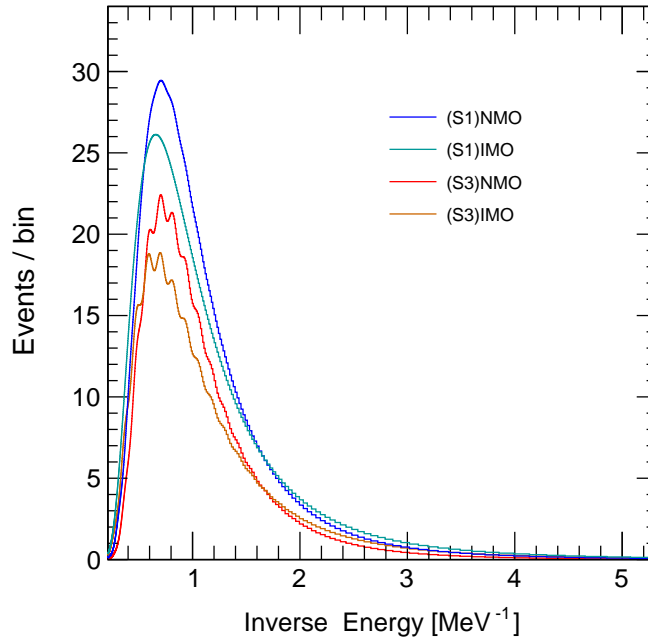


Figure 5.1: Inverse energy distribution of IBD events expected at JUNO for $L = 4000$ km and Model D in table 2.3. The red and black histograms refer specifically to S3 (100% decay of $\bar{\nu}_2$) scenario computed for NMO and IMO, respectively.

spaced.

After observing CCSN neutrinos, the main information that we obtain is the arrival time and the energy of each event, hence their energy spectra. Thus we can take the Fourier transform of the inverse energy spectrum [57, 60, 61] showed in Fig. 5.1 to determine the frequency of the modulations. The observability of a peak in the resulting power spectrum would be a clear sign of the presence of Earth effects. We define the power spectrum of the N detected events as

$$P(\omega) = \left| \frac{1}{\sqrt{N}} \sum_{\text{Energy bin } i} \frac{N_i}{\Delta y_i} \int_{\Delta y_i} dy_i e^{i\omega y_i} \right|^2, \quad (5-6)$$

where Δy_i is the width of the i -th bin and ω is the frequency that characterizes the modulations.

Fig. 5.2 shows some example of Fourier transform of the inverse energy spectrum for two different distances traveled by neutrinos, $L = 8000$ km and $L = 12000$ km. In the former case neutrinos pass through only the Earth's mantle on their way to the detector, that is, they only experience an abrupt change in density (the difference between the vacuum² and mantle densities). According to Eq. (5-5), the modulations in the inverse energy spectrum are characterized by a single frequency and as a consequence only one peak is observed (upper and lower-left panels). In the case of $L = 12000$ km CCSN

²For the purposes of this work we can consider that the Earth atmosphere is vacuum.

neutrinos also cross the Earth's core, then they find two additional jumps in the density corresponding to the differences between the mean densities in the mantle-core and core-mantle boundaries. This multilayer structure of the Earth causes that f_{reg} presents three detectable frequencies in the power spectrum (middle and lower-right panels).

From Fig. 5.2 we can also see how neutrino decay modifies the height and shape of the peaks in the power spectrum. According to the type of neutrino mass ordering, we can classify these effects in two groups:

1. *Pure structures*: In this group we classify the one-peak structures such that the height of the peak is strictly increasing as the percentage of decay increases³. This kind of structures take place for IMO, see for example the lower panels in Fig. 5.2.
2. *Hybrid structures*: Here we classify the structures that present a double-peak formation, which is more accentuated as r_2 increases to a critical value r_2^c , after this the depletion that gives rise the double-peak is regenerated as the percentage of neutrino decay increases, then it forms an single-peak structure whose height, depending on the supernova model being considered and the proximity of the supernova to the Earth, may be greater than the height of the peak corresponding to scenario S1. See for example the NMO scenarios in Fig. 5.2. Upper- and middle-left panels show the behavior of the peak before r_2^c , while the upper- and middle-right panels show such behavior just after passing r_2^c .

Heretofore we have not taken into account the finite nature of the number of detected events. A finite statistics leads to a background for the peaks in the power spectrum and consequently makes it difficult to observe the Earth matter effects [57, 203, 205, 60, 61]. Since we are only working with the main characteristics of each detector, in this thesis we only take into count 1σ Poisson fluctuations at the event number determination and ignore any systematic uncertainties of the detectors. Figs. 5.3 for NMO and 5.4 for IMO show the effect that the finiteness of the data has on the observability of the peak associated with the effects of the Earth. The blue, green and red dotted curves correspond to the average power spectrum over 1000 MC (Monte Carlo) run samples for the scenarios S1, S2 and S3, respectively. While the error bars represent the uncertainty at 1σ in the measurement of each point.

³Only for the results shown in Fig. 5.2 (and also in Figs. 5.5 and 5.8), for simplicity, we compute CCSN neutrino fluxes by setting r_2 as energy independent constant in Eqs. (4-28) and (4-29), unlike the one shown in Eq. (4-27).

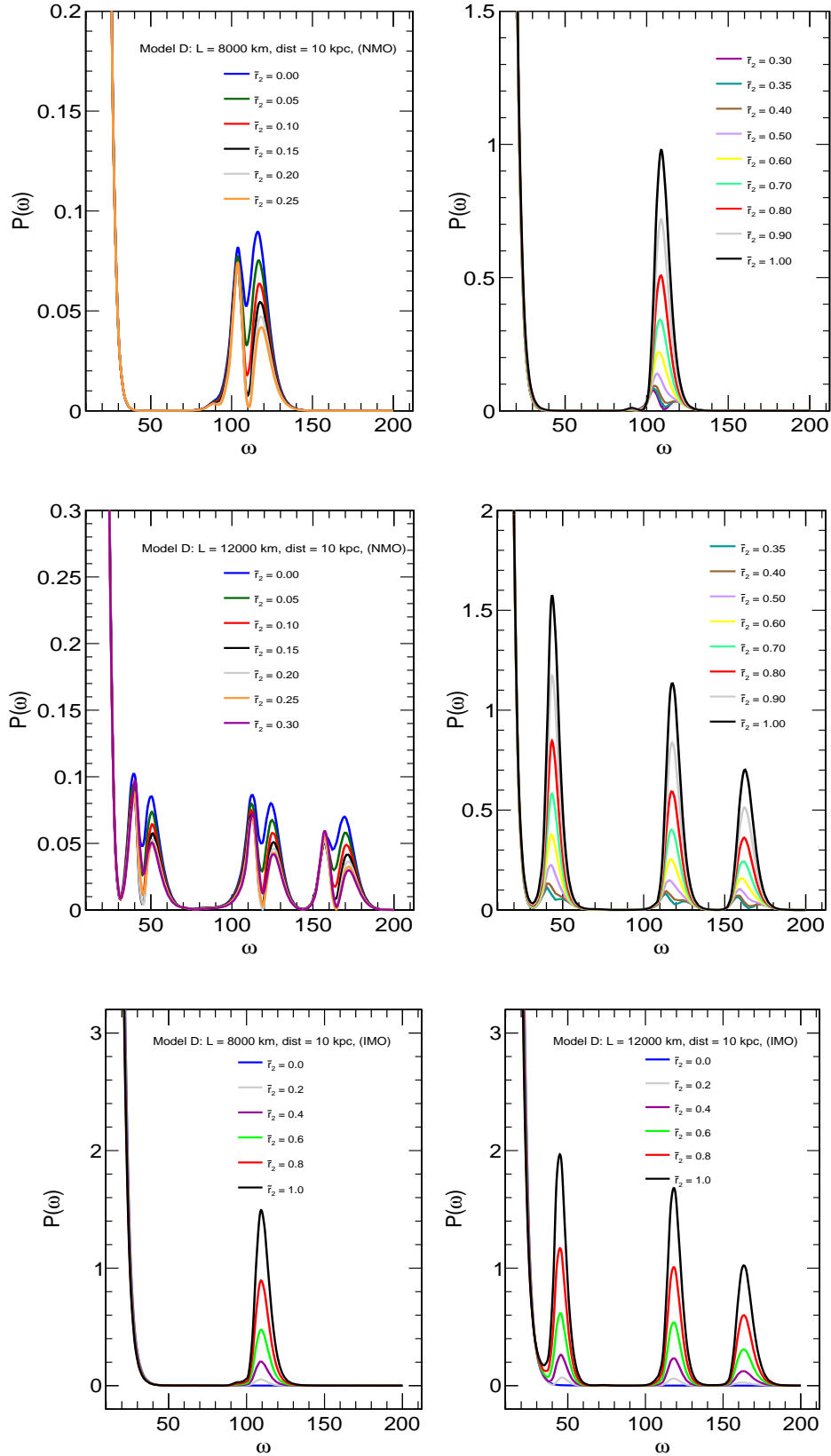


Figure 5.2: (JUNO) Fourier transform of the inverse energy spectrum for two different distances traveled by neutrinos, $L = 8000$ km (upper and lower-left panels) and $L = 12000$ km (middle and lower-right panels) for NMO (upper and middle panels) and IMO (lower panels).

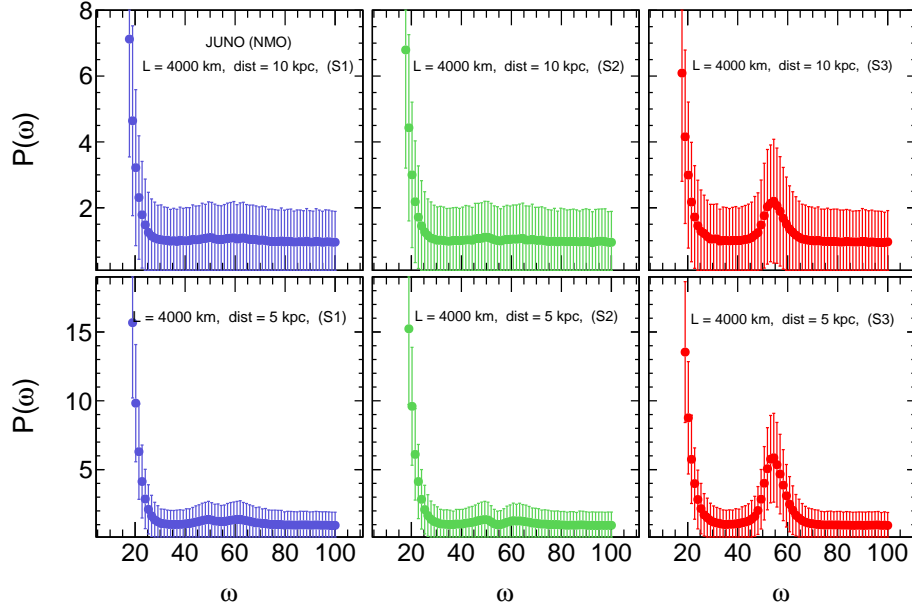


Figure 5.3: (JUNO) Averaged power spectrum over 1000 Monte Carlo run samples for $L = 4000$ km, model D in table 2.3 and NMO. We present these results for the typical CCSN distance of 10 kpc (upper panels) and for a distance of 5 kpc (lower panels), for the three scenarios, S1, S2 and S3 described in the subsection 4.3. We considered the standard deviation given in each fit (vertical error bars) as error in the measurement.

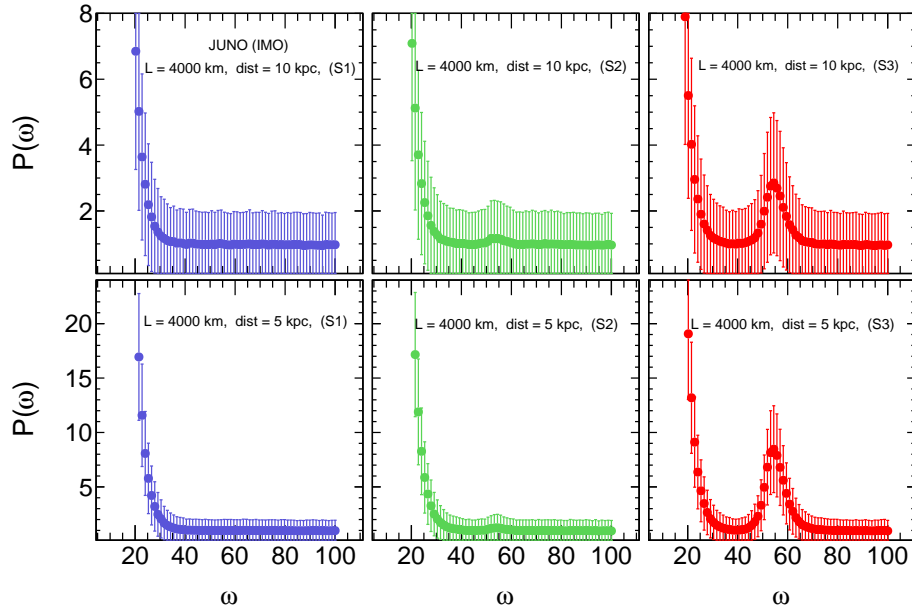


Figure 5.4: Same as in Fig. 5.3 but for IMO.

According to Figs. 5.3 and 5.4 we can draw the following conclusions: IMO provides better opportunities for observing Earth matter effects than

NMO. The decay scenario S2 ($\sim 50\%$ decay) is very similar in effects to S1 (no decay). We think that it is due to the presence of hybrid structures in the power spectrum.

Note that S2 has just passed r_2^c (purple curve in the upper right panel of Fig. 5.2), therefore the heights of the peaks are comparable in both scenarios. Since the expected value for the background fluctuations is ~ 1 [57] (see the scenario S1 in Fig. 5.3), the scenarios S1 (for NMO) and S2 (for both mass orderings) are not appropriate for Earth matter effects observation. At 1σ C.L., the peak in the power spectrum is comparable to or shadowed by the background fluctuations, even for a CCSN at 5 kpc.

5.2

Hyper-Kamiokande

The Hyper-Kamiokande (or Hyper-K) experiment is a water Cherenkov detector that at the same time is a microscope and a telescope that will be used to study elementary particles, the Sun and supernovae by using neutrinos. It is currently under construction (cavern-excavation phase, with the data taking scheduled to start in 2027) in the Kamioka mine, Hida city, Gifu prefecture, Japan [63].

This underground neutrino experiment has an extensive research program aimed at answering some of the most important questions in elementary particle physics, among them the matter-antimatter asymmetry in the Universe, the stability of the proton and the neutrino mass ordering, whose determination increases the precision of CP violation measurements and helps to elucidate the nature of neutrinos, i.e. Dirac or Majorana [63]. According to the standard model of elementary particles, protons are stable particles because of the baryon number conservation. Nevertheless, some grand unified theories (beyond the standard model) violate baryon number conservation and then protons can decay. Additionally, CCSN neutrino observation at Hyper-K will allow us to better understand the explosion mechanism of stars more massive than $\sim 8M_\odot$. Due to its large volume, Hyper-K has an unprecedented capability for observing CCSN neutrinos beyond our galaxy, for example, $\mathcal{O}(10)$ events will be obtained for a supernova in the Andromeda galaxy (i.e. 780 kpc from us) [206].

The detector consist of one cylindrical tank with 71 m height, 68 m in diameter and 40% photo-coverage [206]. It is optically separated into an outer detector with a width of 2 m at the top and bottom or 1 m at the sides, whose

objective is to help distinguish the neutrino signal from the background due mainly to cosmic muons [207], and a 217 kton cylindrical inner detector. Hyper-K is designed to employ the new 50 cm PMTs which have a better timing resolution of 2.6 ns and twice the photon detection efficiency than Super-Kamiokande (Super-K) PMTs. Hyper-K has a possibility to have a second tank in South Korea with the same characteristics as the first [208] but this is still under discussion.

5.2.1

CCSN neutrino detection in a water Cherenkov detector

A water Cherenkov detector like Hyper-K provides mainly three charged current detection channels (IBD and absorption processes on oxygen) and the charged and neutral current neutrino-electron elastic scattering detection channel for CCSN neutrinos. Table 5.2 shows a summary of the detection interactions, which are presented in descending order according to the number of events that each one of them can detect [63].

No.	Type	Channel
1	CC	$\bar{\nu}_e + p \rightarrow e^+ + n$
2	CC + NC	$\nu + e^- \rightarrow \nu + e^-$
3	CC	$\bar{\nu}_e + {}^{16}\text{O} \rightarrow e^+ + {}^{16}\text{N}^*$
4	CC	$\nu_e + {}^{16}\text{O} \rightarrow e^- + {}^{16}\text{F}^*$

Table 5.2: Charged and neutral current detection interactions in Hyper-K for CCSN neutrinos: (1) IBD, (2) elastic neutrino-electron scattering, (3) $\bar{\nu}_e$ ${}^{16}\text{O}$ CC interaction, and (4) ν_e ${}^{16}\text{O}$ CC interaction.

From Table 5.2 we can see that IBD is the main interaction channel for CCSN neutrinos, $\mathcal{O}(10^4)$ events for a galactic supernova at 10 kpc. It is responsible for $\sim 90\%$ of events, making Hyper-K most sensitive to $\bar{\nu}_e$. The elastic scattering of neutrinos on electrons is also a relatively large detection channel with $\mathcal{O}(10^3)$ events [63], but this channel would not be sensitive to the Earth matter effects because they are induced by neutral current reactions common for all flavor (except for $\nu_e(\bar{\nu}_e)$ which can also interact via CC). The other CC channels are subdominants and for simplicity we ignore them.

Water Cherenkov detectors use the IBD reaction on hydrogen nuclei to detect $\bar{\nu}_e$'s. In the case of CCSN neutrinos whose energies are between 5 MeV and 50 MeV, the positron created in the IBD reaction is highly relativistic $\beta \sim 1$, then its speed is higher than the speed of light in water $c_{H_2O} = c/n$,

where $n = 1.34$ is the refractive index of pure water. Therefore it will emit Cherenkov light within an angle $\theta \approx \cos^{-1}(1/n\beta) \approx 42^\circ$. Since Hyper-K could detect multiple photons from each IBD event, this will produce an identifiable circle of hits in the PMTs (ring-imaging technique), which will allow us an accurate reconstruction of events with neutrino energies as low as 5 MeV [63].

In this work we consider only the tank in Japan, currently under construction, with a fiducial mass of 220 kt [63] since for CCSN neutrinos we can use both the inner and outer detectors. As commented before, Hyper-K will have ~ 2 times better photon detection efficiency than its predecessor Super-K, then the energy resolution of Hyper-K is expected to be $\sim \sqrt{2}$ times better than that for Super-K assuming the same photo-coverage. Therefore, since Super-K's energy resolution is 14.2% at $E_\nu = 10$ MeV [209], we calculate the number of IBD events by using Eqs. (5-2) and (5-3) but with $\delta E_\nu/\text{MeV} = 32\% \sqrt{E_\nu/\text{MeV}}$.

5.2.2

Earth matter effects at Hyper-K

Fig. 5.5 shows the Fourier transform of the inverse energy spectrum for Model D in Table 2.3. We present the results for two different distances traveled by neutrinos, $L = 8000$ km and $L = 12000$ km. From this figure we can observe that

1. Like JUNO we have the presence of pure and hybrid structures.
2. Due to its limited energy resolution, Hyper-K cannot resolve the second and third peaks in the power spectrum. Which are expected to $\omega \approx 120$ and $\omega \approx 160$, respectively.
3. For NMO, $\bar{\nu}_2$ decay worsens the observability of Earth matter effects, for neutrinos with $L = 8000$ km, see the upper panels. It should be noted that according to Fig. 5 of Ref. [203], neutrinos that only pass through the mantle have little chance of making Earth effects observable, maybe except for $L = (5000 \pm 1000)$ km.
4. In this particular example, when $\bar{\nu}_2$ decay rate is approximately 80%, the observation of the first peak around $\omega \sim 40$ has a greater chance than in the case of no decay. While $r_2 \geq 0.9$ makes Hyper-K unable to observe that peak.
5. Finally, for IMO we note that $\bar{\nu}_2$ decay always leads to scenarios with a greater chance of observing Earth matter effects.

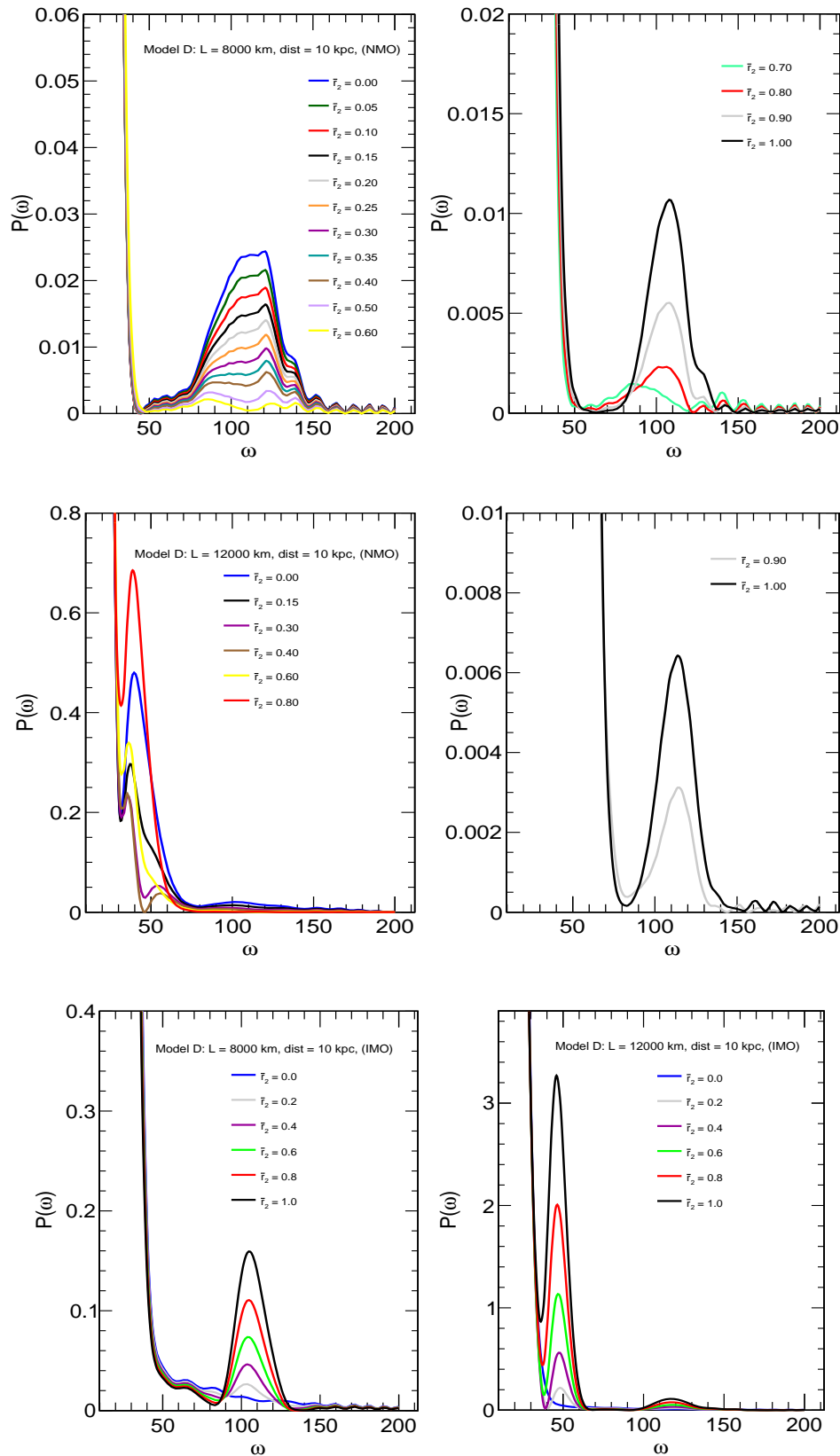


Figure 5.5: (Hyper-K) Fourier transform of the inverse energy spectrum for two different distances traveled by neutrinos, $L = 8000$ km (upper and lower-left panels) and $L = 12000$ km (middle and lower-right panels) for NMO (upper and middle panels) and IMO (lower panels).

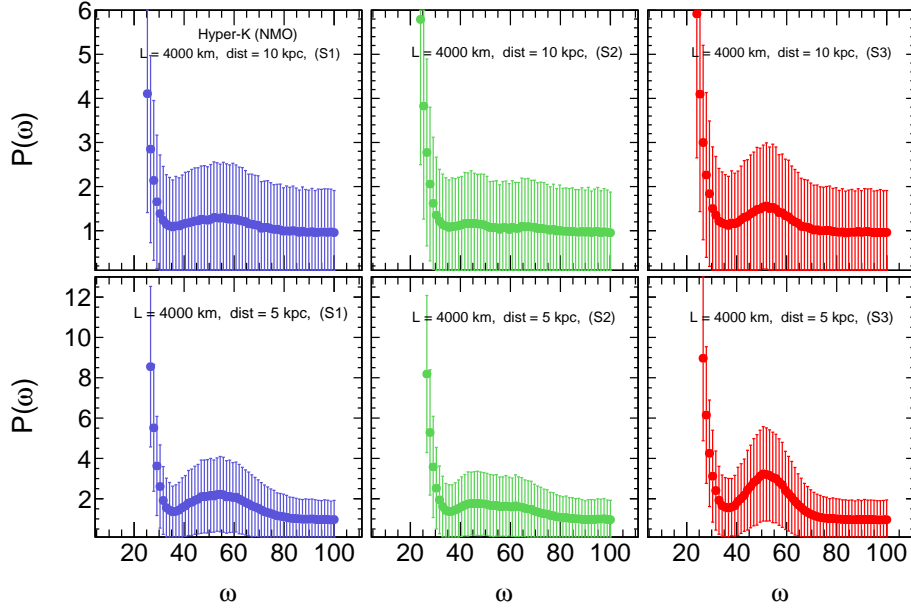


Figure 5.6: (Hyper-K) Averaged power spectrum over 1000 Monte Carlo run samples for $L = 4000$ km, model D in table 2.3 and NMO. We present these results for the typical CCSN distance of 10 kpc (upper panels) and for a distance of 5 kpc (lower panels), for the three scenarios, S1, S2 and S3 described in the subsection 4.3. We considered the standard deviation given in each fit (vertical error bars) as error in the measurement.

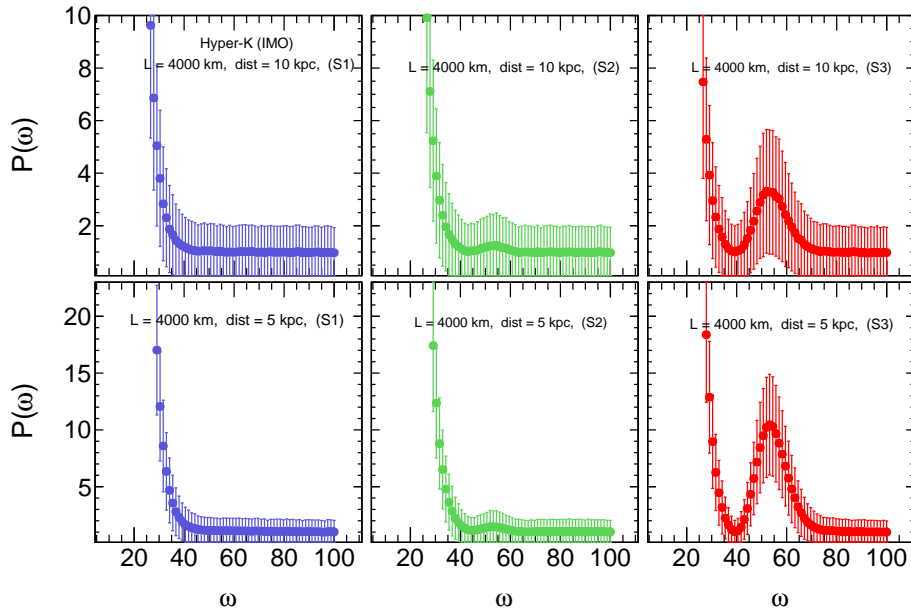


Figure 5.7: Same as in Fig. 5.6 but for IMO.

Figs. 5.6 for NMO and 5.7 for IMO show the averaged power spectrum over 1000 MC (Monte Carlo) run samples for $L = 4000$ km, model D in

table 2.3. We present these results for the CCSN distance of 10 kpc (upper panels) and 5 kpc (lower panels), for the three scenarios, S1, S2 and S3 described in the subsection 4.3. First of all we note that like JUNO the decay scenario S2 ($\sim 50\%$ decay) is very similar in effects to S1 (no decay), except for IMO, for which there are no Earth matter effects in the S1 scenario.

We can also observe that for distances less than 10 kpc (typical distance of a galactic supernovae) there is a greater possibility of observing a peak in the power spectrum, with better conditions for IMO in which case there is also the possibility of observing such a peak for CCSNe 10 kpc away. Unfortunately the conditions are not so favorable for the case of NMO, where it is not possible to observe such a peak for a distance of 10 kpc, since the signal is comparable to the statistical background.

5.3

The Deep Underground Neutrino Experiment (DUNE)

DUNE is a dual-site international experiment for neutrino research and proton decay studies [210, 64]. DUNE's main physics program includes refining the measurement of mixing parameters with a view to determining neutrino mass ordering and the value of CP violation phase, which could provide the answer to the asymmetry of matter-antimatter observed in the Universe. Another goal of DUNE is to look for traces of proton decay. Search for these decays at DUNE can help set limits for unification theories. DUNE's observation of CCSN neutrinos in our galaxy will allow us to learn more about the explosion mechanism of a supernova, as well as obtain first-hand information on its stellar remnants (maybe witness the birth of a black hole).

The experiment will consist of two neutrino detectors: a near detector (DUNE-ND) placed at the Fermi National Accelerator Laboratory (FERMI-LAB) in Batavia, Illinois. And a far detector (DUNE-FD) installed at the Sanford Underground Research Facility (SURF) in Lead, South Dakota.

The DUNE-ND aims to reduce the systematic uncertainties in extracting the oscillation signal at the DUNE-FD which enrich the potential of DUNE [211] for discovering CP violation. This detector consists of three primary components: (1) a Liquid Argon Time-Projection Chamber (LArTPC) called ArgonCube. (2) a high-pressure gaseous argon Time-Projection Chamber (HPgTPC). And (3) an on-axis beam monitor called System for on-Axis Neutrino Detection (SAND).

The DUNE-FD [210, 64, 212] will be a modular LArTPC located 1.5 km

below the SURF, with a total mass 70 kt of liquid argon of which 40 kt will be fiducial mass (in total there will be four LArTPCs with 10 kt each). We will use this detector in our work.

5.3.1

CCSN neutrino detection in a liquid argon detector

Table 5.3 shows a summary of the detection channels for CCSN neutrinos in a LArTPC detector, which are presented in descending order according to the number of events that each one of them can detect [213, 214].

No.	Type	Channel
1	CC	$\nu_e + {}^{40}\text{Ar} \rightarrow {}^{40}\text{K}^* + e^-$
2	CC + NC	$\nu + e^- \rightarrow \nu + e^-$
3	NC	$\nu + {}^{40}\text{Ar} \rightarrow \nu + {}^{40}\text{Ar}^*$
4	CC	$\bar{\nu}_e + {}^{40}\text{Ar} \rightarrow {}^{40}\text{Cl}^* + e^+$

Table 5.3: Charged and neutral current detection interactions in DUNE for CCSN neutrinos: (1) ν_e ${}^{40}\text{Ar}$ CC interaction, (2) elastic neutrino-electron scattering, (3) ν ${}^{40}\text{Ar}$ NC interaction, and (4) $\bar{\nu}_e$ ${}^{40}\text{Ar}$ CC interaction.

DUNE-FD will have high sensitivity to electron neutrino via the ν_e ${}^{40}\text{Ar}$ CC processes (dominant interaction) for which the observables are the electron and the cascade of de-excitation γ -products from K^* [215]. At the far detector, electrons are drifted by electric fields and the signals are collected on wire planes; using the arrival time of these particles, it is possible to reconstruct the three-dimensional tracks. On the other hand, argon can scintillate, and the light can be measured by solid state silicon photomultipliers (SiPMs), allowing a fast synchronization of the signals and improving the location of events within the detector [216, 210, 212]. This channel provides a unique opportunity to observe the neutronization burst, primarily composed of ν_e . In this work we use the cross section for the most relevant CCSN neutrino interaction in argon (channel 1 in Table 5.3) found in the SNOwGLOBES software package [217] and the energy resolution that has been calculated by the ICARUS collaboration [213] $\delta E_\nu/\text{MeV} = 0.11 \sqrt{E_\nu/\text{MeV}} + 0.02(E/\text{MeV})$ which is better than the one that Hyper-K would have.

5.3.2

Earth matter effects at DUNE

Figs. 5.8 shows an example of Fourier transform of the inverse energy spectrum for two different distances traveled by neutrinos, $L = 8000$ km (upper panels) and $L = 12000$ km (lower panels) for NMO (left panels) and IMO (right panels).

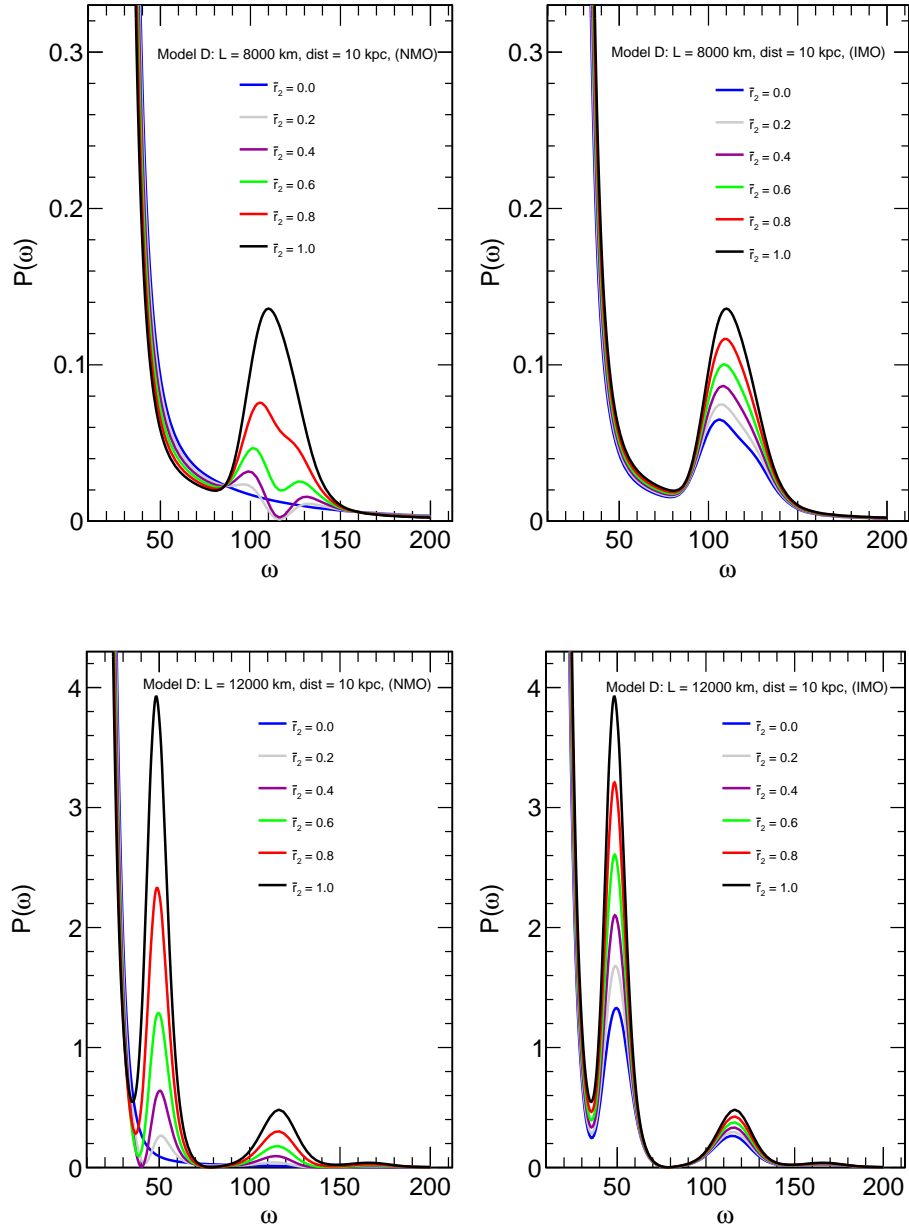


Figure 5.8: (DUNE) Fourier transform of the inverse energy spectrum for two different distances traveled by neutrinos, $L = 8000$ km (upper panels) and $L = 12000$ km (lower panels) for NMO (left panels) and IMO (right panels).

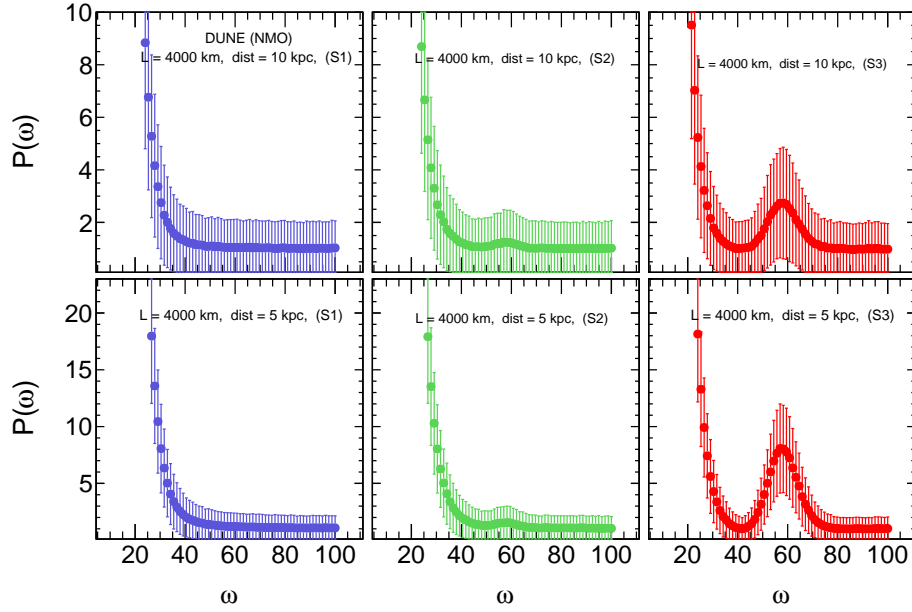


Figure 5.9: (DUNE) Averaged power spectrum over 1000 Monte Carlo run samples for $L = 4000$ km, model D in table 2.3 and NMO. We present these results for the typical CCSN distance of 10 kpc (upper panels) and for a distance of 5 kpc (lower panels), for the three scenarios, S1, S2 and S3 described in the subsection 4.3. We considered the standard deviation given in each fit (vertical error bars) as error in the measurement.

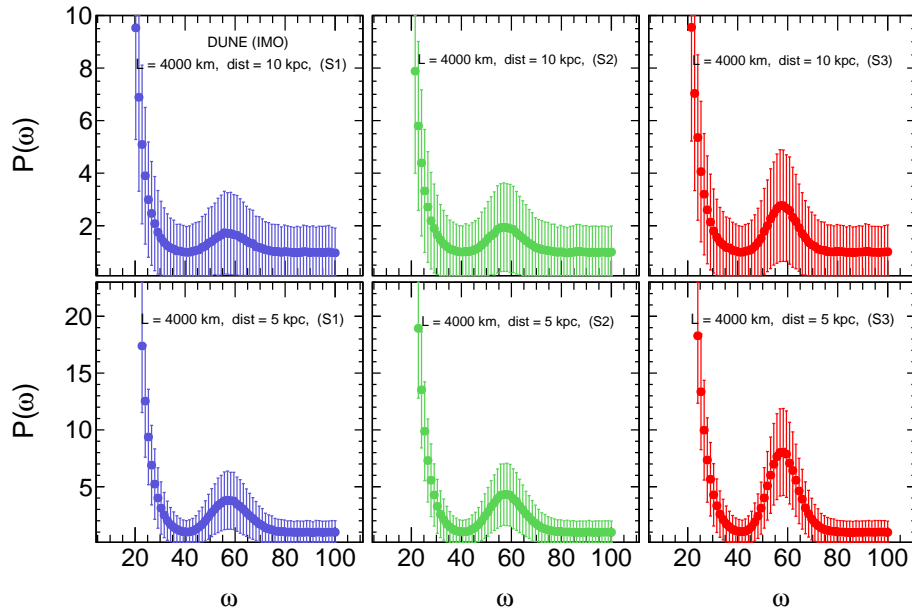


Figure 5.10: Same as in Fig. 5.9 but for IMO.

As opposed to JUNO and Hyper-K we can observe a tendency to form pure structures for both mass ordering, except for $L = 8000$ km (NMO). This

increases the possibilities of observing the peaks associated with Earth effects, especially when neutrino decay is present.

It should be noted that due to its energy resolution DUNE-FD can observe only two peaks (at $\omega \approx 50$ and $\omega \approx 120$) when neutrinos cross the Earth's core. This result is better with respect to Hyper-K but unfavorable in relation to JUNO.

In Figs. 5.9 for NMO and 5.10 for IMO we show an example of averaged power spectrum over 1000 MC (Monte Carlo) run samples for $L = 4000$ km and the model D in table 2.3. similar to the examples presented for JUNO and Hyper-K. We can notice that for a supernova in our galaxy at 10 kpc away, there is a little chance of observing a peak in the power spectrum in the case of 100% of neutrino decay. The other neutrino decay scenarios remain unfavorable unless the supernova distance is less than 10 kpc and the mass ordering inverted.

Sensitivity of the next-generation of neutrino detectors to Earth Matter Effects

In this chapter we study the sensitivity of JUNO, Hyper-K and DUNE to the detection of Earth matter effects via Fourier transform of the inverse-energy spectrum of CCSN neutrinos. Hereafter, we will focus on S3, because is a good prospect for an unambiguous identification of such effects. Therefore, as a starting point for this purpose let us note that to obtain the power spectrum shown for example in Figs. 5.9 and 5.10, we averaged 1000 MC run samples, where each one of them represents the Fourier transform that we would obtain when analyzing the neutrino energy spectrum from a single CCSN explosion.

Once each of these power spectra is obtained, we can use the area (A) under the peak (s) that they exhibit as a partial measurement of the presence of Earth effects in the neutrino energy spectrum. This calculation is made between two fixed frequencies ω_{min} and ω_{max} as performed in Ref. [203]. We have used the word partial when referring to this measure because $A \neq 0$ by itself cannot be considered as proof of the existence of Earth effects due to the limited number of events (statistical errors). For this reason, in addition of calculating this area, we must compare it with the area obtained when only background fluctuations are present.

This gives rise to two distributions: the *signal* obtained from the areas calculated taken into account the regeneration factors and the *background* corresponding to the areas calculated in the absence of the regeneration factors. Fig. 6.1 shows an example of these area distributions (signal in red and background in black) for neutrinos coming from a CCSN at 10 kpc away (model D in Table 2.3), for two baselines: $L = 4000$ km and $L = 12000$ km.

We decided to accept the observation of Earth effects at a confidence level (C.L.) $1 - \alpha$ if the observation, A , is greater than a critical value A_c^α known as detection condition [203] (lower limit of the hatched region in Fig. 6.1). Here α is the probability of false alarm which will be defined in section 6.2 in the context of the signal detection theory [204].

In this thesis we use two statistical tools which help us to have a better

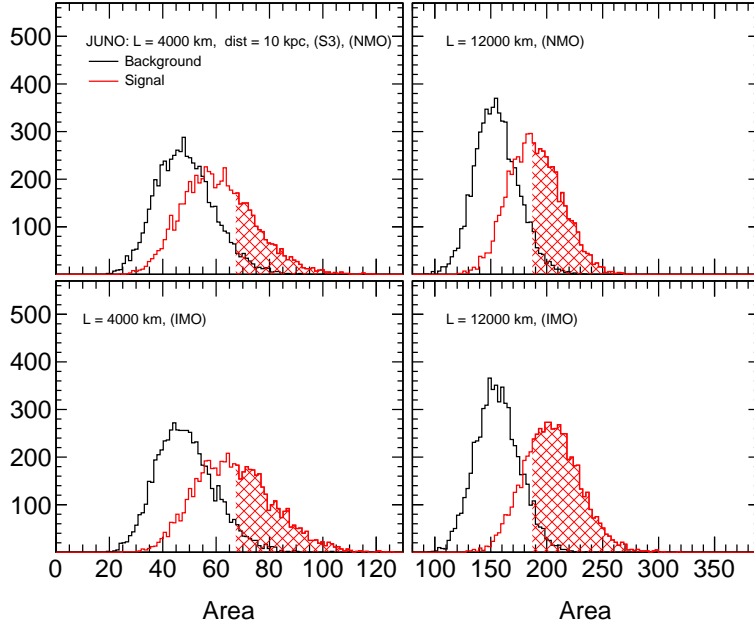


Figure 6.1: Background fluctuations (black) and signal (red) area distributions. The background distribution was calculated in the absence of the Earth matter effects whereas the signal distribution was calculated in the presence of the Earth matter effects. We show these distributions for JUNO for the both mass orderings: NMO (upper panels) and IMO (lower panels). The hatched region correspond to a confidence level of 2σ (95.45%).

idea of how possible it is to observe Earth matter effects at a certain level of confidence. These are the Earth matter observation probability and the sensitivity parameter d' . We start by defining the latter.

6.1

Sensitivity parameter d'

The parameter d' describes the relationship of signal and background fluctuations distributions to each other. When d' is close to zero, the distributions are completely overlapping which means that there is no way to distinguish between signal and background fluctuations. In contrast, when d' is large, the two distributions are widely separated. Therefore d' measure the sensitivity with which the Earth matter effects can be detected. Mathematically this statistic can approximately be written as

$$d' = \frac{\mu_s - \mu_b}{\sqrt{\frac{1}{2}(\sigma_s^2 + \sigma_b^2)}}, \quad (6-1)$$

where μ_s and μ_b are the means of the signal and background fluctuation distributions and σ_s and σ_b their standard deviations, respectively. So, roughly speaking, d' is the distance between the means of the two distributions shown

in Fig. 6.1 (red and black histograms). We can see by comparing the left and right panels of this figure that this parameter has a higher value when neutrinos cross the Earth's core than when they cross only the mantle. On the other hand, Fig. 6.1 also shows that for inverted mass ordering there is a better sensitivity to discriminate between signal and background fluctuations.

Fig. 6.2 shows the sensitivity to Earth matter effects detection in the presence of invisible neutrino decay for JUNO (upper panel), Hyper-K (middle panel) and DUNE (lower panel) as a function of r_2 , the decay rate of ν_2 . For the sake of simplicity, we treated r_i as constant which does not depend on neutrino energy unlike the one shown in Eq. (4-27). To be more correct, the sensitivity detection should have been computed and shown as a function of $\langle r_i \rangle$, which is the averaged value of r_i over neutrino energy but for the illustrative purpose we approximate it as constant. Furthermore, these results are presented for the special case of a supernova 10 kpc away. This is because at that distance the probability of a CCSN occurring in our galaxy is higher. From this figure we can observe that

1. There is a very marked difference between the neutrino and anti-neutrino detection channels.
2. In the case of JUNO or Hyper-K, the sensitivity parameter behaves differently for NMO than for IMO.

Let us see for example that in the case of JUNO the solid curves (NMO) decrease as r_2 increases, they reach a minimum around $r_2 \sim 0.3$ for $L = 4000$ km or $L = 8000$ km and $r_2 \sim 0.4$ for $L = 12000$ km, and then they become increasing functions of the decay parameter. On the other hand, the dashed curves (IMO) are strictly increasing functions for all possible values of r_2 . In the case of Hyper-K, the minimum is shifted to the right for $L = 4000$ km and its concavity is more pronounced, while for $L = 8000$ km and $L = 12000$ km the concavity is very small or almost nonexistent. We think that in part this is due to the energy resolution of the detector. We can try to understand qualitatively such a difference of behaviors of the sensitivity between NMO and IMO found in the upper and middle panels of Fig. 6.2 as follows.

According to the lower left panels of Figs. 4.1-4.3 corresponding to NMO for the antineutrino channel, $\Delta F_{\bar{\nu}_e}$ is negative in the relevant neutrino energy range of $\gtrsim 20$ MeV for S1 (no decay), whereas for the scenarios of larger decay rates, S2 and S3, $\Delta F_{\bar{\nu}_e}$ is mostly positive for all the energy range. This implies that when the decay rate increases from 0 to 100%, $\Delta F_{\bar{\nu}_e} = \bar{f}_{\text{reg}}[(1-r_2)F_{\bar{\nu}_x}^0 - F_{\bar{\nu}_e}^0]$ around the relevant energy range changes its sign. Then the Earth matter

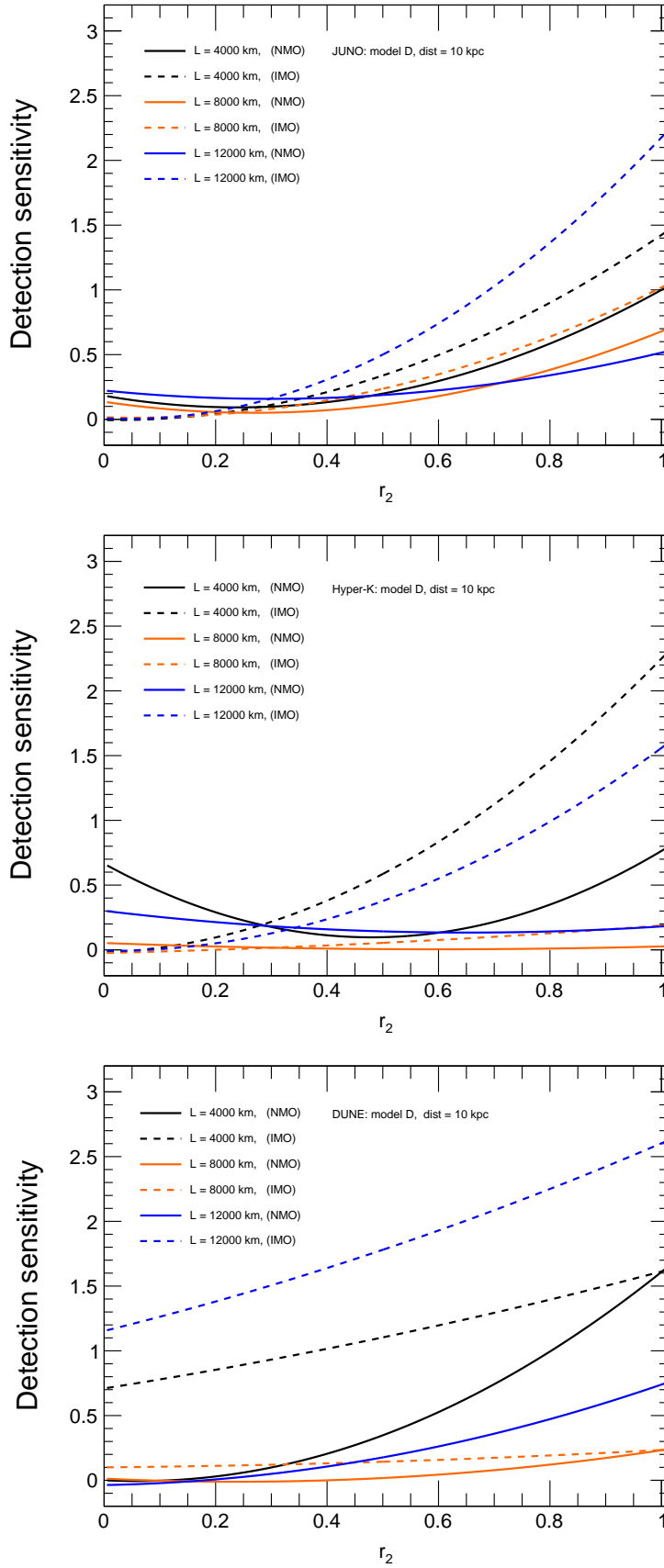


Figure 6.2: Sensitivity to Earth matter effects detection in presence of invisible neutrino decay for JUNO (upper panel), Hyper-K (middle panel) and DUNE (lower panel) as a function of the ν_2 decay rate r_2 .

effects are practically non-existent near the point where $\Delta F_{\bar{\nu}_e}$ changes its sign, which correspond to the peak of the events (see Fig. 5.1, $\sim 12.7/0.65$ MeV), and therefore, we expect worst detection sensitivity around such a point. On the other hand, if we look at the lower right panels of Figs. 4.1-4.3 corresponding to IMO, we can see that $\Delta F_{\bar{\nu}_e}$ is nearly always positive for all the energy range, increasing monotonically as the decay rate increases.

We can also try to understand the behavior of the sensitivity curves for NMO by means of Figs. 5.2 and 5.5. For example, in the case of JUNO, the presence of double-peak structures for $r_2 \lesssim 0.2$ (upper left panel of Figs. 5.2) leads to a lower value for the mean of the signal, consequently the distance between the two distributions, signal and background, becomes smaller, causing a lower value of the sensitivity parameter. While for $r_2 > 0.2$, the predominant presence of a single-peak structure makes d' a strictly increasing function in this range. The suppression in the intensity of the peaks due to these double-peak structures seems to have its origin in the partial destructive interference presented by the different components of the power spectrum [60].

Now in the case of DUNE (lower panel of Fig. 6.2), from the upper panels of Figs. 4.1-4.3 corresponding to the neutrino channel we can see that as the decay parameter varies from 0 to 1, within the relevant neutrino energy range of $\gtrsim 15$ MeV, the possibility of observing Earth matter effects increases. In particular, for NMO, we can also understand analytically that the sensitivity should be an increasing function of r_2 as $\Delta F_{\nu_e} \simeq -f_{\text{reg}} r_2 F_{\nu_x}^0$ (see Eq. (4-32)).

Finally, in agreement with Fig. 6.2 we stand out the following results:

1. This figure can help us to understand why decay scenarios such as the scenario S2 for NMO ($< 70\%$ of $\bar{\nu}_2$ decay) does not enhance the impact on Earth effect identification when compared to S1.
2. For NMO, when $r_2 \gtrsim 0.4$ (40% of ν_2 decay) JUNO has better sensitivity to Earth matter effects detection than the other detectors.
3. For IMO, Hyper-K has better sensitivity to Earth matter effects detection than JUNO in the particular case of CCSN neutrinos with a baseline $L = 4000$ km. While for $L = 8000$ km and $L = 12000$ km the JUNO's sensitivity is better than that of Hyper-K.
4. For IMO, DUNE has better sensitivity to Earth matter effects detection than the other detectors when $r_2 \lesssim 0.8$ (for $L = 4000$ km), $r_2 \lesssim 0.4$ (for $L = 8000$ km) and for the full range of r_2 in the case of $L = 12000$ km.

6.2

Detection probability of Earth matter effects

The second statistic that we use in this work is the signal detection probability which is very common when we have to make decisions that they are in some way uncertain or ambiguous. We define this probability ($p = 1 - \beta$) as the fraction of the area of the signal distribution [203], above A_c^α ; red hatched region in Fig. 6.1. Here β corresponds to the probability of making an error type-II, that is, considering as background fluctuations the signal below the detection criterion.

To describe the accuracy of the presence or absence of Earth matter effects in future CCSN neutrino fluxes, it is also necessary to take into account that we can confuse the background with the signal, that is, we can think that we are observing a signal when it is actually background. This possibility defines the so-called probability of false alarm, α , that according to Fig. 6.1 α corresponds to the fraction of the area of the background distribution above the decision criterion. It is very common to give this probability in terms of a certain number of double-sided Gaussian standard deviations. In this work, we identify a particular value of A as a signal if and only if, it is located at a distance greater than $n\sigma$ away from the background mean. The relationship between $n\sigma$ and α can be written as

$$\alpha(n) = \frac{2}{\sqrt{2\pi}} \int_n^\infty dx e^{-x^2/2} = \operatorname{erfc}\left(\frac{n}{\sqrt{2}}\right), \quad (6-2)$$

where $\operatorname{erfc}(x)$ is the complementary error function. With this definition we can identify 1σ , 2σ and 3σ with a confidence level of 68.27%, 95.45% and 99.73%, respectively [62, 218, 219].

In order to give an example of this definition, we present below the detection probability of the Earth matter effects as a function of the distance to the supernova, for two sets of CCSN models: $\{B, C_2, D\}$ and $\{A, C_3, D\}$. The first set includes only models for the accretion phase while the second is mixed. Figs. 6.3 and 6.4 show this probability, respectively for $\{B, C_2, D\}$ and $\{A, C_3, D\}$, at 2σ (95.45% C.L.) for JUNO (upper panel), Hyper-K (middle panel) and DUNE (lower panel), for NMO (upper panel of each subfigure) and IMO (lower panel of each subfigure).

From these figures we can draw out the following observations:

1. Despite the fact that this statistic is model dependent (it depends on the CCSN parameters), we can see that in general it reflects the positive impact that ν_2 decay has on the observation of the Earth matter effects.

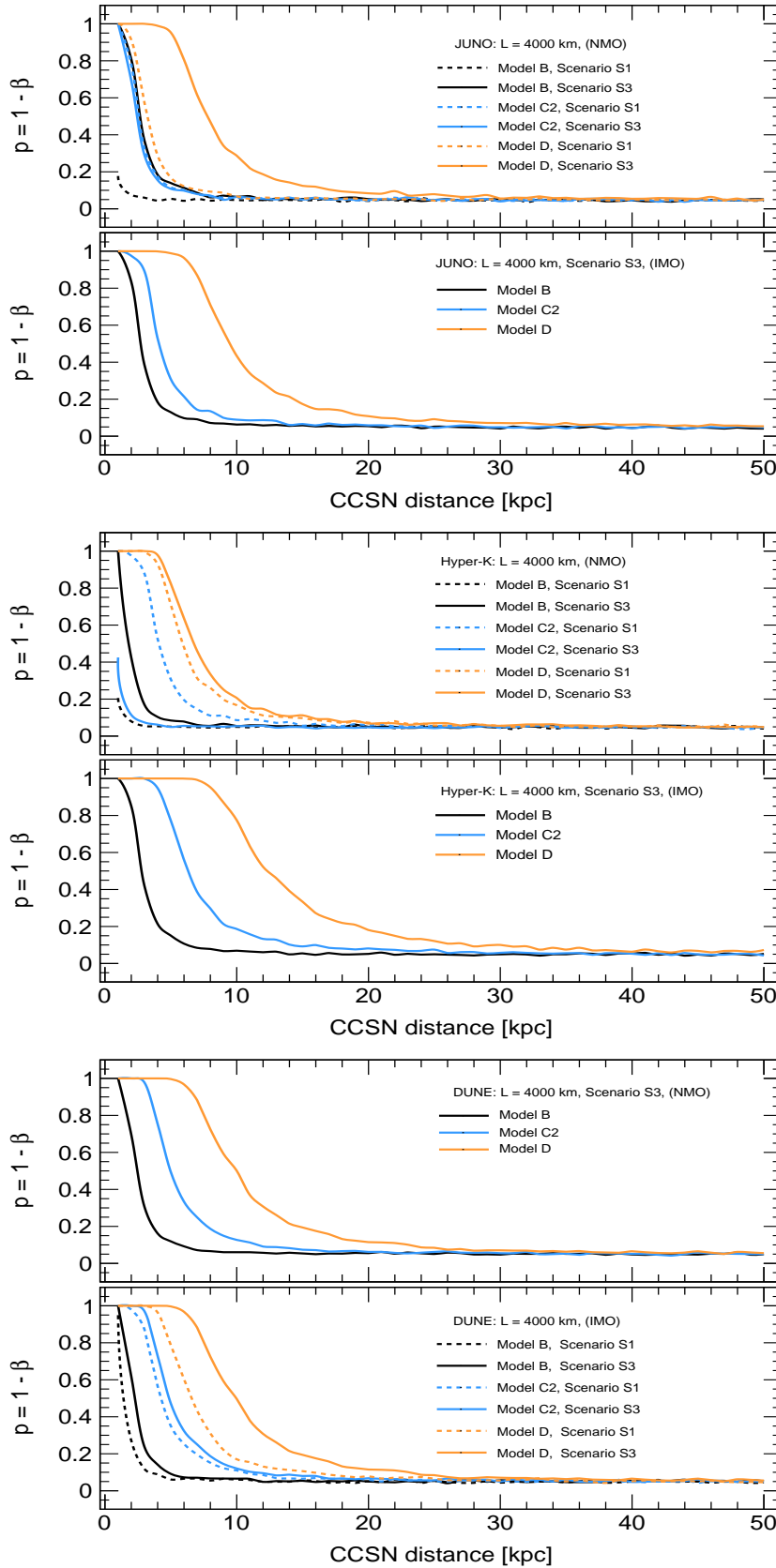


Figure 6.3: Detection probability of the Earth matter effects at 2σ (95.45% C.L.) by JUNO (upper panel), Hyper-K (middle panel) and DUNE (lower panel), for NMO (upper panel of each subfigure) and IMO (lower panel of each subfigure) for different CCSN emission models B, C2 and D as a function of the distance to CCSN.

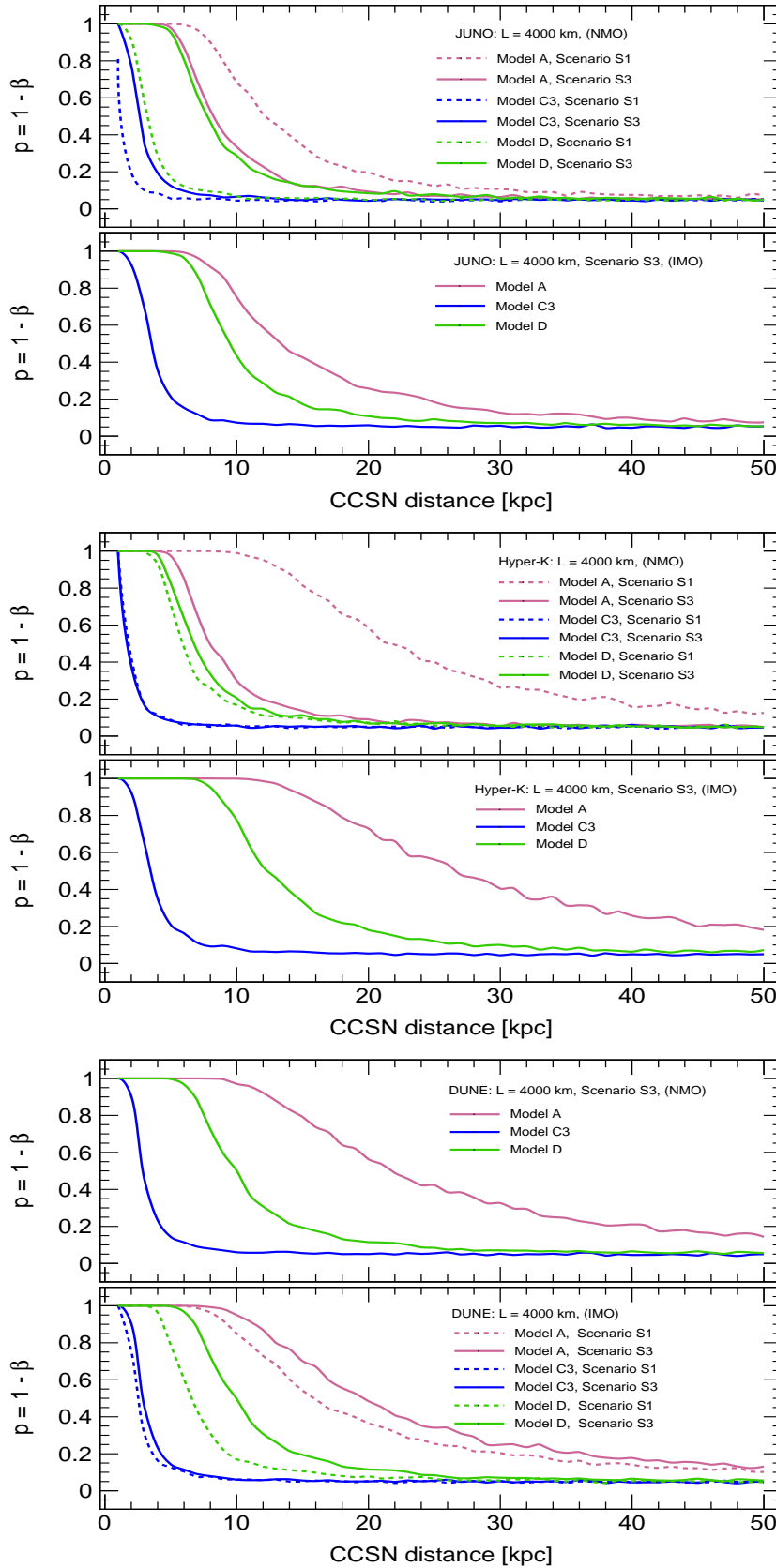


Figure 6.4: Detection probability of the Earth matter effects at 2σ (95.45% C.L.) by JUNO (upper panel), Hyper-K (middle panel) and DUNE (lower panel), for NMO (upper panel of each subfigure) and IMO (lower panel of each subfigure) for different CCSN emission models B, C3 and D as a function of the distance to CCSN.

2. JUNO and Hyper-K present a higher probability of detection of the effects under consideration if the neutrino mass ordering is inverted while DUNE has approximately equal possibilities in both orderings. It should be noted that in the absence of neutrino decay, we expect that it is not possible to observe such effects in the anti-neutrino detection channel for IMO, nor is it possible to observe them in the neutrino channel for NMO.
3. There is a greater possibility of clearly and unambiguously identifying the presence of the Earth matter effects in the neutrino energy spectrum for distances < 10 kpc. This is because the number of detected events increases with the proximity of the supernova to Earth. In particular, in the case of a CCSN at a distance of ~ 1 kpc the probability is close to unity.
4. A comparison between Figs. 6.3 and 6.4 shows that the probabilities using the models in set $\{A, C_3, D\}$ are greater than the probabilities using the models in set $\{B, C_2, D\}$. The success on identifying the Earth matter effects depends very much on the number of events detected, for this reason there will be a better chance of observing these effects if the entire emission interval of ~ 10 s is considered in the analysis, instead of considering the neutronization burst, the accretion and cooling phases separately.

Conclusions

The aim of this thesis was to study the sensitivity that the next generation of detectors (JUNO, Hyper-K and DUNE) will have to the detection of the Earth matter effects through the identification of the modulations in the energy spectrum of neutrinos from CCSNe in our galaxy, assuming the possibility of the invisible decay of ν_2 after the neutrinos have left the star, on their way to Earth because the decay effects can potentially increase the Earth matter effects. To achieve this purpose, three decay scenarios were created: S1 (corresponding the case where there is not neutrino decay), S2 ($\sim 50\%$ of decay) and S3 (100% of decay), as well as six neutrino emission models: A, B, C1, C2, C3 and D (tabla 2.2) with which, for each detector, the inverse energy spectrum was constructed and later the Fourier transform was used to obtain the peaks, in the power spectrum, that characterize the frequencies of these modulations due to the interaction of the CCSN neutrinos with the matter of the Earth. This study was carried out for three baselines $L = 4000$ km, $L = 8000$ km and $L = 12000$ km.

Due to the finite number of events obtained to carry out this analysis, it is necessary to take into account the statistical fluctuations in the determination of the number of events and therefore the uncertainty in the unambiguous determination of one of these peaks. As statistical tools to discriminate between signal (presence of Earth matter effects, and therefore identification of a peak in the power spectrum) and background fluctuations, we use the sensitivity d' and the probability of detection p defined in chapter 6 in the context of the signal detection theory which was used previously in Ref. [203] to determine the probability of observation of these effects (without neutrino decay). The main results of this research include the following:

- From a theoretical point of view, the incorporation of ν_2 decay into the study of the energy spectrum of CCSN neutrinos can alter the probability of observing the so-called Earth matter effects. However a clear identification of such effects by the next generation of detectors such as JUNO, Hyper-K and DUNE would only take place for decay

rates of ν_2 greater than $\sim 70\%$, as observed in Fig. 6.2 which shows d' as a function of r_2 . This is basically due to the presence of double-peak structures in the power spectrum which suppress the intensity of the peaks due to the partial destructive interference presented among the different components of the power spectrum, similar to what happen in the case without decay effect as discussed in Ref. [60].

- As already mentioned in previous works [57, 203], the capability of a detector to identify the Earth matter effects by detecting the modulations in the energy spectrum of the neutrinos that reach the detector depends mainly on the number of detected events and the energy resolution of the detector, therefore, according to the results observed in Figs. 6.3 and 6.4 we can conclude that there is a greater possibility of clearly and unambiguously identifying the presence of the Earth matter effects for CCSNe at distances < 10 kpc. In the case of neutrinos coming from core-collapse supernovae in our galaxy or from any of its satellite galaxies (e.g., the Large Magellanic Cloud), the number of observed events will be considerably reduced due to the much longer distances they have to travel to reach the Earth, typically $\sim \mathcal{O}(10)$ kpc.
- JUNO and Hyper-K present a higher probability of detection of the effects under consideration if the neutrino mass ordering is inverted while DUNE has approximately equal possibilities in both orderings.
- In the standard scenario (no neutrino decay) the observation of the effects due to the Earth matter are restricted only to the anti-neutrino channel if the mass ordering is normal and to the neutrino channel if the ordering is inverted. The addition of ν_2 decay to this work evidenced the possibility of observing Earth matter effects for both mass orderings in both detection channels, ν_e and $\bar{\nu}_e$. Therefore, if Earth matter effects are observed, in the next CCSN, in both channels (neutrino and anti-neutrino) at the same time, we can consider this evidence as an indication of the presence of neutrino decay.
- Another fact that could be considered as evidence of CCSN neutrino decay would be the Earth matter effects observation in the ν_e channel and the simultaneously disappearance of the neutronization peak from the CCSN neutrino burst.
- In the case of CCSN neutrinos, the trajectories that these follow inside the Earth to reach the detector can generally be classified into two: 1) paths that only cross the mantle. In this case, the shorter the path length, the greater the chance of observing Earth matter effects. For example,

small baselines such as $L = 4000$ km present a greater opportunity to identify the modulations compared to the case of longer baselines such as $L = 8000$ km. Indeed, the dependence on energy presented by the regeneration factors for baselines with $L \sim 4000$ km is slower compared to that exhibited by the regeneration factors with the longer baseline. In the first case, it will be easier to detect such modulations with the expected energy resolutions for the future detectors under consideration. 2) paths that cross both the mantle and the core of the Earth. In this case, contemplating the possibility of 100% of ν_2 decay, JUNO's energy resolution will allow it to observe the three peaks that occur in the power spectrum, which will increase the chance of observing the Earth matter effects.

- Finally we can conclude that in the case of a typical CCSN at our galaxy (10.7 ± 4.5 kpc [58]), the presence of 100% of ν_2 decay can enhance the probability of observation of the Earth matter effects, see for example the probability for model D in Figs. 6.3 and 6.4. However, this result is model dependent and given the small number of events detected from the supernova SN 1987A, we are currently at the mercy of the advances in numerical simulation which at the time indicate that during the cooling phase there is a tendency towards the equalization of the fluxes and the proximity of the average values of the energies under consideration, $\langle E_{\bar{\nu}_e} \rangle$ and $\langle E_{\nu_x} \rangle$.

Bibliography

- [1] AHMAD, Q. R. et al. (SNO Collaboration). Measurement of day and night neutrino energy spectra at SNO and constraints on neutrino mixing parameters. **Phys. Rev. Lett.**, v. 89, p. 011302, 2002.
- [2] AHMAD, Q. R. et al. (SNO Collaboration). Direct evidence for neutrino flavor transformation from neutral current interactions in the Sudbury Neutrino Observatory. **Phys. Rev. Lett.**, v. 89, p. 011301, 2002.
- [3] FUKUDA, Y. et al. (Super-Kamiokande Collaboration). Evidence for oscillation of atmospheric neutrinos. **Phys. Rev. Lett.**, v. 81, p. 1562–1567, 1998.
- [4] KAJITA, T.; KEARNS, E.; SHIOZAWA, M. Establishing atmospheric neutrino oscillations with Super-Kamiokande. **Nucl. Phys. B**, v. 908, p. 14–29, 2016.
- [5] EGUCHI, K. et al. (KamLAND Collaboration). First results from KamLAND: Evidence for reactor anti-neutrino disappearance. **Phys. Rev. Lett.**, v. 90, p. 021802, 2003.
- [6] ARAKI, T. et al. (KamLAND Collaboration). Measurement of neutrino oscillation with KamLAND: Evidence of spectral distortion. **Phys. Rev. Lett.**, v. 94, p. 081801, 2005.
- [7] AN, F. P. et al. (Daya Bay Collaboration). Observation of electron-antineutrino disappearance at Daya Bay. **Phys. Rev. Lett.**, v. 108, p. 171803, 2012.
- [8] ABE, Y. et al. (Double Chooz Collaboration). Indication of Reactor $\bar{\nu}_e$ Disappearance in the Double Chooz Experiment. **Phys. Rev. Lett.**, v. 108, p. 131801, 2012.
- [9] AHN, J. K. et al. (RENO Collaboration). Observation of Reactor Electron Antineutrino Disappearance in the RENO Experiment. **Phys. Rev. Lett.**, v. 108, p. 191802, 2012.

- [10] ABE, K. et al. (T2K Collaboration). First Muon-Neutrino Disappearance Study with an Off-Axis Beam. **Phys. Rev. D**, v. 85, p. 031103, 2012.
- [11] ADAMSON, P. et al. (MINOS Collaboration). Measurement of Neutrino and Antineutrino Oscillations Using Beam and Atmospheric Data in MINOS. **Phys. Rev. Lett.**, v. 110, n. 25, p. 251801, 2013.
- [12] ADAMSON, P. et al. (NOvA Collaboration). Measurement of the neutrino mixing angle θ_{23} in NOvA. **Phys. Rev. Lett.**, v. 118, n. 15, p. 151802, 2017.
- [13] ESTEBAN, I. et al. The fate of hints: updated global analysis of three-flavor neutrino oscillations. **JHEP**, v. 09, p. 178, 2020.
- [14] DE SALAS, P. F. et al. 2020 global reassessment of the neutrino oscillation picture. **JHEP**, v. 02, p. 071, 2021.
- [15] BANDYOPADHYAY, A.; CHOUBEY, S.; GOSWAMI, S. Exploring the sensitivity of current and future experiments to $\theta(\text{solar})$. **Phys. Rev.**, v. D67, p. 113011, 2003.
- [16] DE SALAS, P. F. et al. Neutrino Mass Ordering from Oscillations and Beyond: 2018 Status and Future Prospects. **Frontiers in Astronomy and Space Sciences**, v. 5, p. 36, 2018.
- [17] MYSLIK, J. (LEGEND Collaboration). LEGEND: The Large Enriched Germanium Experiment for Neutrinoless Double-Beta Decay. **In: 13th Conference on the Intersections of Particle and Nuclear Physics**, Oct 2018.
- [18] GUINN, I. S.; LÓPEZ-CASTAÑO, J. M. Current status of LEGEND: Searching for Neutrinoless Double-Beta Decay in ^{76}Ge : Part I. **PoS**, v. LeptonPhoton2019, p. 143, 2019.
- [19] LÓPEZ-CASTAÑO, J. M.; GUINN, I. Current status of LEGEND: Searching for Neutrinoless Double-Beta Decay in ^{76}Ge : Part II. **PoS**, v. LeptonPhoton2019, p. 162, 2019.
- [20] ARMENGAUD, E. et al. The CUPID-Mo experiment for neutrinoless double-beta decay: performance and prospects. **Eur. Phys. J. C**, v. 80, n. 1, p. 44, 2020.
- [21] ALBANESE, V. et al. (SNO+ Collaboration). **The SNO+ Experiment**. **Physics.ins-det**, 2104.11687, 2021.

- [22] ADHIKARI, G. et al. (nEXO Collaboration). **nEXO: Neutrinoless double beta decay search beyond 10^{28} year half-life sensitivity.** Nucl-ex, 2106.16243, 2021.
- [23] MARTÍN-ALBO, J. et al. (NEXT Collaboration). The NEXT experiment for neutrinoless double beta decay searches. **In: 31st Rencontres de Blois on Particle Physics and Cosmology**, Oct 2019.
- [24] AKER, M. et al. (KATRIN Collaboration). Improved Upper Limit on the Neutrino Mass from a Direct Kinematic Method by KATRIN. **Phys. Rev. Lett.**, v. 123, n. 22 , p. 221802, 2019.
- [25] GONZALEZ-GARCIA, M. C.; MALTONI, M. Status of Oscillation plus Decay of Atmospheric and Long-Baseline Neutrinos. **Phys. Lett.**, v. B663, p. 405–409, 2008.
- [26] ABRAHÃO, T. et al. Constraint on neutrino decay with medium-baseline reactor neutrino oscillation experiments. **Journal of High Energy Physics**, v. 2015, n. 11 , p. 1, Nov 2015.
- [27] CHOUBEY, S.; GOSWAMI, S.; PRAMANIK, D. A study of invisible neutrino decay at dune and its effects on θ_{23} measurement. **Journal of High Energy Physics**, v. 2018, n. 2 , p. 55, Feb 2018.
- [28] PORTO-SILVA, Y. P. et al. Constraining visible neutrino decay at KamLAND and JUNO. **Eur. Phys. J. C**, v. 80, n. 10 , p. 999, 2020.
- [29] BERRYMAN, J. M.; DE GOUVEA, A.; HERNANDEZ, D. Solar Neutrinos and the Decaying Neutrino Hypothesis. **Phys. Rev. D**, v. 92, n. 7 , p. 073003, 2015.
- [30] AHARMIM, B. et al. (NSO Collaboration). Constraints on Neutrino Lifetime from the Sudbury Neutrino Observatory. **Phys. Rev. D**, v. 99, n. 3 , p. 032013, 2019.
- [31] DE GOUVÊA, A. et al. Fundamental physics with the diffuse supernova background neutrinos. **Phys. Rev. D**, v. 102, p. 123012, 2020.
- [32] AGUILAR, A. et al. (LSND Collaboration). Evidence for neutrino oscillations from the observation of $\bar{\nu}_e$ appearance in a $\bar{\nu}_\mu$ beam. **Phys. Rev. D**, v. 64, p. 112007, Nov 2001.
- [33] AGUILAR-AREVALO, A. A. et al. (MiniBooNE Collaboration). Improved search for $\bar{\nu}_\mu \rightarrow \bar{\nu}_e$ oscillations in the minibooNE experiment. **Phys. Rev. Lett.**, v. 110, p. 161801, Apr 2013.

- [34] DENTLER, M. et al. Updated Global Analysis of Neutrino Oscillations in the Presence of eV-Scale Sterile Neutrinos. **JHEP**, v. 08, p. 010, 2018.
- [35] ABAZAJIAN, K. N. et al. **Light Sterile Neutrinos: A White Paper**. HEP, 1204.5379, 2012.
- [36] GIUNTI, C. Light Sterile Neutrinos: Status and Perspectives. **Nucl. Phys.**, v. B908, p. 336–353, 2016.
- [37] LOPES, I. The spectroscopy of solar sterile neutrinos. **The European Physical Journal C**, v. 78, n. 4 , p. 327, Apr 2018.
- [38] GIUNTI, C.; LASSERRE, T. eV-scale Sterile Neutrinos. **Ann. Rev. Nucl. Part. Sci.**, v. 69, p. 163–190, 2019.
- [39] DASGUPTA, B.; KOPP, J. Sterile Neutrinos. **Phys. Rept.**, v. 928, p. 63, 2021.
- [40] BERRYMAN, J. M.; HUBER, P. Sterile Neutrinos and the Global Reactor Antineutrino Dataset. **JHEP**, v. 01, p. 167, 2021.
- [41] AARTSEN, M. G. et al (IceCube Collaboration). Searches for sterile neutrinos with the icecube detector. **Phys. Rev. Lett.**, v. 117, p. 071801, Aug 2016.
- [42] LI, XUE-QIAN; LIU, Y.; WEI, ZHENG-TAO. Neutrino decay as a possible interpretation to the MiniBooNE observation with unparticle scenario. **Eur. Phys. J.**, v. C56, p. 97–103, 2008.
- [43] MOSS, Z. et al. Exploring a nonminimal sterile neutrino model involving decay at icecube. **Physical Review D**, v. 97, n. 055017 , p. 12, 2018.
- [44] MOHANTY, S.; SADHUKHAN, S. Explanation of icecube spectrum with $\nu \rightarrow 3\nu$ neutrino splitting in a ν 2hdm model. **Journal of High Energy Physics**, v. 2018, n. 10 , p. 111, Oct 2018.
- [45] HIRATA, K. et al. (Kamiokande-II Collaboration). Observation of a Neutrino Burst from the Supernova SN 1987a. **Phys. Rev. Lett.**, v. 58, p. 1490–1493, 1987.
- [46] BIONTA, R.M. et al. Observation of a Neutrino Burst in Coincidence with Supernova SN 1987a in the Large Magellanic Cloud. **Phys. Rev. Lett.**, v. 58, p. 1494, 1987.

- [47] ALEKSEEV, E. N. et al. Detection of the Neutrino Signal From SN1987A in the LMC Using the Inr Baksan Underground Scintillation Telescope. **Phys. Lett. B**, v. 205, p. 209–214, 1988.
- [48] FRIEMAN, J. A.; HABER, H. E.; FREESE, K. Neutrino Mixing, Decays and Supernova SN1987a. **Phys. Lett. B**, v. 200, p. 115–121, 1988.
- [49] CHUPP, E. L.; VESTRAND, W.T.; REPPIN, C. Experimental Limits on the Radiative Decay of SN1987A Neutrinos. **Phys. Rev. Lett.**, v. 62, p. 505–508, 1989.
- [50] BEACOM, J. F. BELL, N. F. Do Solar Neutrinos Decay? **Phys. Rev. D**, v. 65, p. 113009, 2002.
- [51] FOGLI, G.L. et al. Three generation flavor transitions and decays of supernova relic neutrinos. **Phys. Rev. D**, v. 70, p. 013001, 2004.
- [52] ANDO, S. Decaying neutrinos and implications from the supernova relic neutrino observation. **Phys. Lett. B**, v. 570, p. 11, 2003.
- [53] ANDO, S. Appearance of neutronization peak and decaying supernova neutrinos. **Phys. Rev. D**, v. 70, p. 033004, 2004.
- [54] DE GOUVÊA, A.; MARTINEZ-SOLER, I.; SEN, M. Impact of neutrino decays on the supernova neutronization-burst flux. **Phys. Rev. D**, v. 101, n. 4 , p. 043013, 2020.
- [55] DIGHE, A. S.; SMIRNOV, A. Y. Identifying the neutrino mass spectrum from the neutrino burst from a supernova. **Phys. Rev. D**, v. 62, p. 033007, 2000.
- [56] LUNARDINI, C.; SMIRNOV, A. Y. Supernova neutrinos: Earth matter effects and neutrino mass spectrum. **Nucl. Phys. B**, v. 616, p. 307–348, 2001.
- [57] DIGHE, A. S.; KEIL, MATHIAS T.; RAFFELT, G. G. Identifying earth matter effects on supernova neutrinos at a single detector. **JCAP**, v. 06, p. 006, 2003.
- [58] MIRIZZI, A.; RAFFELT, G. G.; SERPICO, P. D. Earth matter effects in supernova neutrinos: Optimal detector locations. **JCAP**, v. 05, p. 012, 2006.
- [59] SCHOLBERG, K. Supernova Signatures of Neutrino Mass Ordering. **J. Phys. G**, v. 45, n. 1 , p. 014002, 2018.

- [60] BORRIELLO, E. et al. Can one observe Earth matter effects with supernova neutrinos? *Phys. Rev. D*, v. 86, p. 083004, 2012.
- [61] LIAO, W. Detecting supernovae neutrino with Earth matter effect. *Phys. Rev. D*, v. 94, n. 11, p. 113016, 2016.
- [62] AN, F. et al. (JUNO Collaboration). Neutrino Physics with JUNO. *J. Phys. G*, v. 43, n. 3, p. 030401, 2016.
- [63] ABE, K. et al. (Hyper-Kamiokande Collaboration). **Hyper-Kamiokande Design Report**. physics.ins-det, 1805.04163, 2018.
- [64] ABI, B. et al. (DUNE Collaboration). **Deep Underground Neutrino Experiment (DUNE), Far Detector Technical Design Report, Volume II DUNE Physics**. HEP, 2002.03005, 2020.
- [65] CHADWICK, J. Intensitätsverteilung im magnetischen Spectrum der β -Strahlen von radium B + C. *Verhandl. Dtsc. Phys. Ges.*, v. 16, p. 383, 1914.
- [66] PAULI, W. Dear radioactive ladies and gentlemen. *Phys. Today*, v. 31N9, p. 27, 1978.
- [67] FERMI, E. An attempt of a theory of beta radiation. 1. *Z. Phys.*, v. 88, p. 161–177, 1934.
- [68] COWAN, C. L. et al. Detection of the free neutrino: A Confirmation. *Science*, v. 124, p. 103–104, 1956.
- [69] DANBY, G. et al. Observation of High-Energy Neutrino Reactions and the Existence of Two Kinds of Neutrinos. *Phys. Rev. Lett.*, v. 9, p. 36–44, 1962.
- [70] KODAMA, K. et al. (DONUT Collaboration). Observation of tau neutrino interactions. *Phys. Lett. B*, v. 504, p. 218–224, 2001.
- [71] DECAMP, D. et al. (ALEPH Collaboration). A Precise Determination of the Number of Families With Light Neutrinos and of the Z Boson Partial Widths. *Phys. Lett. B*, v. 235, p. 399–411, 1990.
- [72] WEINBERG, S. A Model of Leptons. *Phys. Rev. Lett.*, v. 19, p. 1264–1266, 1967.
- [73] GLASHOW, S. L. Partial Symmetries of Weak Interactions. *Nucl. Phys.*, v. 22, p. 579–588, 1961.

- [74] SALAM, A. Weak and Electromagnetic Interactions. **Conf. Proc. C**, v. 680519, p. 367–377, 1968.
- [75] GOLDHABER, M.; GRODZINS, L.; SUNYAR, A. W. Helicity of Neutrinos. **Phys. Rev.**, v. 109, p. 1015–1017, 1958.
- [76] CHANG, T. Parity violation and neutrino mass. **Nucl. Sci. Tech.**, v. 13, p. 129–133, 2002.
- [77] WU, C. S. et al. Experimental test of parity conservation in beta decay. **Phys. Rev.**, v. 105, p. 1413–1415, Feb 1957.
- [78] LESGOURGUES, J.; PASTOR, S. Massive neutrinos and cosmology. **Phys. Rept.**, v. 429, p. 307–379, 2006.
- [79] ALAM, S. et al. (eBOSS Collaboration). Completed SDSS-IV extended Baryon Oscillation Spectroscopic Survey: Cosmological implications from two decades of spectroscopic surveys at the Apache Point Observatory. **Phys. Rev. D**, v. 103, n. 8 , p. 083533, 2021.
- [80] ESCUDERO, M. et al. Relaxing Cosmological Neutrino Mass Bounds with Unstable Neutrinos. **JHEP**, v. 12, p. 119, 2020.
- [81] FORMAGGIO, J. A.; DE GOUVÊA, A.; ROBERTSON, R. G. Direct Measurements of Neutrino Mass. **Phys. Rept.**, v. 914, p. 1–54, 2021.
- [82] UMEHARA, S. et al. Neutrino-less double-beta decay of Ca-48 studied by Ca F(2)(Eu) scintillators. **Phys. Rev. C**, v. 78, p. 058501, 2008.
- [83] AGOSTINI, M. et al. (GERDA Collaboration). Final Results of GERDA on the Search for Neutrinoless Double- β Decay. **Phys. Rev. Lett.**, v. 125, n. 25 , p. 252502, 2020.
- [84] ALVIS, S. I. et al. (Majorana Collaboration). A Search for Neutrinoless Double-Beta Decay in ^{76}Ge with 26 kg-yr of Exposure from the MAJORANA DEMONSTRATOR. **Phys. Rev. C**, v. 100, n. 2 , p. 025501, 2019.
- [85] BARABASH, A. S. (NEMO Collaboration). Investigation of double-beta-decay processes at the NEMO-3 tracking detector. **Phys. Atom. Nucl.**, v. 68, p. 414–419, 2005.
- [86] ARGYRIADES, J. et al. (NEMO-3 Collaboration). Measurement of the two neutrino double beta decay half-life of Zr-96 with the NEMO-3 detector. **Nucl. Phys. A**, v. 847, p. 168–179, 2010.

- [87] ARNOLD, R. et al. (NEMO-3 Collaboration). Results of the search for neutrinoless double- β decay in ^{100}Mo with the nemo-3 experiment. **Phys. Rev. D**, v. 92, p. 072011, Oct 2015.
- [88] ARNOLD, R. et al. (NEMO-3 Collaboration). Measurement of the $2\nu\beta\beta$ decay half-life and search for the $0\nu\beta\beta$ decay of ^{116}Cd with the nemo-3 detector. **Phys. Rev. D**, v. 95, p. 012007, Jan 2017.
- [89] ADAMS, D. Q. et al. (CUORE Collaboration). Improved limit on neutrinoless double-beta decay in ^{130}Te with cuore. **Phys. Rev. Lett.**, v. 124, p. 122501, Mar 2020.
- [90] ADAMS, D. Q. et al. (CUORE Collaboration). **High sensitivity neutrinoless double-beta decay search with one tonne-year of CUORE data**. Nucl-ex, 2104.06906, 2021.
- [91] GANDO, A. et al. (KamLAND-Zen Collaboration). Search for majorana neutrinos near the inverted mass hierarchy region with kamland-zen. **Phys. Rev. Lett.**, v. 117, p. 082503, Aug 2016.
- [92] GANDO, Y. et al. (KamLAND-Zen Collaboration). **The nylon balloon for xenon loaded liquid scintillator in KamLAND-Zen 800 neutrinoless double-beta decay search experiment**. Physics.ins-det, 2104.10452, 2021.
- [93] ANTON, G. et al. (EXO-200 Collaboration). Search for Neutrinoless Double- β Decay with the Complete EXO-200 Dataset. **Phys. Rev. Lett.**, v. 123, n. 16, p. 161802, 2019.
- [94] ARNOLD, R. et al. (NEMO-3 Collaboration). Measurement of the $2\nu\beta\beta$ decay half-life of ^{150}Nd and a search for $0\nu\beta\beta$ decay processes with the full exposure from the nemo-3 detector. **Phys. Rev. D**, v. 94, p. 072003, Oct 2016.
- [95] AGOSTINI, M.; BENATO, G.; DETWILER, J. Discovery probability of next-generation neutrinoless double- β decay experiments. **Phys. Rev. D**, v. 96, n. 5, p. 053001, 2017.
- [96] VITAGLIANO, E.; TAMBORRA, I.; RAFFELT, G. Grand Unified Neutrino Spectrum at Earth: Sources and Spectral Components. **Rev. Mod. Phys.**, v. 92, p. 45006, 2020.
- [97] AUDREN, B. et al. Robustness of cosmic neutrino background detection in the cosmic microwave background. **JCAP**, v. 03, p. 036, 2015.

- [98] IRVINE, J. M.; HUMPHREYS, R. Neutrino masses and the cosmic-neutrino background. **Journal of Physics G: Nuclear Physics**, v. 9, n. 7, p. 847–852, Jul 1983.
- [99] BAHCALL, J. N.; ULRICH, R. K. Solar models, neutrino experiments, and helioseismology. **Rev. Mod. Phys.**, v. 60, p. 297–372, Apr 1988.
- [100] BETHE, H. A. Energy production in stars. **Phys. Rev.**, v. 55, p. 434–456, Mar 1939.
- [101] AGOSTINI, M. et al. (BOREXINO Collaboration). Experimental evidence of neutrinos produced in the CNO fusion cycle in the Sun. **Nature**, v. 587, p. 577–582, 2020.
- [102] LUDHOVA, L.; ZAVATARELLI, S. Studying the Earth with Geoneutrinos. **Adv. High Energy Phys.**, v. 2013, p. 425693, 2013.
- [103] POLLACK, H.; HURTER, S.; JOHNSON, J. Heat flow from the Earth's interior: Analysis of the global data set. **Reviews of Geophysics**, v. 31, p. 14, 1993.
- [104] STEIN, C. Heat flow of the earth. **Global Earth Physics. In: A handbook of physical constants**, Jan 1995.
- [105] Kamland Collaboration. Partial radiogenic heat model for Earth revealed by geoneutrino measurements. **Nature Geoscience**, v. 4, n. 9, p. 647–651, Sept. 2011.
- [106] HIRATA, K. S. et al. Observation in the Kamiokande-II Detector of the Neutrino Burst from Supernova SN 1987a. **Phys. Rev. D**, v. 38, p. 448–458, 1988.
- [107] HAINES, T. et al. (IMB Collaboration). Neutrinos From SN1987A in the Imb Detector. **Nucl. Instrum. Meth. A**, v. 264, p. 28–31, 1988.
- [108] ALEXEYEV E. N. et al. Detection of the neutrino signal from sn 1987a in the lmc using the inr baksan underground scintillation telescope. **Physics Letters B**, v. 205, n. 2, p. 209–214, 1988.
- [109] AGLIETTA, M. et al. The neutrino burst from SN 1987A detected in the Mont Blanc LSD experiment. In: Kafatos, M. Michalitsianos, A. G., editors, **SUPERNOVA 1987A IN THE LARGE MAGELLANIC CLOUD**, p. 119–129, Jan. 1988.

- [110] GAISSER, T. K.; HONDA, M. Flux of atmospheric neutrinos. **Ann. Rev. Nucl. Part. Sci.**, v. 52, p. 153–199, 2002.
- [111] SECKEL, D.; STANEV, T.; GAISSER, T. K. Signatures of Cosmic-Ray Interactions on the Solar Surface. **apj**, v. 382, p. 652, Dec 1991.
- [112] INGELMAN, G.; THUNMAN, M. High-energy neutrino production by cosmic ray interactions in the sun. **Phys. Rev. D**, v. 54, p. 4385–4392, 1996.
- [113] WAXMAN, E.; BAHCALL, J. High energy neutrinos from astrophysical sources: An upper bound. **Phys. Rev. D**, v. 59, p. 023002, Dec 1998.
- [114] MANNHEIM, K. High-energy neutrinos from extragalactic jets. **Astroparticle Physics**, v. 3, n. 3 , p. 295–302, 1995.
- [115] WAXMAN, E.; BAHCALL, J. High energy neutrinos from cosmological gamma-ray burst fireballs. **Phys. Rev. Lett.**, v. 78, p. 2292–2295, Mar 1997.
- [116] STECKER, F. W. et al. High-energy neutrinos from active galactic nuclei. **Phys. Rev. Lett.**, v. 66, p. 2697–2700, May 1991.
- [117] AARTSEN, M. G. et al. (IceCube Collaboration). First observation of PeV-energy neutrinos with IceCube. **Phys. Rev. Lett.**, v. 111, p. 021103, 2013.
- [118] KOPP, S. E. Accelerator-based neutrino beams. **Phys. Rept.**, v. 439, p. 101–159, 2007.
- [119] ELDRED, J. et al. Beam intensity effects in Fermilab Booster synchrotron. **Phys. Rev. Accel. Beams**, v. 24, n. 4 , p. 044001, 2021.
- [120] PAPADIMITRIOU, V. et al. Design of the LBNF Beamline. **In: 7th International Particle Accelerator Conference**, Jul 2016.
- [121] KOSEKI, T. et al. Beam commissioning and operation of the J-PARC main ring synchrotron. **Progress of Theoretical and Experimental Physics**, v. 2012, n. 1 , Dec 2012. 02B004.
- [122] BRUNING, O. S. et al. LHC Design Report Vol.1: The LHC Main Ring. **CERN Yellow Reports: Monographs**, Jul 2004.
- [123] BENEDIKT, M. et al. LHC Design Report. 3. The LHC injector chain. **CERN Yellow Reports: Monographs**, Dec 2004.

- [124] APOLLINARI, G. et al. High-Luminosity Large Hadron Collider (HL-LHC): Technical Design Report V. 0.1. **CERN Yellow Reports: Monographs**, v. 4/2017, 2017.
- [125] DE KERRET, H. et al. (Double Chooz Collaboration). Double Chooz θ_{13} measurement via total neutron capture detection. **Nature Phys.**, v. 16, n. 5, p. 558–564, 2020.
- [126] AN, F. P. et al. Observation of electron-antineutrino disappearance at Daya Bay. **Phys. Rev. Lett.**, v. 108, p. 171803, Apr 2012.
- [127] AN, F. P. et al. (Daya Bay Collaboration). New measurement of θ_{13} via neutron capture on hydrogen at Daya Bay. **Phys. Rev. D**, v. 93, n. 7, p. 072011, 2016.
- [128] AHN, J. K. et al. (RENO Collaboration). Observation of reactor electron antineutrinos disappearance in the reno experiment. **Phys. Rev. Lett.**, v. 108, p. 191802, May 2012.
- [129] KIM, SOO-BONG (RENO Collaboration). Measurement of neutrino mixing angle Θ_{13} and mass difference Δm_{ee}^2 from reactor antineutrino disappearance in the RENO experiment. **Nucl. Phys. B**, v. 908, p. 94–115, 2016.
- [130] BAADE, W.; ZWICKY, F. On super-novae. **Proceedings of the National Academy of Sciences**, v. 20, n. 5, p. 254–259, 1934.
- [131] DA SILVA, L. A. L. The classification of supernovae. **Astrophys Space Sci.**, v. 202, n. 2, p. 215–236, 1993.
- [132] KUCHNER, M. J. et al. Evidence for ^{56}Ni ^{56}Co ^{56}Fe Decay in Type IA Supernovae. **Astrophysical Journal**, v. 426, p. L89, May 1994.
- [133] HORIUCHI, S.; KNELLER, J. P. What can be learned from a future supernova neutrino detection? **Journal of Physics G: Nuclear and Particle Physics**, v. 45, n. 043002, p. 74, 2018.
- [134] BURROWS, A. Colloquium: Perspectives on core-collapse supernova theory. **Rev. Mod. Phys.**, v. 85, p. 245, 2013.
- [135] JANKA, H. T. **Neutrino Emission from Supernovae**. Astro-ph.HE, 1702.08713, 2017.
- [136] JANKA, H. T. **Neutrino-driven Explosions**. Astro-ph.HE, 1702.08825, 2017.

- [137] JANKA, H. T. et al. Core-collapse supernovae: Reflections and directions. **Progress of Theoretical and Experimental Physics**, v. 2012, n. 1 , p. 01A309, Dec. 2012.
- [138] MÜLLER, B. Neutrino Emission as Diagnostics of Core-Collapse Supernovae. **Ann. Rev. Nucl. Part. Sci.**, v. 69, p. 253–278, 2019.
- [139] NAGAKURA, H. et al. Core-collapse supernova neutrino emission and detection informed by state-of-the-art three-dimensional numerical models. **Mon. Not. Roy. Astron. Soc.**, v. 500, n. 1 , p. 696–717, 2020.
- [140] JANKA, H. T. et al. Core-collapse supernovae: Reflections and directions. **Prog. Theor. Exp. Phys.**, v. 2012, n. 01A309 , p. 33, 2012.
- [141] QIAN, YONG-ZHONG. Neutrinos, supernovae, and the origin of the heavy elements. **Sci. China-Phys. Mech. Astron.**, v. 61, n. 049501 , p. 6, 2018.
- [142] HOROWITZ, C. J. Neutrino trapping in a supernova and the screening of weak neutral currents. **Phys. Rev. D**, v. 55, n. 4577 , p. 5, 1997.
- [143] BURROWS, A.; LATTIMER, J. M. The birth of neutron stars. **The Astrophysical Journal**, v. 307, n. 1 , p. 178–196, 1986.
- [144] WALLACE, J.; BURROWS, A.; DOLENCE, J. C. Detecting the supernova breakout burst in terrestrial neutrino detectors. **The Astrophysical Journal**, v. 817, n. 2 , p. 29, 2016.
- [145] O'CONNOR, E. P.; COUCH, S. M. Exploring fundamentally three-dimensional phenomena in high-fidelity simulations of core-collapse supernovae. **The Astrophysical Journal**, v. 865, n. 2 , p. 81, 2018.
- [146] JANKA, H. T. Conditions for shock revival by neutrino heating in core-collapse supernovae. **Astronomy and Astrophysics**, v. 368, n. 2 , p. 527–560, 2001.
- [147] FRIEMAN, J. A.; HABER, H. E.; FREESE, K. Neutrino mixing, decays and supernova 1987a. **Physics Letters B**, v. 200, n. 1,2 , p. 115–121, 1988.
- [148] TOTANI, T. et al. Future detection of supernova neutrino burst and explosion mechanism. **Astrophys. J.**, v. 496, p. 216–225, 1998.
- [149] KEIL, M. T.; RAFFELT, G. G.; JANKA, H. T. Monte Carlo study of supernova neutrino spectra formation. **Astrophys. J.**, v. 590, p. 971–991, 2003.

- [150] TAMBORRA, I. et al. High-resolution supernova neutrino spectra represented by a simple fit. **Phys. Rev. D**, v. 86, p. 125031, 2012.
- [151] TANG, J.; WANG, T.; WU, M. Constraining sterile neutrinos by core-collapse supernovae with multiple detectors. **JCAP**, v. 10, p. 038, 2020.
- [152] RAFFELT, G. G. et al. Supernova neutrinos: Flavor-dependent fluxes and spectra. **In: 4th Workshop on Neutrino Oscillations and their Origin (NOON2003)**, Mar 2003.
- [153] SERPICO, P. D. et al. Probing the neutrino mass hierarchy with the rise time of a supernova burst. **Phys. Rev. D**, v. 85, p. 085031, 2012.
- [154] FISCHER, T. et al. Protoneutron star evolution and the neutrino-driven wind in general relativistic neutrino radiation hydrodynamics simulations. **aap**, v. 517, p. A80, July 2010.
- [155] ANDO, S.; SATO, K. Relic neutrino background from cosmological supernovae. **New J. Phys.**, v. 6, p. 170, 2004.
- [156] GIUNTI, C.; CHUNG, W. K. **Fundamentals of Neutrino Physics and Astrophysics**. Oxford University Press, New York, 1st edition, 2007.
- [157] CLEVELAND, B. T. et al. Measurement of the solar electron neutrino flux with the Homestake chlorine detector. **Astrophys. J.**, v. 496, p. 505–526, 1998.
- [158] GAVRIN, V. N. The russian-american gallium experiment SAGE. **Physics-Uspekhi**, v. 54, n. 9 , p. 941–949, Sep 2011.
- [159] VIGNAUD, D. The Solar neutrino problem after the GALLEX artificial neutrino source experiment. **In: 30th Rencontres de Moriond: Euroconferences: Dark Matter in Cosmology, Clocks and Tests of Fundamental Laws**, 1995.
- [160] HAINES, T. J. et al. Calculation of atmospheric neutrino-induced backgrounds in a nucleon-decay search. **Phys. Rev. Lett.**, v. 57, p. 1986–1989, Oct 1986.
- [161] BAHCALL, J. N. et al. Are standard solar models reliable? **Phys. Rev. Lett.**, v. 78, p. 171–174, 1997.
- [162] BAHCALL, J. N.; SERENELLI, A. M.; BASU, S. 10,000 standard solar models: a Monte Carlo simulation. **Astrophys. J. Suppl.**, v. 165, p. 400–431, 2006.

- [163] BAHCALL, J. N.; BETHE, H. A. Do solar neutrino experiments imply new physics? *Phys. Rev. D*, v. 47, p. 1298–1301, 1993.
- [164] AKHMEDOV, E. K.; SMIRNOV, A. Y. Paradoxes of neutrino oscillations. *Phys. Atom. Nucl.*, v. 72, p. 1363–1381, 2009.
- [165] WOLFENSTEIN, L. Neutrino Oscillations in Matter. *Phys. Rev. D*, v. 17, p. 2369–2374, 1978.
- [166] MIKHEYEV, S. P.; SMIRNOV, A. Y. Resonance Amplification of Oscillations in Matter and Spectroscopy of Solar Neutrinos. *Sov. J. Nucl. Phys.*, v. 42, p. 913–917, 1985.
- [167] DOOLING, D. et al. Matter effects in four neutrino mixing. *Phys. Rev. D*, v. 61, p. 073011, 2000.
- [168] MALTONI, M.; SMIRNOV, A. Y. Solar neutrinos and neutrino physics. *Eur. Phys. J. A*, v. 52, n. 4, p. 87, 2016.
- [169] ADEY, D. et al. (Daya Bay Collaboration). Measurement of the Electron Antineutrino Oscillation with 1958 Days of Operation at Daya Bay. *Phys. Rev. Lett.*, v. 121, n. 24, p. 241805, 2018.
- [170] BAK, G. et al. (RENO Collaboration). Measurement of Reactor Antineutrino Oscillation Amplitude and Frequency at RENO. *Phys. Rev. Lett.*, v. 121, n. 20, p. 201801, 2018.
- [171] PANTALEONE, J. T. Neutrino oscillations at high densities. *Phys. Lett. B*, v. 287, p. 128–132, 1992.
- [172] DUAN, H. et al. Coherent Development of Neutrino Flavor in the Supernova Environment. *Phys. Rev. Lett.*, v. 97, p. 241101, 2006.
- [173] DUAN, H. et al. Simulation of Coherent Non-Linear Neutrino Flavor Transformation in the Supernova Environment. 1. Correlated Neutrino Trajectories. *Phys. Rev. D*, v. 74, p. 105014, 2006.
- [174] HANNESTAD, S. et al. Self-induced conversion in dense neutrino gases: Pendulum in flavour space. *Phys. Rev. D*, v. 74, p. 105010, 2006. [Erratum: *Phys.Rev.D* 76, 029901 (2007)].
- [175] FOGLI, G. L. et al. Collective neutrino flavor transitions in supernovae and the role of trajectory averaging. *JCAP*, v. 12, p. 010, 2007.
- [176] DUAN, H.; FULLER, G. M.; QIAN, YONG-ZHONG. Collective Neutrino Oscillations. *Ann. Rev. Nucl. Part. Sci.*, v. 60, p. 569–594, 2010.

- [177] DZIEWONSKI, A. M.; ANDERSON, D. L. Preliminary reference Earth model. *Phys. Earth. Plan. Int.*, v. 25, p. 297, 1981.
- [178] IOANNISIAN, A. N.; SMIRNOV, A. Y. Neutrino oscillations in low density medium. *Phys. Rev. Lett.*, v. 93, p. 241801, 2004.
- [179] IOANNISIAN, A. N. et al. A Precise analytical description of the earth matter effect on oscillations of low energy neutrinos. *Phys. Rev. D*, v. 71, p. 033006, 2005.
- [180] GELMINI, G. B.; RONCADELLI, M. Left-Handed Neutrino Mass Scale and Spontaneously Broken Lepton Number. *Phys. Lett. B*, v. 99, p. 411–415, 1981.
- [181] GELMINI, G. B.; VALLE, J. W. F. Fast Invisible Neutrino Decays. *Phys. Lett.*, v. B142, p. 181, 1984.
- [182] BAHCALL, J. N.; CABIBBO, N.; YAHIL, A. Are neutrinos stable particles? *Phys. Rev. Lett.*, v. 28, p. 316–318, Jan 1972.
- [183] ACKER, A.; PAKVASA, S.; PANTALEONE, J. Decaying dirac neutrinos. *Phys. Rev. D*, v. 45, p. R1–R4, Jan 1992.
- [184] ABDULLAHI, A.; DENTON, P. B. Visible Decay of Astrophysical Neutrinos at IceCube. *Phys. Rev. D*, v. 102, n. 2, p. 023018, 2020.
- [185] SÁNCHEZ, B. L. Decaimentos de neutrinos induzidos por escalares e aplicações a supernovas. Dissertação de mestrado, Instituto de Física Gleb Wataghin, Universidade Estadual de Campinas, Campinas, 2006.
- [186] LINDNER, M.; OHLSSON, T.; WINTER, W. Decays of supernova neutrinos. *Nucl. Phys. B*, v. 622, p. 429–456, 2002.
- [187] MIRIZZI, A.; MONTANINO, D.; SERPICO, P. D. Revisiting cosmological bounds on radiative neutrino lifetime. *Phys. Rev. D*, v. 76, p. 053007, 2007.
- [188] KIM, C. W.; LAM, W. P. Some remarks on neutrino decay via a Nambu-Goldstone boson. *Mod. Phys. Lett. A*, v. 5, p. 297–299, 1990.
- [189] CHIKASHIGE, Y.; MOHAPATRA, R. N.; PECCEI, R. D. Spontaneously Broken Lepton Number and Cosmological Constraints on the Neutrino Mass Spectrum. *Phys. Rev. Lett.*, v. 45, p. 1926, 1980.

- [190] CHIKASHIGE, Y.; MOHAPATRA, R. N.; PECCEI, R. D. Are There Real Goldstone Bosons Associated with Broken Lepton Number? *Phys. Lett.*, v. B98, p. 265–268, 1981.
- [191] SCHECHTER, J.; VALLE, J. W. F. Neutrino Decay and Spontaneous Violation of Lepton Number. *Phys. Rev.*, v. D25, p. 774, 1982.
- [192] BEREZHIANI, Z. G.; VYSOTSKY, M. I. Neutrino Decay in Matter. *Phys. Lett.*, v. B199, p. 281, 1987.
- [193] ACKER, A.; PAKVASA, S.; PANTALEONE, J. T. Decaying Dirac neutrinos. *Phys. Rev. D*, v. 45, p. 1–4, 1992.
- [194] GRIFFITHS, D. J. **Introduction to elementary particles; 2nd rev. version.** Physics textbook. Wiley, New York, NY, 2008.
- [195] WEINBERG, S. **The Quantum Theory of Fields**, volumen 1. Cambridge University Press, New York, NY, 1995.
- [196] KERSTEN, J.; SMIRNOV, A. Y. Decoherence and oscillations of supernova neutrinos. *Eur. Phys. J. C*, v. 76, n. 6 , p. 339, 2016.
- [197] DELGADO, E. A.; NUNOKAWA, H.; QUIROGA, A. A. **Probing neutrino decay scenarios by using the Earth matter effects on supernova neutrinos.** arXiv: 2109.02737 2021.
- [198] DJURCIC, Z. et al. (JUNO Collaboration). **JUNO Conceptual Design Report.** Physics.ins-det, 1508.07166, 2015.
- [199] LU, JIA-SHU; LI, YU-FENG; ZHOU, SHUN. Getting the most from the detection of Galactic supernova neutrinos in future large liquid-scintillator detectors. *Phys. Rev. D*, v. 94, n. 2 , p. 023006, 2016.
- [200] LU, JIA-SHU et al. Constraining Absolute Neutrino Masses via Detection of Galactic Supernova Neutrinos at JUNO. *JCAP*, v. 05, p. 044, 2015.
- [201] STEIGER, H. T. J. (JUNO Collaboration). Design and Status of JUNO. *J. Phys. Conf. Ser.*, v. 1468, n. 1 , p. 012187, 2020.
- [202] STRUMIA, A.; VISSANI, F. Precise quasielastic neutrino/nucleon cross-section. *Phys. Lett. B*, v. 564, p. 42–54, 2003.
- [203] DIGHE, A. S. et al. Signatures of supernova neutrino oscillations in the earth mantle and core. *JCAP*, v. 01, p. 004, 2004.

- [204] KAY, S. M. **Fundamentals of Statistical Signal Processing: Detection theory**, volumen 2 de **Fundamentals of Statistical Signal Processing**. Prentice-Hall PTR, New Jersey, 1998.
- [205] SCHOLBERG, K.; BURGMEIER, A.; WENDELL, R. Obtaining supernova directional information using the neutrino matter oscillation pattern. **Phys. Rev. D**, v. 81, p. 043007, 2010.
- [206] ABE, K. et al. (Hyper-Kamiokande Collaboration). Supernova Model Discrimination with Hyper-Kamiokande. **Astrophys. J.**, v. 916, n. 1 , p. 15, 2021.
- [207] ZSOLDOS, S. Large Area Photo-Detection System using 3-inch PMTs for the Hyper-Kamiokande Outer Detector. **JPS Conf. Proc.**, v. 27, p. 011018, 2019.
- [208] ABE, K. et al. (Hyper-Kamiokande Collaboration). Physics potentials with the second Hyper-Kamiokande detector in Korea. **PTEP**, v. 2018, n. 6 , p. 063C01, 2018.
- [209] SUZUKI, Y. The Super-Kamiokande experiment. **Eur. Phys. J. C**, v. 79, n. 4 , p. 298, 2019.
- [210] ABI, B. et al. (DUNE Collaboration). Deep Underground Neutrino Experiment (DUNE), Far Detector Technical Design Report, Volume I Introduction to DUNE. **JINST**, v. 15, n. 08 , p. T08008, 2020.
- [211] ABED ABUD, A. et al. (DUNE Collaboration). **Deep Underground Neutrino Experiment (DUNE) Near Detector Conceptual Design Report**. Physics.ins-det, 2103.13910, 2021.
- [212] ABI, B. et al. (DUNE Collaboration). Supernova neutrino burst detection with the Deep Underground Neutrino Experiment. **Eur. Phys. J. C**, v. 81, n. 5 , p. 423, 2021.
- [213] GIL BOTELLA, I.; RUBBIA, A. Oscillation effects on supernova neutrino rates and spectra and detection of the shock breakout in a liquid argon TPC. **JCAP**, v. 10, p. 009, 2003.
- [214] SEADROW, S. et al. Neutrino Signals of Core-Collapse Supernovae in Underground Detectors. **Mon. Not. Roy. Astron. Soc.**, v. 480, n. 4 , p. 4710–4731, 2018.

- [215] ABI, B. et al. (DUNE Collaboration). **Supernova Neutrino Burst Detection with the Deep Underground Neutrino Experiment**. HEP, 2008.06647, 2020.
- [216] SCHOLBERG, K. Supernova Neutrino Detection. **Ann. Rev. Nucl. Part. Sci.**, v. 62, p. 81–103, 2012.
- [217] ALBERT, J. et al. SNOwGLOBES (SuperNova Observatories with GLOBES) . https://github.com/SNOwGLOBES/snowglobes/blob/master/doc/snowglobes_1.2.pdf [accessed2019-07-13], 2018.
- [218] BLENNOW, M. et al. Quantifying the sensitivity of oscillation experiments to the neutrino mass ordering. **JHEP**, v. 03, p. 028, 2014.
- [219] CIUFFOLI, E.; EVSLIN, J.; ZHANG, X. Confidence in a neutrino mass hierarchy determination. **JHEP**, v. 01, p. 095, 2014.

A

CCSN neutrino spectra in presence of neutrino decay

As discussed in Section 4, the expected CCSN neutrino spectra in the presence of neutrino decay can be explicitly written in terms of the decay parameter, the time-integrated primary spectra and the mixing parameters. Here, we explicitly show all the calculations necessary to reach Eqs. (4-28a), (4-28b), (4-29a) and (4-29b).

We start with the calculation of F_{ν_e} and $F_{\bar{\nu}_e}$ for the case of normal mass ordering. For this purpose we rewrite the total fluxes of the neutrino mass eigenstates at the surface of the star in the following compact form:

$$F_{\nu_i} = a_i F_{\nu_e}^0 + (1 - a_i) F_{\nu_x}^0, \quad (\text{A-1a})$$

$$F_{\bar{\nu}_i} = \bar{a}_i F_{\bar{\nu}_e}^0 + (1 - \bar{a}_i) F_{\bar{\nu}_x}^0, \quad (\text{A-1b})$$

with $a_1 = a_2 = 0$ and $a_3 = 1$ for the calculation of F_{ν_e} and $\bar{a}_1 = 1$ and $\bar{a}_2 = 0$ for the calculation of $F_{\bar{\nu}_e}$. These values for a_i and \bar{a}_i are obtained from the analysis of the crossing probabilities P_H and P_L in Fig. 3.2.

With this information we can find F_{ν_e} by slightly modifying Eq. (3-52) to include the effect of the decay of the mass eigenstates, this is:

$$\begin{aligned} F_{\nu_e} &= \sum_{i=1}^3 |U_{ei}|^2 (1 - r_i) F_{\nu_i}, \\ &= |U_{e1}|^2 (1 - r_1) F_{\nu_1} + |U_{e2}|^2 (1 - r_2) F_{\nu_2} + |U_{e3}|^2 (1 - r_3) F_{\nu_3}, \\ &= c_{12}^2 c_{13}^2 (1 - r_1) F_{\nu_x}^0 + s_{12}^2 c_{13}^2 (1 - r_2) F_{\nu_x}^0 + s_{13}^2 (1 - r_3) F_{\nu_e}^0, \\ &= s_{13}^2 (1 - r_3) F_{\nu_e}^0 + (c_{12}^2 c_{13}^2 - r_1 c_{12}^2 c_{13}^2 + s_{12}^2 c_{13}^2 - r_2 s_{12}^2 c_{13}^2) F_{\nu_x}^0, \\ &= s_{13}^2 (1 - r_3) F_{\nu_e}^0 + (c_{13}^2 - r_1 c_{12}^2 c_{13}^2 - r_2 s_{12}^2 c_{13}^2) F_{\nu_x}^0, \end{aligned} \quad (\text{A-2})$$

which under the approximation $\theta_{13} = 0$ results in

$$F_{\nu_e} \approx (1 - r_1 c_{12}^2 - r_2 s_{12}^2) F_{\nu_x}^0. \quad (\text{A-3})$$

For the case of $F_{\bar{\nu}_e}$ we have a similar analysis:

$$\begin{aligned}
F_{\bar{\nu}_e} &= \sum_{i=1}^3 |U_{ei}|^2 (1 - r_i) F_{\bar{\nu}_i}, \\
&\approx |U_{e1}|^2 (1 - r_1) F_{\bar{\nu}_1} + |U_{e2}|^2 (1 - r_2) F_{\bar{\nu}_2}, \\
&\approx c_{12}^2 c_{13}^2 (1 - r_1) F_{\bar{\nu}_e}^0 + s_{12}^2 c_{13}^2 (1 - r_2) F_{\bar{\nu}_x}^0, \\
&\approx c_{12}^2 (1 - r_1) F_{\bar{\nu}_e}^0 + s_{12}^2 (1 - r_2) F_{\bar{\nu}_x}^0,
\end{aligned} \tag{A-4}$$

where we have ignore the term $|U_{e3}|^2 (1 - r_3) F_{\bar{\nu}_3}$ because the small mixing angle θ_{e3} is further suppressed in the stellar medium, so the $\bar{\nu}_e \rightarrow \bar{\nu}_3$ transitions are negligible.

Now we present the calculation of F_{ν_e} and $F_{\bar{\nu}_e}$ for the case of inverted mass ordering. Here $a_1 = 0$ and $a_2 = a_3 = 1$ for the calculation of F_{ν_e} and $\bar{a}_1 = \bar{a}_2 = 0$ for the calculation of $F_{\bar{\nu}_e}$. Therefore,

$$\begin{aligned}
F_{\nu_e} &= \sum_{i=1}^3 |U_{ei}|^2 (1 - r_i) F_{\nu_i}, \\
&\approx |U_{e1}|^2 (1 - r_1) F_{\nu_1} + |U_{e2}|^2 (1 - r_2) F_{\nu_2}, \\
&\approx c_{12}^2 c_{13}^2 (1 - r_1) F_{\nu_x}^0 + s_{12}^2 c_{13}^2 (1 - r_2) F_{\nu_e}^0, \\
&\approx s_{12}^2 (1 - r_2) F_{\nu_e}^0 + c_{12}^2 (1 - r_1) F_{\nu_x}^0,
\end{aligned} \tag{A-5}$$

and

$$\begin{aligned}
F_{\bar{\nu}_e} &= \sum_{i=1}^3 |U_{ei}|^2 (1 - r_i) F_{\bar{\nu}_i}, \\
&\approx |U_{e1}|^2 (1 - r_1) F_{\bar{\nu}_1} + |U_{e2}|^2 (1 - r_2) F_{\bar{\nu}_2}, \\
&\approx c_{12}^2 c_{13}^2 (1 - r_1) F_{\bar{\nu}_x}^0 + s_{12}^2 c_{13}^2 (1 - r_2) F_{\bar{\nu}_e}^0, \\
&\approx [c_{12}^2 (1 - r_1) + s_{12}^2 (1 - r_2)] F_{\bar{\nu}_x}^0, \\
&\approx [1 - r_1 c_{12}^2 - r_2 s_{12}^2] F_{\bar{\nu}_x}^0.
\end{aligned} \tag{A-6}$$